Improving Low-Degree Gravity Estimates through New Laser Ranging Satellites, Ground Stations, and Combination Solutions

by

Evan S. Tucker

B.A., University of Colorado Boulder, 2019

M.S., University of Colorado Boulder, 2021

A thesis submitted to the

Faculty of the Graduate School of the

University of Colorado in partial fulfillment

of the requirements for the degree of

Doctor of Philosophy

Department of Aerospace Engineering Sciences

2023

Committee Members:

Prof. R. Steven Nerem, Chair

Dr. Bryant D. Loomis

Prof. Marcus J. Holzinger

Prof. Jay W. McMahon

Dr. Felix W. Landerer

Tucker, Evan S. (Ph.D., Aerospace Engineering Sciences)

Improving Low-Degree Gravity Estimates through New Laser Ranging Satellites, Ground Stations, and Combination Solutions

Thesis directed by Prof. R. Steven Nerem

Earth's mass is constantly redistributing due to climatic and geophysical dynamics. Although changes in the deep solid Earth tend to occur over geologic timescales, near-surface processes take place over hours to years. These mass changes, which include earthquakes as well as movement of the atmosphere, hydrosphere, and ice sheets, constitute Earth's time-variable gravity (TVG) field. The observation of TVG is critical to understanding sea-level rise, terrestrial water storage, ice sheet melting, and other climatic processes. Of particular importance are certain components of low-degree, large-scale TVG signals to which dedicated gravity missions, such as the Gravity Recovery and Climate Experiment (GRACE), lack sensitivity. Alternative methods are therefore favored for estimating these parameters. Satellite Laser Ranging (SLR) is a proven technique with applications to many areas of fundamental geodesy. Through a constellation of passive satellites and network of ground tracking stations, SLR delivers more accurate estimates of low-degree gravity coefficients, which allows for validation and enhancement of the GRACE data.

This work uses high-fidelity numerical simulations to investigate potential improvements to SLR-derived gravity estimates. First, existing simulation techniques are further developed for application to SLR. A combination of real data and geophysical models ensures realistic tracking statistics in the simulation. Potential new SLR satellites are investigated at various altitudes and inclinations, with a particular focus on the inclination after it is determined to be more impactful. It is found that the addition of a low-inclination satellite significantly improves the SLR gravity solution by introducing a unique sensitivity to the gravity field that decorrelates key coefficients. Several cases involving the addition of new ground stations are then investigated. In general, the filling of geographic gaps at the poles and in the Southern hemisphere reduces errors in the

recovered gravity field by improving the observing geometry. However, a hypothetical case involving a uniformly distributed ground network reveals that stations lack the ability to systematically improve SLR gravity estimates in the way that a new satellite can. Finally, the simulated SLR data are combined with simulated GRACE data to investigate a jointly inverted solution. The results show that this method fully leverages the information in the SLR data, which enhances the GRACE data more than a simple substitution of coefficients. The simulation environment provides a novel way to quantify the improvements from these rigorous combination solutions. A variety of global and regional techniques are applied to analyze these solutions.

Dedication

To my grandfathers, Ed Finkle and Ron Tucker.

Acknowledgements

I would first like to thank my advisor, Professor Steve Nerem, for bringing me into his lab and supporting me throughout my studies. His academic and professional guidance have greatly improved all aspects of my research abilities. I would also like to thank Dr. Bryant Loomis for serving on my committee and for his mentorship. Bryant showed incredible generosity with his time by hosting me at GSFC on two occasions as well as through his willingness to answer questions, discuss results, and provide feedback. I am grateful for the valuable support of the rest of my committee members: Professor Marcus Holzinger, Professor Jay McMahon, and Dr. Felix Landerer. I would also like to acknowledge Kenny Rachlin for kindly providing technical assistance on many aspects of GEODYN and SLR.

Thank you to all my friends in the Nerem group for the fun times. I am especially grateful to Alexa, Eduard, and Carlos for the input they provided along the way. Finally, I would like to thank my parents for their unwavering support over the years.

This work was funded by the NASA FINESST program through grant 80NSSC20K1611, and by a CU Boulder CIRES Graduate Student Research Award. Several sources have also supported conference presentations of this work: the CCAR Bahls Travel Award, the Graduate and Professional Student Government, and the Graduate School.

Contents

Chapter

Tables

Table

Figures

Figure

Chapter 1

Introduction

1.1 Historical Overview

The concept of Satellite Laser Ranging (SLR) dates back nearly to the time of the first artificial Earth satellite. Just 5 years after the launch of Sputnik 1 in 1957, Tavenner [1962] proposed the following:

> "Largos, the laser-activated reflecting geodetic optical satellite, is a system that is envisioned as a solution to these problems of stero-triangulation (sic). Numerous prismatic reflectors, which have the property of reflecting any ray of light falling upon them back to the source of the light ray, are placed on a satellite. A laser, which has the property of concentrating coherent light in a narrow beam, is the source of light used in this system. Lasers, located at each ground observing station, beam light pulses activated by a common triggering circuit to the satellite. The satellite reflects each signal to its respective source, where the signal is recorded on a photographic plate against a background of stars." (p. 3602)

Thus, the role of the satellite in SLR is passive; it simply carries at least one reflector whose purpose is to return a laser pulse from a ground station. Following the orbit insertion failure of Beacon Explorer-A in March 1964, the Beacon Explorer-B (BE-B/Explorer 22) with its retroreflector assembly launched successfully in October 1964 [Plotkin et al., 1965]. Over the following month, a coordinated effort between NASA Goddard Spaceflight Center (GSFC) in Greenbelt, MD and the General Electric Company in Phoenix, AZ led to the first observations of laser reflections from BE-B as signals on an oscilloscope [Plotkin et al., 1965; Snyder et al., 1965]. Beacon-C (BE-C), also carrying a reflector assembly, launched in April 1965 and remains a tracking target to this day despite the end of its primary mission in 1973 (ILRS/GSFC). The laser hardware at this time

achieved ranges with meter-level precision [Degnan, 1985]. Although Lunar Laser Ranging developed during this era and is closely related to SLR, it will not be covered here but the reader is referred to Kokurin [2003] for more details.

The first dedicated SLR satellites, Starlette and the Laser Geodynamics Satellite (LAGEOS), were launched in 1975 and 1976, respectively, with the goal of providing high quality data for geodetic investigations [Pearlman et al., 2019]. Both satellites are spin-stabilized passive spheres containing numerous corner cube reflectors. LAGEOS, for example, measures 60 cm in diameter, weighs 441 kg, and contains 426 corner cube reflectors [Degnan, 1985]. The key benefits of this design are summarized as follows:

(1) *Spherical*: This "cannonball" shape simplifies the modeling of non-conservative forces and center of mass corrections. It also permits attitude-independent ranging.

(2) *Passive*: That the satellites contain no active instruments reduces costs by eliminating the need for several subsystems (thermal, power, communications, etc.). Consumables do not limit the mission duration.

(3) *Dense*: A low area-to-mass ratio reduces effects and errors from non-conservative forces and slows orbital decay allowing a mission duration of many decades.

Of course, there are drawbacks to this design such as an inability to maneuver in case of orbital insertion error or for collision avoidance. An abundance of Earth orbiters, including CubeSats, altimetry satellites, and GNSS satellites, carry and have carried corner cube assemblies for primary or redundant orbit determination using laser ranging [Pearlman et al., 2019]. One can make a subtle distinction between these satellites with active payloads that carry a corner cube(s) and the passive *geodetic* SLR satellites that are the focus of this thesis.

The hardware component of SLR ground stations is largely taken for granted throughout this work, but its development cannot be completely ignored. The laser, timing, and tracking assemblies are a critical part of successful, accurate, and consistent SLR. The laser used in the first SLR

experiments was a Q-switched ruby laser with a telescope receiver mounted on a repurposed Nike-Ajax radar system [Plotkin et al., 1965]. Modern laser assemblies with sub-cm accuracy, such as NASA's Space Geodesy Satellite Laser Ranging (SGSLR) system, utilize Nd:YAG lasers operating with kHz frequency and picosecond pulse widths [McGarry et al., 2019; Pearlman et al., 2019]. Because SLR is done at optical wavelengths, it cannot occur through clouds; at the same time, it is unaffected during transit through the ionosphere [Pearlman et al., 2019]. Advancements to in-situ meteorological instruments at ground stations have led to more accurate data for atmospheric corrections [McGarry et al., 2019]. Nearly all SLR ground stations require human operation or oversight, but the trend towards automation of ground stations will increase the amount and consistency of SLR data [Horvath et al., 2014]. McGarry et al. [2019] report more aspects of modern SLR ground station hardware. Figure 1.1 shows a simplified overview of SLR operations. Safety systems can vary between stations but their general function is to cease ranging operations if it detects an aircraft nearby.

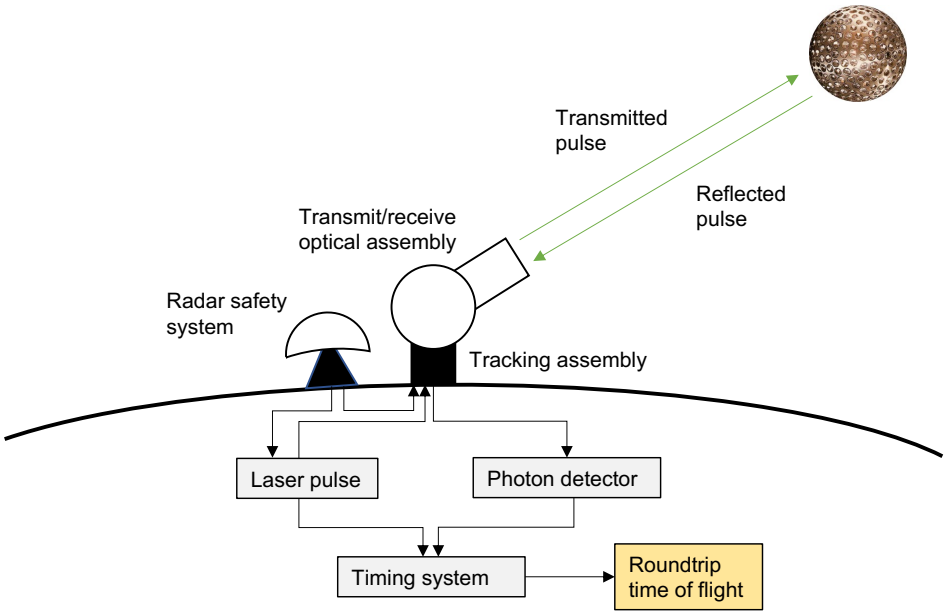

Figure 1.1: Simplified schematic of SLR operations. Satellite image from ILRS/GSFC.

SLR has remained an attractive technique due to its simplicity; the fundamental observable

is the roundtrip travel time of a laser pulse (Figure 1.1). The ground stations and observations to laser ranging satellites are broadly overseen and archived by the International Laser Ranging Service (ILRS), which was established in 1997 and today consists of over 75 organizations in 30 countries [Pearlman et al., 2002, 2019]. The remainder of this chapter presents necessary context to situate the research in this thesis. The current SLR space segment and ground network are discussed in more detail. Modern applications of SLR are explored, with particular emphasis on its important role in measuring time-variable gravity (TVG) notwithstanding the advent of more modern techniques. It will be shown that investigating new SLR satellites, ground stations, and joint solutions with GRACE to improve TVG is a critically under-studied area that this dissertation addresses.

1.2 Current SLR Network

1.2.1 Space Segment

Table 1.1 lists 12 SLR satellites and their properties. Larets orbits with the lowest mean altitude at just 691 km, while the Etalon pair orbit at over 19,000 km. Beacon-C is the only non-spherical satellite listed and has the lowest inclination at 41°, while LAGEOS-1 has the "largest" inclination at 109.9°, although Stella, Larets, and BLITS are nearer to polar in their sun-synchronous orbits inclined around 98°. The BLITS satellite is no longer tracked following a collision with space debris in 2013, and its successor BLITS-M failed to separate after launch in 2019 [Parkhomenko et al., 2013, ILRS/GSFC[1]]. Both Beacon-C and Starlette have the most eccentric orbits ($e \approx 0.02$), which causes their altitude to vary by about 300 km between apsides. The LAser RElativity Satellite, LARES, has the lowest area-to-mass ratio and is the densest object currently orbiting in the Solar System; its primary mission is to investigate the relativistic frame-dragging effect [Ciufolini et al., 2012]. Section 1.3 discusses the critical contribution of this satellite in more detail. The recently launched LARES-2 complements LAGEOS-1 to facilitate studies of relativistic phenomena.

Of the 12 satellites presented in Table 1.1, 7 of them will be the primary focus of this thesis

[1] https://ilrs.gsfc.nasa.gov/missions/satellite_missions/past_missions/blit_general.html

("SLR7"): LAGEOS-1/2, Starlette, Stella, AJISAI, Larets, and LARES. The Etalon satellites, due to their altitude, lack sensitivity to the temporal gravity field. The new LARES-2 satellite also has a high altitude that will limit its usefulness in TVG studies. Beacon-C is excluded from this work due to its irregular shape and susceptibility to large non-gravitational perturbations [Sośnica et al., 2015]. Additionally, the satellite is geomagnetically stabilized, which makes it unobservable throughout large swaths of the Southern hemisphere [Cheng et al., 1997]. The selected SLR7 match the satellites used in the current Technical Note 14 that supplements GRACE data [Loomis et al., 2019, 2020].

1.2.2 Ground Segment

The ground segment of the ILRS consists of over 40 stations conducting SLR and Lunar laser ranging, but this number fluctuates for several reasons including, but not limited to, technical issues, hardware upgrades, and/or staffing [Pearlman et al., 2019]. Figure 1.2 shows a map of SLR stations that form the "baseline" network in this work. The network is notably denser in the Northern hemisphere and has gaps near the equator and mid to high southern latitudes. The level of hardware and automation varies between stations, which can lead to different qualities and quantities of data. As mentioned previously, SLR operations cannot occur through clouds, meaning that local weather conditions also play a role in a station's productivity. Finally, it should be noted that a station's latitude coupled with a satellite's altitude and inclination dictates the overall observability of a given station-satellite configuration.

1.3 The Contemporary Role of SLR

Though simple in concept, SLR has supported numerous operational and scientific goals over its history. This section reviews many of SLR's capabilities with a particular emphasis on estimating low-degree gravity fields as this is central to this thesis. However, SLR's role in fundamental geodesy is also presented for completeness and to demonstrate the critical need to maintain and advance its infrastructure.

Table 1.1: SLR satellite orbits and properties

Mission (Country)	**Launch Year**	**Altitude** (km)	**Inclination** (degree)	**Eccentricity**	**Area-to-mass** ($m^2\ kg^{-1} \times 10^{-4}$)	$\mathbf{C_R}$
Beacon-C (USA)	1965	940-1300	41	0.024	180	1.08
Starlette (France)	1975	800-1100	49.8	0.020	9.6	1.134
LAGEOS-1 (USA)	1976	5860	109.9	0.0039	6.9	1.146
AJISAI (Japan)	1986	1500	50	0.0016	58	1.040
Etalon-1 & 2 (USSR)	1989	19140	65	0.0006	9.3	1.22/1.25
LAGEOS-2 (USA)	1992	5620	52.7	0.014	7.0	1.111
Stella (France)	1993	830	98.6	0.0010	9.4	1.125
Larets (Russia)	2003	691	98.2	0.0017	15	1.003
BLITS (Russia)	2009	832	98.8	0.0016	30	1.10
LARES (Italy)	2012	1450	69.5	0.014	2.7	1.105
LARES-2 (Italy)	2022	5896	70.1	< 0.0025	4.7	ND

C_R = coefficient of reflectivity, ND = no data available. Data from Sośnica et al. [2015], Torrence et al. [1995], ILRS/GSFC, and Kenny Rachlin (personal communication).

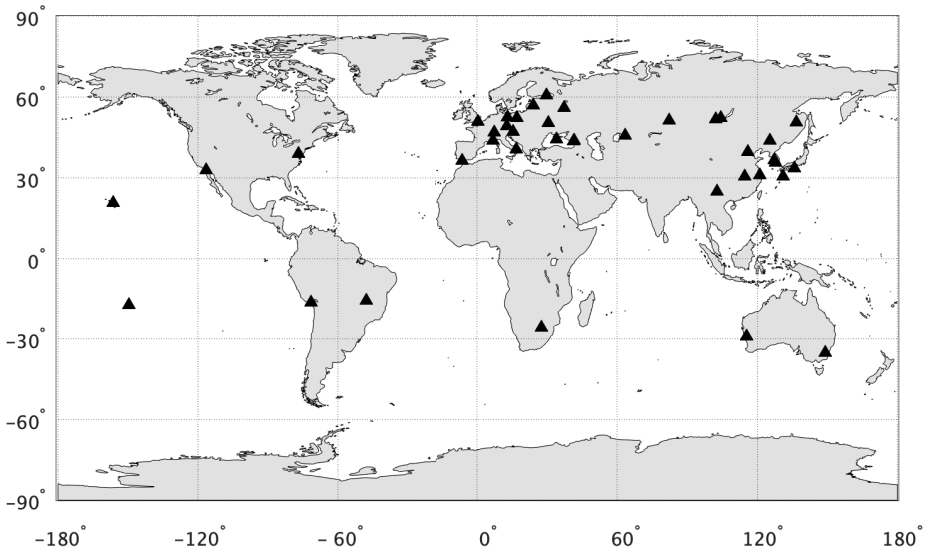

Figure 1.2: Map of current SLR stations.

1.3.1 In Support of GRACE

Since 2002, GRACE (2002-2017) and GRACE-FO (2018-present) have measured temporal changes in Earth's gravity field with unprecedented spatiotemporal resolution. The satellites primarily use a microwave ranging instrument to continuously observe inter-satellite range, which depends on terrestrial gravitational anomalies and non-gravitational forces (e.g. drag). After accounting for the non-gravitational forces using on-board accelerometer data, Earth's gravity field is then computed on a monthly basis. Though several different basis functions have been used, the focus here is on spherical harmonics (see Chapter 2). GRACE can estimate up to about degree and order 90 for monthly solutions, corresponding to a spatial resolution of about 400 km [Tapley et al., 2004b, 2019; Landerer et al., 2020]. Movement of surface water (liquid and ice) causes much of the monthly time-variable gravity signal, which allows one to infer ice-sheet melting, changes in global ocean mass, and variations in terrestrial water storage [e.g., Velicogna, 2009; Chen et al., 2020; Rodell et al., 2018]. The GRACE data also reveal motion of the solid Earth: secularly from glacial isostatic adjustment (GIA) and episodically from large earthquakes [Peltier et al., 2015; Han et al., 2006].

The low-degree spherical harmonic gravity coefficients contain signals from large-scale movement of ice and water, making their contribution particularly strong in certain scientific applications [Chen et al., 2005; Su et al., 2020]. Early on in the GRACE mission it was discovered that SLR more accurately estimates the $C_{2,0}$ harmonic, which describes Earth's oblateness ($J_2 = -C_{2,0}\sqrt{5}$) [Cheng and Ries, 2017]. GRACE-derived values of $C_{2,0}$ contain a $\sim$160-day signal that has been described as "tide-like" aliasing from the S_2 ocean tide [Chen et al., 2009]. Recent work, however, demonstrates the signal likely comes from thermally-induced accelerometer errors related to the beta-prime angle of the orbit [Cheng and Ries, 2017]. Though GRACE $C_{2,0}$ estimates have improved with subsequent data releases, the GRACE Science Data System recommends replacement of this harmonic with SLR-derived values that are released as Technical Notes (TN) [Landerer et al., 2020]. Figure 1.3 compares GRACE and SLR estimates of $C_{2,0}$ and shows the presence of

the nuisance ∼160-day signal in the GRACE estimate.

From Figure 1.3 it is clear that the SLR $C_{2,0}$ estimate is more reliable than GRACE. However, differences also exist between SLR estimates depending on the applied processing. Loomis et al. [2019] included a TVG forward model in their data processing, which led to new $C_{2,0}$ estimates released as part of TN-14. This altered the trend in $C_{2,0}$ over 2005-2015 to -2.38×10^{-11}/year compared to -1.73×10^{-11}/year in TN-11, the predecessor to TN-14 [Loomis et al., 2019; Cheng and Ries, 2017]. Given $C_{2,0}$'s magnitude, this modification affects rates in global mean sea level, Antarctica, and Greenland by 0.08 mm/year, -15.4 Gt/year, and -3.5 Gt/year, respectively [Loomis et al., 2019]. Cheng and Ries [2023] recently presented several updated versions of TN-11 where they process the data with a TVG forward model (TN-11G) or a least squares adjusted empirical orthogonal function (EOF) approach (TN-11E). The linear $C_{2,0}$ rates of these updated products generally agree with TN-14, but their annual amplitude is up to $\sim$ 50% larger. Currently, only TN-11E could be downloaded[2] , although CSR has another $C_{2,0}$ product[3] (RL-06) that includes a forward model but seems separate from TN-11G in Cheng and Ries [2023]. Regardless, the introduction of the forward model means that the SLR solutions are no longer completely independent. Even with these recent advances, the discrepancies in annual amplitude and overall magnitude of $C_{2,0}$ reveal the need to seek further improvements of this coefficient. Chapter 4 discusses this topic in more detail.

Inspection of Figure 1.3 shows a further degradation of the GRACE data beginning in late 2016. This is linked to the use of only a single accelerometer beginning in November 2016 and for the entirety of GRACE-FO [Loomis et al., 2020]. On GRACE-B (GRACE) the accelerometer was turned off in the final months to reduce power requirements, whereas the GRACE-D (GRACE-FO) accelerometer performs worse than expected [Loomis et al., 2020; Landerer et al., 2020]. In both cases, a "transplant" algorithm is used that leverages the observations from the functioning instrument [Bandikova et al., 2019; Landerer et al., 2020]. Importantly, Loomis et al. [2020]

[2] `https://ftp.csr.utexas.edu/pub/slr/TN11E/TN11E.txt` Accessed: 23 May 2023
[3] `https://ftp.csr.utexas.edu/pub/slr/degree_2/C20_RL06.txt` Accessed: 23 May 2023

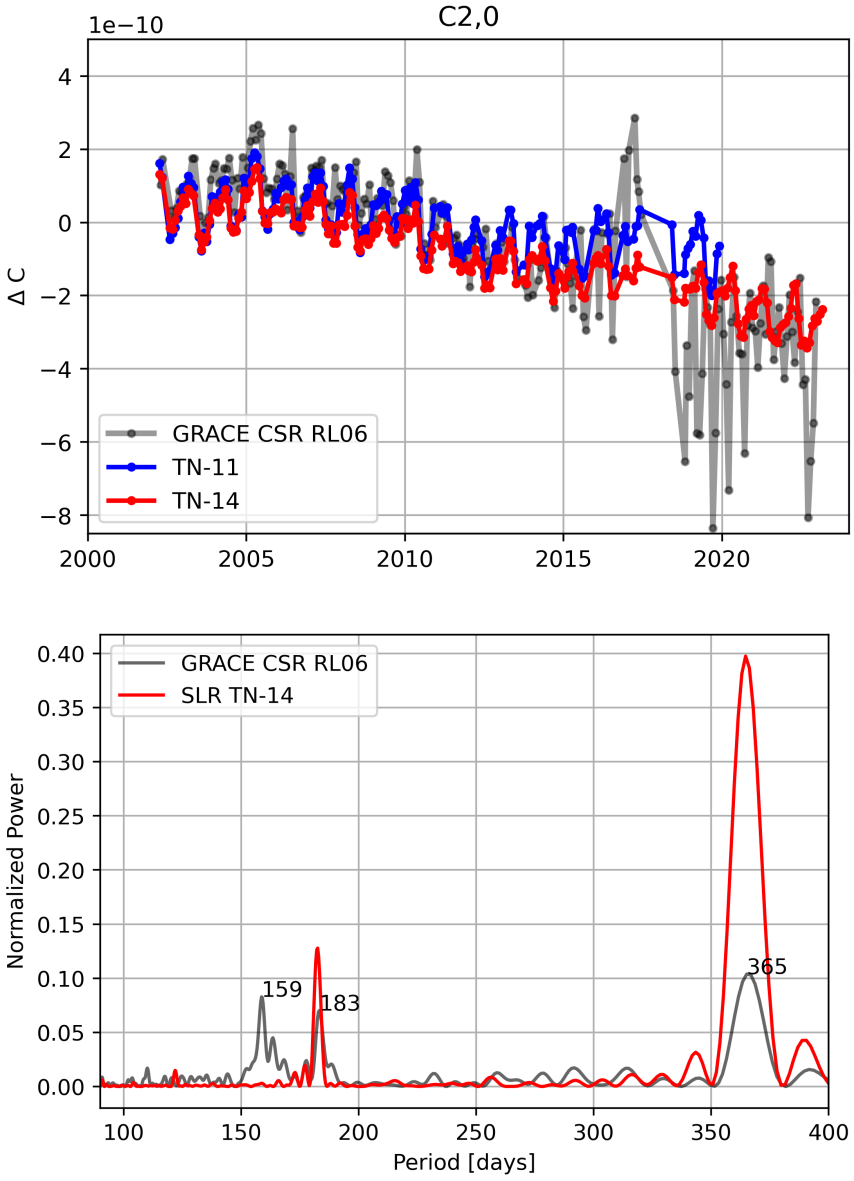

Figure 1.3: Top: Comparison of $C_{2,0}$ from GRACE (grey), SLR TN-11 (blue), and SLR TN-14 (red). Bottom: Periodogram of GRACE and SLR TN-14 $C_{2,0}$ estimates.

demonstrate that the single-accelerometer period also impacts GRACE $C_{3,0}$ estimates as seen in Figure 1.4. During March 2012 to July 2016, where GRACE had both accelerometers, the RMS of the difference between GRACE and SLR $C_{3,0}$ estimates is 2.4×10^{-11}; this value increases by a factor of three during the single accelerometer period [Loomis et al., 2020]. This has expanded SLR's role in providing estimates of low-degree zonal coefficients. An equally striking feature of Figure 1.4 is the poor SLR estimates of the odd zonals before 2012. This is due to the substantial contribution of the LARES satellite, which launched in 2012 (Table 1.1). Relative to other SLR satellites, LARES has a unique altitude, inclination, and area-to-mass ratio, which means it provides sensitivity that greatly improves SLR-based recovery of these odd zonals [Sośnica et al., 2015; Loomis et al., 2020]. Loomis et al. [2020] report that replacing GRACE $C_{3,0}$ with SLR values during the single accelerometer period modifies the trend in Antarctic ice-sheet mass loss from -92 ± 54 Gt yr^{-1} to -170 ± 43 Gt yr^{-1}. Thus, it is now conventional to replace GRACE $C_{3,0}$ with post-LARES SLR estimates [Landerer et al., 2020].

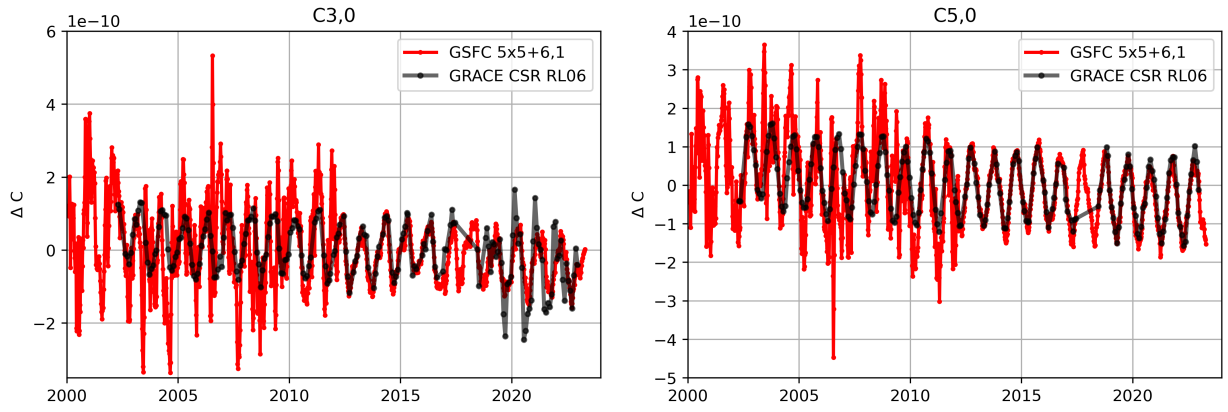

Figure 1.4: GRACE (grey) and SLR (red) $C_{3,0}$ and $C_{5,0}$ timeseries.

Directly substituting SLR $C_{2,0}$ and $C_{3,0}$ into GRACE solutions naturally raises questions as to (1) whether this approach is mathematically optimal and (2) whether this approach neglects useful information about other coefficients in the SLR data. Independent SLR solutions are limited to a maximum degree of ∼5. While the SLR data are sensitive to higher degrees, gravity coefficients of the same degree parity and order cannot always be separated as they induce perturbations

of the same frequency on a given satellite [Kaula, 1966]. This effect manifests as correlations between gravity coefficients in the SLR solution [Loomis et al., 2020; Cheng and Ries, 2017; Sośnica et al., 2015]. For example, the magnitude of the correlation coefficient for $C_{2,0}/C_{4,0}$ is ≥ 0.5 and ≥ 0.8 for $C_{3,0}/C_{5,0}$ [Loomis et al., 2020, 2019; Sośnica et al., 2015]. The inclusion of *a priori* information in the SLR data processing mitigates the impact of these correlations, but the value of the formal parameter correlations often remains unaffected [Loomis et al., 2019]. Thus, a simple substitution of coefficients at the solution level fails to account for these correlations. Recent work has shown promising results from so-called combination solutions, where the GRACE and SLR normal equations are merged prior to the final inversion to obtain a joint solution [Kang et al., 2022; Haberkorn et al., 2016]. These results have shown that, depending on the relative weighting, the SLR data can contribute to resolving the low-degree zonals as well as the GRACE resonant orders (integer multiples of $m \approx 15$) [Kang et al., 2022; Haberkorn et al., 2016]. Despite these studies, the substitution method for SLR $C_{2,0}$ and $C_{3,0}$ is still overwhelmingly used when processing GRACE gravity fields for scientific applications. Chapter 6 discusses and investigates these combination solutions in more detail.

SLR remains an essential part of satellite gravimetry despite GRACE's success. A typical monthly GRACE gravity field has over 3,000 coefficients, yet simply modifying 2 of these coefficients has been shown to have wide ranging scientific implications. SLR gravity solutions continue to improve and are an area of ongoing research. The impact of LARES guides the work in Chapter 4, while the demonstrated importance of low-degree gravity fields motivates the investigations in Chapters 5 and 6.

1.3.2 Continuity of Observations

SLR has existed decades longer than GRACE and can provide time-variable $C_{2,0}$ estimates back to 1976 and estimates up to about degree 4 back to 1993 [e.g., Lemoine et al., 2006; Cheng et al., 2013a; Zelensky et al., 2014]. However, one must exercise caution as Table 1.1 shows the number of satellites varies over the years and Figure 1.4 shows how adding satellites can change

TVG solutions. Nevertheless, SLR has the capability to provide *some* record of TVG in the pre-GRACE era albeit with a coarse resolution. Talpe et al. [2017] used principal component analysis to combine the spatial modes of GRACE (assumed stationary pre-GRACE) with SLR/DORIS and reconstructed smoothed mass change timeseries of the polar ice sheets back to 1993. To get ice mass change back to 1994, Bonin et al. [2018] applied an inversion technique that used predefined regions, but ultimately faced significant challenges in separating the Greenland and Antarctic signals with a 5×5 SLR gravity field[4] .

The GRACE data in Figures 1.3 and 1.4 reveal an approximately one year gap between GRACE and GRACE-FO from mid 2017 to mid 2018. Such gaps in the record are not ideal because a loss in continuity between GRACE and GRACE-FO can make identifying biases in GRACE-FO difficult [Landerer et al., 2020]. To bridge this gap and validate GRACE-FO it is necessary to look at independent data sources. The technique presented by Bonin et al. [2018] showed promise in filling inter-mission gaps, but would benefit from higher resolution SLR data. Ongoing work by Loomis [2019] has sought to maintain continuity through the estimation of large SLR-derived mass concentration block ("mascons"), and future additions to the SLR network could enhance the resolution of this method. Other gap-filling techniques have relied on combinations with secondary data, such as kinematic orbits from the ESA Swarm satellites, which are several years into their extended mission [Meyer et al., 2019]. An improvement of independent SLR gravity solutions would significantly benefit these gap-filling methods. GRACE-FO is at the end of its prime 5-year mission and faces challenges related to increasing solar activity, the faulty accelerometer, and a leaky thruster [Landerer et al., 2022]. Its successor is planned to launch no sooner than late 2027; this could give a $\sim$1 year overlap, but another data gap remains a real possibility given these confounding variables [Landerer et al., 2022; Wiese et al., 2022].

[4] Note that the $n \times m$ notation refers to a gravity field complete to degree n and order m. Rarely is $m \neq n$ when using this notation.

1.3.3 Other Geodetic Applications of SLR

Though the main purpose of this work centers on TVG, SLR data have historically been used for reference frame determination and Earth orientation parameters (EOPs). The International Earth Rotation Service (IERS) defines and maintains a set of conventions for The International Terrestrial Reference System (ITRS), an Earth-centered Earth-fixed coordinate system [Bloßfeld, 2015]. The ITRS is realized every few years as the International Terrestrial Reference Frame (ITRF) consisting of a set of crust-fixed station coordinates computed from four geodetic techniques: GNSS, SLR, VLBI, and DORIS [Bloßfeld, 2015]. The origin of the ITRF (center of mass from long-term observation) is uniquely realized through SLR because Earth-orbiting satellites move about the instantaneous center of mass; the dynamic difference between these two origins, called geocenter motion, captures global scale mass redistribution and solid-Earth signals [Cheng et al., 2013b]. GRACE cannot resolve geocenter (degree-1 spherical harmonics) motion since it orbits about Earth's center of mass. There are several ways to obtain degree-1 coefficients for use in GRACE data products, each having certain advantages and disadvantages. While the "dynamic" method could be used to estimate these coefficients directly, this is not typically done because it requires the introduction of a Coriolis-like term in the equations of motion to account for the non-inertial frame [Wu et al., 2012; Cheng et al., 2013b]. Alternatively, one could use the "kinematic" approach to directly estimate the center-of-mass/center-of-figure offset or the "network shift" approach that estimates geocenter motion through the translational Helmert parameters [Yu et al., 2021; Cheng et al., 2013b]. For supplementing GRACE data, "inverse" methods that leverage surface mass observations and model outputs are also quite common [Sun et al., 2016; Swenson et al., 2008].

The ITRF is related to the quasi-inertial International Celestial Reference Frame (ICRF) through a set of EOPs: Universal Time (UT1), pole coordinates, and pole offsets from precession and nutation. Two of these parameters, pole coordinates and excess length of day (related to UT1), can be derived from SLR data [Bloßfeld et al., 2018]. There is decades of literature surrounding

SLR's important role in this capacity and the reader is referred to Bloßfeld [2015] for further information. Uniquely, SLR is the only technique that contributes to measuring all 3 of the "pillars of geodesy": the Earth's geometric shape, rotation, and gravity field [Bloßfeld, 2015].

1.4 Previous SLR Simulation Studies

Most SLR TVG studies focus on processing real data, and little work has been done thus far to quantify the effect of an expanded network on TVG. There exists an extensive body of literature surrounding so-called "mass-change simulations" that focus overwhelmingly on spatiotemporal improvements and future constellations for GRACE-like or, more generally, satellite-satellite tracking (SST) configurations [e.g., Deccia et al., 2022; Hauk and Wiese, 2020; Loomis et al., 2012; Wiese et al., 2012]. No reviewed literature has applied these analysis techniques to investigate SLR TVG despite the consistently important need to have such estimates. Otsubo et al. [2016] simulated a new ground station to quantify potential improvements to geodetic parameters. They used six satellites (SLR7 minus Larets) and simulated 134 virtual stations placed at 15 by 30 degree intervals of latitude and longitude, respectively. From this, they compute reductions in formal errors for translation and scale components of the reference frame and for a single 60-day 4×4 gravity field with a single new station. The simulated data do not contain force model errors and the authors only consider the formal covariance matrices. Maier et al. [2012] ran a simulation only to investigate the maximum degree that 5 SLR satellites (SLR7 minus Larets and LARES) could recover, but do not consider time-variable effects or potential network additions.

Kehm et al. [2018] used methods similar to SST simulation studies to investigate the effect of an improved SLR ground segment on EOPs and ITRF parameters. They simulate (1) improved tracking statistics with the current network and (2) improved network geometry from eight potential future stations. As the focus of their study is geodetic reference frames, Kehm et al. [2018] use only 5 satellites (Etalon-1&2, LAGEOS-1&2, and LARES) and do not consider Stokes coefficients. Kehm et al. [2019] continued this work by simulating a grid of stations similar to Otsubo et al. [2016], again looking only at reference frame parameters. Additional work by Glaser et al. [2019]

simulated improved network geometry using a list of future stations as in Kehm et al. [2018]. This work was also in the context of reference frame parameters and additionally looked at combined TRF solutions with other techniques (GPS, VLBI). Their simulation considers neither force model uncertainty nor gravity parameter estimation. However, they discuss station tracking statistics using total cloud cover as a proxy which is relevant to the simulation development in this thesis.

1.5 Project Overview

The 2017 Earth Science Decadal Survey recognizes mass change as a designated observable, highlighting the need to accurately continue this unique record [National Academies of Sciences, Engineering, and Medicine, 2018]. While GRACE and GRACE-FO have produced groundbreaking results, operational and data processing challenges have underscored the importance of redundancy in the mass-change observing system. Although SLR will never replace GRACE for measuring TVG, it continues to play an increasingly important role in measuring the low-degree gravity field, which broadly captures changes in ice mass, ocean mass, and terrestrial water storage. SLR as an independent technique not only delivers critical support to GRACE, but also could provide continuity and validation of the large-scale TVG record [Chen et al., 2022]. This is especially true if the resolution and accuracy of the SLR results were improved. Overall, this idea guides the direction of this thesis.

The LARES satellite significantly improved SLR estimates of the odd-zonal temporal gravity coefficients. Yet, despite this known impact of a single satellite, no reviewed literature systematically investigates future SLR satellites for improving gravity estimates. However, numerous studies have cited the importance of using SLR satellites at various altitudes and inclinations to provide the most reliable gravity solutions [Bloßfeld et al., 2018; Sośnica et al., 2015; Bloßfeld et al., 2015; Cheng et al., 1997]. Of course, the space segment comprises only one part of SLR, which leads one naturally to question the potential impact on TVG from future ground stations. The newly developed SLR simulation environment also permits a novel investigation of combining SLR and GRACE data to fully leverage the information in each data set.

A clear motivation and need to investigate future SLR additions and its current role with GRACE has been established. This work consists of six additional chapters as described below. Additionally, these results have produced two journal articles: Tucker et al. [2022] corresponding to Chapter 4 and Tucker et al. [2023] corresponding to Chapter 5.

- *Chapter 2*: The mathematical expressions for Earth's gravity field are developed. An overview of estimation theory is presented to show how gravity is estimated from satellite orbits. Finally, combining data from different sources and simulation performance metrics are shown.

- *Chapter 3*: The numerical simulation is developed and validated. Sources of error, tracking statistics, and force models are defined.

- *Chapter 4*: Results from investigating a new SLR satellite are presented. The orbit search space is narrowed to consist of altitude and inclination. It is shown that the addition of a low-inclination SLR satellite improves recovery of low-degree TVG coefficients by decorrelating certain coupled terms.

- *Chapter 5*: Results from investigating new SLR stations are presented. Several realistic and boundary cases are studied to explore possible improvements from new stations. Though less impactful than a new satellite, new stations that fill geographic gaps can constrain existing SLR TVG estimates.

- *Chapter 6*: The simulated SLR data are combined with simulated GRACE data to solve for a single set of gravity coefficients. The benefits and improvements from using this method are analyzed and discussed.

- *Chapter 7*: The work in this dissertation is summarized and recommendations are made.

Chapter 2

Theory

2.1 Overview

This chapter presents the mathematical formulation of the methods and analysis techniques used in this work.

2.2 Gravity

Although SLR has several geodetic capabilities, this project largely focuses on its role in determining the time-variable gravity field. The following equations also generally apply to representing the gravity field with GRACE estimates. This section presents the geopotential as spherical harmonics and reviews key properties associated with this basis. The geoid is also defined and time variations in the gravity field are represented in terms of the spherical harmonic coefficients.

2.2.1 Gravitational Potential

This section presents a relevant overview of Earth's gravity field, with more details available in [Kaula, 1966; Torge, 2001; Vallado, 2013]. For a point mass exterior to Earth's surface, the gravitational potential V satisfies Laplace's equation

$$\nabla^2 V = \frac{\partial^2 V}{\partial x^2} + \frac{\partial^2 V}{\partial y^2} + \frac{\partial^2 V}{\partial z^2} = 0 \tag{2.1}$$

The above expression can be transformed to spherical coordinates and solved with separation of variables to get a *harmonic* function. Let the gravitational potential in terms of radial distance

from the origin r, latitude ϕ, and longitude λ (Figure 2.1) be $V(r, \phi, \lambda)$. Then the it can be shown that

$$V(r,\phi,\lambda) = \frac{GM}{r}\sum_{n=0}^{\infty}\sum_{m=0}^{n}\left(\frac{r_E}{r}\right)^n P_{nm}(\sin\phi)[C_{nm}\cos(m\lambda) + S_{nm}\sin(m\lambda)] \tag{2.2}$$

where G is the gravitational constant, M is Earth's mass, r_E is Earth's mean equatorial radius, $P_{nm}(\sin\phi)$ is the associated Legendre function of degree n and order m, and C_{nm} and S_{nm} are the dimensionless spherical harmonic coefficients. The associated Legendre functions can be computed using equations 1.29-1.30 in Kaula [1966]. In practice, the outer summation in Eq. 2.2 is truncated at some finite degree n_{max}. One could also explicitly factor out the degree 0 terms, which represents the potential of a spherically symmetric mass distribution. If the coordinate system is taken as the body's center of mass, then the degree 1 terms are zero.

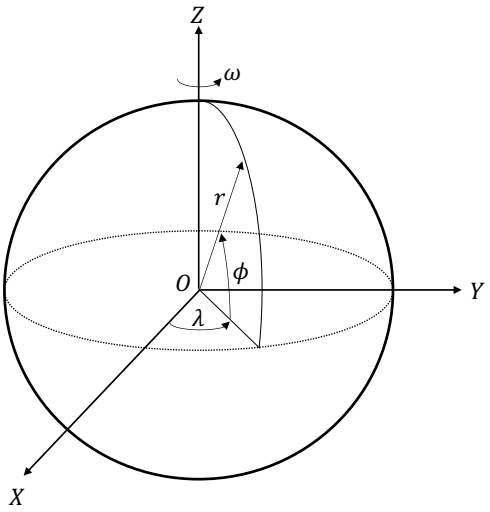

Figure 2.1: Geometry of Earth-centered Earth-fixed frame and spherical coordinates.

Conventionally, the associated Legendre function and spherical harmonic ("Stokes") coefficients are presented fully normalized such that [Vallado, 2013]:

$$\bar{C}_{nm} = \Pi_{nm}C_{nm}, \quad \bar{S}_{nm} = \Pi_{nm}S_{nm}, \quad \bar{P}_{nm} = \frac{P_{nm}}{\Pi_{nm}} \tag{2.3}$$

$$\Pi_{nm} = \left[\frac{(n+m)!}{(n-m)!k(2n+1)}\right]^{1/2} \qquad k = \begin{cases} 1 & m = 0 \\ 2 & m \neq 0 \end{cases} \tag{2.4}$$

Equation 2.3 can be substituted into Eq. 2.2. Some texts use "J" notation for the $m = 0$ terms with $-C_{n0} = J_n$. Note that this expression involves the unnormalized spherical harmonic coefficient and that S_{n0} is zero by definition. Unless otherwise stated, the results will assume the coefficients are fully normalized and the overbar may be dropped for convenience. Rearranging and letting $\mu = GM$, Eq. 2.2 becomes

$$V(r, \phi, \lambda) = \frac{\mu}{r} + \frac{\mu}{r} \sum_{n=2}^{n_{max}} \sum_{m=0}^{n} \left(\frac{r_E}{r}\right)^n \bar{P}_{nm}(\sin\phi)[\bar{C}_{nm}\cos(m\lambda) + \bar{S}_{nm}\sin(m\lambda)] \tag{2.5}$$

2.2.2 Spherical Harmonics Nomenclature & Properties

Spherical harmonics, akin to a Fourier series on a sphere, are a convenient basis to represent the gravity field given the aspherical shape of the Earth. Although there exist other basis functions for the gravity field, this work will only use spherical harmonics. The spherical harmonics are orthogonal and constitute an independent basis, making them ideal to represent functions on a sphere. The degree and order of the spherical harmonic determines lines where the function goes to zero on the sphere. Categorizing these harmonics will highlight certain properties that aid in their interpretation (Figure 2.2).

The *zonal* harmonics arise when $m = 0$. These are symmetric about the pole and have no longitudinal dependence. Zeroes occur at n bands of latitude. The largest gravitational perturbation on a satellite due to Earth's shape comes from Earth's equatorial bulge. As seen in Figure 2.2, J_2 describes this oblateness and is about 3 orders of magnitude larger than the next largest coefficient, J_3 [Vallado, 2013]. Accurate recovery of J_2 is therefore critical to quantifying large-scale mass distribution.

When $m > 0$ and $n \neq m$, the spherical harmonics take on a tile-like appearance and are called *tesserals*. These vanish along $2m$ meridians and $l - m$ latitudes. Due to their spatial pattern, they are important for describing regional variations. The final case occurs when $n = m$, which gives rise to the *sectoral* harmonics. With zeros along $2n$ meridians, these are independent of latitude and account for longitudinal variations in mass distribution.

From Figure 2.2 it is apparent that the spatial resolution becomes smaller with increasing

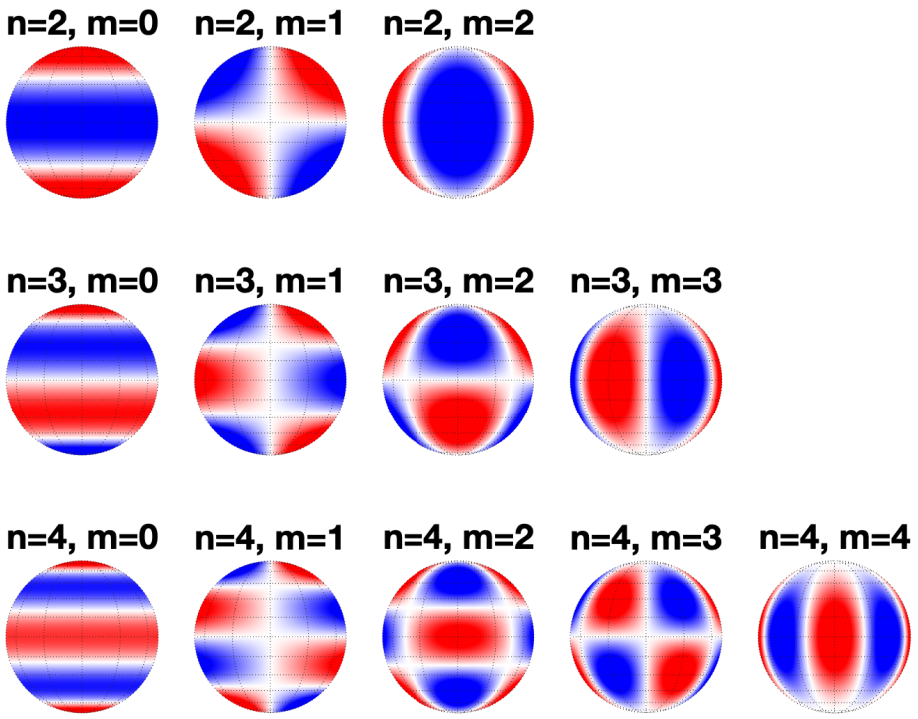

Figure 2.2: Examples of zonal ($m = 0$), tesseral ($m > 0,\ m \neq n$), and sectoral ($m = n$) spherical harmonics.

degree. The spatial half-wavelength λ_n of a spherical harmonic of degree n can be approximated as [Wahr et al., 1998]:

$$\lambda_n \approx \frac{20000}{n} \text{ km} \tag{2.6}$$

Therefore, the spatial resolution of a gravity field to degree 5 is about 4000 km, while the resolution of a field to degree 60 is about 330 km.

2.2.3 The Geoid

The *reference ellipsoid* approximates Earth's shape as an oblate spheroid with the equatorial and polar radii corresponding to the semi-major a and semi-minor b axes, respectively [Vallado, 2013]. Its shape may also be reported as flattening $f = (a - b)/a$. The *geoid* is the equipotential surface that coincides with mean sea level (MSL) and deviates from the reference ellipsoid due to density inhomogeneities [Torge, 2001; Vallado, 2013]. As shown in Figure 2.3, the topography does not necessarily coincide with the geoid. By definition, the gravity vector is always perpendicular to the geoid surface. The potential on the geoid is defined as the *potential of gravity*, or W, which is the sum of the gravitational potential V and rotational potential [Kaula, 1966]:

$$W(r, \phi, \lambda) = V(r, \phi, \lambda) + \frac{1}{2}\omega^2 r^2 \cos^2 \phi \tag{2.7}$$

where ω is the rotation rate of the Earth.

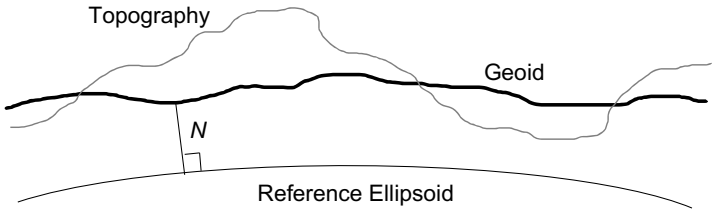

Figure 2.3: Relationship between reference ellipsoid, geoid, topography, and geoid height N.

A point P has potential U_P with respect to the reference ellipsoid. Let the disturbing potential T_P be [Torge, 2001],

$$T_P = W_P - U_P \tag{2.8}$$

Note that the rotational potential differences out of Eq. 2.8. Using Eq. 2.5 one finds,

$$T = \frac{\mu}{r} \sum_{n=2}^{\infty} \sum_{m=0}^{n} \left(\frac{r_E}{r} \right)^n \bar{P}_{nm}(\sin\phi)[\bar{C}^*_{nm} \cos(m\lambda) + \bar{S}_{nm} \sin(m\lambda)] \tag{2.9}$$

with $\bar{C}^*_{nm} = \bar{C}^{obs}_{nm} - \bar{C}^{ref}_{nm}$. The reference ellipsoid is defined with $\bar{C}^{ref}_{nm}$, which comprises only even zonal harmonics [Torge, 2001]. Applying Brun's formula to obtain geoid height N,

$$N = \frac{T}{\gamma} \tag{2.10}$$

with normal gravity $\gamma = \mu/r^2$. Using a spherical approximation for the normal gravity leads to

$$N = r_E \sum_{n=2}^{\infty} \sum_{m=0}^{n} \bar{P}_{nm}(\sin\phi)[\bar{C}^*_{nm} \cos(m\lambda) + \bar{S}_{nm} \sin(m\lambda)] \tag{2.11}$$

The focus of this work is time-variable gravity. This can be expressed as variations about some mean field or other value such that Eq. 2.11 is modified to give,

$$\Delta N = r_E \sum_{n=2}^{\infty} \sum_{m=0}^{n} \bar{P}_{nm}(\sin\phi)[\Delta\bar{C}_{nm}(t) \cos(m\lambda) + \Delta\bar{S}_{nm}(t) \sin(m\lambda)] \tag{2.12}$$

where the temporal dependence of the Stokes coefficients is shown explicitly, but will subsequently be implied.

2.2.4 Surface Mass Density

It is often insightful to represent changes in the gravity field in terms of surface mass density. At the sub-monthly to annual scale most sources of mass change, and hence time-variable gravity, are confined to a layer near or on Earth's surface. Other sources, such as atmospheric contributions, can be removed during data processing. Suppose the density inducing a temporal geoid change is $\Delta\rho(r, \phi, \lambda)$ and that it is concentrated in a thin layer at Earth's surface [Wahr et al., 1998]. The surface density $\Delta\sigma$ has units mass per area and is defined as [Wahr et al., 1998]

$$\Delta\sigma(\phi, \lambda) = \int_{\text{thin layer}} \Delta\rho(r, \phi, \lambda) dr \tag{2.13}$$

which ultimately leads to the following expression given by Wahr et al. [1998]:

$$\Delta\sigma(\phi, \lambda) = \frac{r_E \rho_{avg}}{3} \sum_{n=0}^{\infty} \sum_{m=0}^{n} \frac{2n+1}{1+k_n} \bar{P}_{nm}(\sin\phi)[\Delta\bar{C}_{nm} \cos(m\lambda) + \Delta\bar{S}_{nm} \sin(m\lambda)] \tag{2.14}$$

In Eq. 2.14 ρ_{avg} is the Earth's mean density and k_n is the degree-dependent load love number that represents the Earth's response to a surface load. Surface mass anomalies can be expressed in terms of equivalent water height (EWH or w.e.), which is intuitive since movement of water and ice drives monthly time-variable gravity. One simply divides $\Delta\sigma$ (in mass per area, e.g. kg/m^2) by the density of water p_w to convert to units of equivalent water height.

2.3 Least Squares Estimation

Here we seek to determine a set of n parameters specifying a spacecraft's trajectory from a set of m observations. In nearly all cases $m > n$, which leads to an overdetermined problem. A statistical framework becomes necessary to estimate the "best" values of the parameters. GEODYN, the selected orbit determination and parameter estimation software (see Section 3.2), uses a partitioned Bayesian least squares method. The details of least squares estimation will be presented following Tapley et al. [2004a].

The n dimensional state vector contains all parameters to be estimated and can be expressed as,

$$\mathbf{X} = [\mathbf{r} \quad \mathbf{v} \quad \boldsymbol{\alpha}]^T \tag{2.15}$$

where $\mathbf{r}$ and $\mathbf{v}$ are the satellite position and velocity vectors respectively, and $\boldsymbol{\alpha}$ contains other parameters to be estimated. One can make the distinction between "arc" parameters specific to each satellite arc (position, velocity, drag coefficients) and "global" parameters common to the combined solution (gravity coefficients). The nonlinear dynamics and measurement models can be expressed as,

$$\dot{\mathbf{X}} = F(\mathbf{X}, t) \quad \mathbf{X}(t_k) \equiv \mathbf{X}_k \tag{2.16}$$

$$\mathbf{Y}_i = G(\mathbf{X}_i, t_i) + \boldsymbol{\epsilon}_i \quad i = 1, \ldots, l \tag{2.17}$$

where $\mathbf{Y}_i$ is a p-dimensional set of observations $i = 1, \ldots, l$, $m = p \times l$, and $\boldsymbol{\epsilon}_i$ represents measurement noise or error. With a reasonable reference trajectory $\mathbf{X}^*$, one can define the state and

observation deviation vectors, respectively,

$$\mathbf{x}(t) = \mathbf{X}(t) - \mathbf{X}^*(t), \quad \mathbf{y}(t) = \mathbf{Y}(t) - \mathbf{Y}^*(t) \tag{2.18}$$

Equations 2.16 and 2.17 are linearized through expansion into a first-order Taylor series and combined with Eq. 2.18 to get

$$\dot{\mathbf{x}}(t) = A(t)\mathbf{x}(t), \quad \mathbf{y}_i = \tilde{H}_i \mathbf{x}_i + \boldsymbol{\epsilon}_i \tag{2.19}$$

where

$$A(t) = \left[\frac{\partial F(t)}{\partial \mathbf{X}(t)}\right]^* \quad \tilde{H}_i = \left[\frac{\partial G}{\partial \mathbf{X}}\right]_i^* \tag{2.20}$$

and $[\ ]^*$ indicates evaluation of the partials with the reference solution. The solution to the first expression of Eq. 2.19 can be expressed as

$$\mathbf{x}(t) = \Phi(t, t_k)\mathbf{x}_k \tag{2.21}$$

where the state transition matrix $\Phi(t, t_k)$ satisfies the following

$$\dot{\Phi}(t, t_0) = A(t)\Phi(t, t_0) \quad \Phi(t_0, t_0) = I \tag{2.22}$$

The second expression of Eq. 2.19 can be expressed in terms of the state at a single epoch $\mathbf{x}_k$

$$\mathbf{y} = H\mathbf{x} + \boldsymbol{\epsilon} \tag{2.23}$$

where the k subscript is dropped for convenience and

$$\mathbf{y} \equiv \begin{bmatrix} y_1 \\ \vdots \\ y_l \end{bmatrix}, \quad H \equiv \begin{bmatrix} \tilde{H}_1\Phi(t_1, t_k) \\ \vdots \\ \tilde{H}_l\Phi(t_l, t_k) \end{bmatrix}, \quad \boldsymbol{\epsilon} \equiv \begin{bmatrix} \epsilon_1 \\ \vdots \\ \epsilon_l \end{bmatrix} \tag{2.24}$$

In the Eq. 2.23 the total number of observations is $m = pl$, $\mathbf{y}$ is $m \times 1$, $\mathbf{x}$ is $n \times 1$, H is $m \times n$, and $\boldsymbol{\epsilon}$ is $m \times 1$. Typically $\boldsymbol{\epsilon}$ is assumed zero-mean and independent such that

$$E(\boldsymbol{\epsilon}) = [0 \ \cdots \ 0]^T, \quad E(\boldsymbol{\epsilon}\boldsymbol{\epsilon}^T) = R = \begin{bmatrix} \sigma_1^2 & \cdots & 0 \\ \vdots & \ddots & \vdots \\ 0 & \cdots & \sigma_m^2 \end{bmatrix} \tag{2.25}$$

The least squares solution estimates $\mathbf{x}$ such that the weighted sum of squared residuals is minimized,

$$J(\mathbf{x}) = 1/2\boldsymbol{\epsilon}^T R^{-1}\boldsymbol{\epsilon} = 1/2\boldsymbol{\epsilon}^T W\boldsymbol{\epsilon} \tag{2.26}$$

If the estimate of $\mathbf{x}$ is $\hat{\mathbf{x}}$, then it can be shown that the *normal equation* reads

$$H^T W H\hat{\mathbf{x}} = H^T W\mathbf{y} \tag{2.27}$$

where the $n \times n$ *normal matrix* is $H^T WH$. Equation 2.27 has the well-known solution

$$\hat{\mathbf{x}} = (H^T WH)^{-1} H^T W\mathbf{y} \tag{2.28}$$

2.4 Combining Data

As mentioned in 2.3, the state vector $\mathbf{x}$ contains the arc and global parameters for each satellite. The data for a particular satellite are processed in arcs to balance error accumulation with spatiotemporal coverage. For a given timespan it is desired that data from all satellites contribute to the estimation of the global terms (gravity coefficients). The data in this dissertation will be combined at the normal equation level (Eq. 2.27) and inverted for a common set of parameters (Eq. 2.28).

Recall, for a given satellite, the normal matrix $N = H^T WH$ has dimensions $n \times n$ and the right hand side $\mathbf{b} = H^T W\mathbf{y}$ is $n \times 1$. The size of n can vary between satellites because it is composed of n_a arc parameters and n_g global parameters. A complete combination of arc and global parameters would therefore require augmentation of either the H or N matrices. However, the arc parameters can be estimated implicitly, or "reduced", such that the size of N is reduced to n_g. This will be derived following [Kaula, 1966; Bloßfeld, 2015]. First, the normal equation is partitioned into arc (subscript 1) and global (subscript 2) parts,

$$\begin{bmatrix} N_{11} & N_{12} \\ N_{21} & N_{22} \end{bmatrix} \begin{bmatrix} \hat{\mathbf{x}}_1 \\ \hat{\mathbf{x}}_2 \end{bmatrix} = \begin{bmatrix} \mathbf{b}_1 \\ \mathbf{b}_2 \end{bmatrix} \tag{2.29}$$

Through Gaussian elimination this reduces to,

$$\begin{bmatrix} I_{n_a} & N_{11}^{-1}N_{12} \\ 0 & N_{22} - N_{12}^T N_{11}^{-1} N_{12} \end{bmatrix} \begin{bmatrix} \hat{\mathbf{x}}_1 \\ \hat{\mathbf{x}}_2 \end{bmatrix} = \begin{bmatrix} N_{11}^{-1}\mathbf{b}_1 \\ \mathbf{b}_2 - N_{12}^T N_{11}^{-1}\mathbf{b}_1 \end{bmatrix} \tag{2.30}$$

From the second row of Eq. 2.30,

$$\tilde{N} = N_{22} - N_{12}^T N_{11}^{-1} N_{12} \tag{2.31}$$

$$\tilde{\mathbf{b}} = \mathbf{b}_2 - N_{12}^T N_{11}^{-1}\mathbf{b}_1 \tag{2.32}$$

Therefore, the reduced normal equation system reads,

$$\tilde{N}\hat{\mathbf{x}}_2 = \tilde{\mathbf{b}} \tag{2.33}$$

GEODYN iterates on the arc parameters until convergence before writing out the normal equations. Once this process is complete for all satellites and data arcs, the normal equation files are supplied to the Ncombine/Nsolve software packages provided by NASA/GSFC. This reduces, combines, and solves for the individual normal equations. A series of functions implementing the partitioning and reduction were also developed for applications requiring additional flexibility. These were validated with results from Ncombine/Nsolve. The combined system is simply a superposition of j normal equation systems [Bloßfeld, 2015]:

$$\tilde{N}_c = \sum_{i=1}^{j} \lambda_i \tilde{N}_i \tag{2.34}$$

$$\tilde{\mathbf{b}}_c = \sum_{i=1}^{j} \lambda_i \tilde{\mathbf{b}}_i \tag{2.35}$$

where λ_i is a weighting factor for the i-th normal equation.

2.5 Performance Indicators

The main goal of this work ultimately involves assessing improvements to SLR gravity solutions with simulated additions to the baseline solution. Furthermore, the truth is known with a simulation and this will be leveraged in the analysis. Here, several equations are presented that are used in the analyses throughout this dissertation.

The *degree variance* is defined as,

$$\sigma_n^2 = \sum_{m=0}^{n} (\Delta\bar{C}_{nm}^2 + \Delta\bar{S}_{nm}^2) \tag{2.36}$$

where the C and S can represent the full signal or the difference (error) between the estimated and truth values. Terminology can vary, but generally the square root of the degree variance is known as the degree amplitude or degree RMS (root mean square). It may also be called the error degree RMS depending on the coefficients used in the calculation. While Eq. 2.36 produces a dimensionless value, one can scale it by r_E^2 to obtain the geoid degree variance [Torge, 2001; Wahr et al., 1998]. Observe also that a simple modification of Eq. 2.36 would allow one to express the errors in terms of the order m. The order-wise formulation is less often used, but is insightful in certain analyses.

Suppose X is a random vector. Then the symmetric *variance-covariance* matrix P is given by [Tapley et al., 2004a],

$$P = E[(X - E[X])(X - E[X])^T] = \begin{bmatrix} var(X_1) & cov(X_1, X_2) & \cdots & cov(X_1, X_n) \\ cov(X_2, X_1) & var(X_2) & \cdots & cov(X_2, X_n) \\ \vdots & \vdots & \ddots & \vdots \\ cov(X_n, X_1) & cov(X_n, X_2) & \cdots & var(X_n) \end{bmatrix} \tag{2.37}$$

where $E[\cdot]$ is the expected value, *var* is the variance also denoted σ_i^2, and *cov* is the covariance. The correlation coefficient ρ_{ij} can take on values from $[-1, 1]$ and it describes the linear correlation between two elements of X,

$$\rho_{ij} = \frac{cov(X_i, X_j)}{\sigma_i \sigma_j} \tag{2.38}$$

The matrix in Eq. 2.37 can be reformulated in terms of ρ to produce the *correlation matrix* in which the diagonal values necessarily equal one and the off-diagonal elements follow from Eq. 2.38. Returning to the orbit determination problem, Tapley et al. [2004a] show that the *estimation error covariance matrix* can be computed as

$$P = E[(\hat{\mathbf{x}} - \mathbf{x})(\hat{\mathbf{x}} - \mathbf{x})^T] = (H^T W H)^{-1} \tag{2.39}$$

The square root of the diagonal elements of this matrix give the standard deviations or *formal errors*, and one can also readily form the correlation matrix from Eq. 2.38. Both the formal errors and correlation coefficients will be used throughout this thesis.

The scalar RMS describes the magnitude of variations in some parameter,

$$RMS = \sqrt{\frac{1}{N}\sum_{i=0}^{N}\xi_i^2} \tag{2.40}$$

Often in this thesis, the RMS error (RMSE) will be reported where ξ represents the difference between two values such as the truth and estimate.

2.6 Analytical Considerations

Although this project relies primarily on numerical techniques, one can still gain valuable insight from analytical methods. Orbital perturbations allow SLR to function as a technique to recover time-variable gravity. To solve for increasingly complex gravity fields or to reduce errors, it is therefore necessary to (1) have SLR *satellites* sensitive to particular aspects of the gravity field and (2) form solutions with multiple satellites in varied orbits. Additions to the ground segment, while important, cannot make up for intrinsic deficiencies in the constellation's sensitivity to gravity as seen in Chapter 5. Analyzing a satellite's sensitivity to gravitational perturbations will provide first-order insights to inform the numerical approach. This analytical approach is idealized in many respects– it considers only first-order linear effects and it does not account for satellite visibility. Additionally, the perturbation on a particular orbital element may be non-unique; that is, the perturbation on the argument of periapsis, for example, could be caused by gravitational or drag-like forces.

Following [Kaula, 1966; Vallado, 2013], the potential in Eq. 2.5 is transformed and represented in terms of orbital elements,

$$V = \frac{\mu}{r} + \sum_{n=2}^{\infty}\sum_{m=0}^{n}\sum_{p=0}^{n}\sum_{q=-\infty}^{\infty}\frac{\mu}{r}\left(\frac{r_E}{r}\right)^n F_{nmp}(i)G_{npq}(e)S_{nmpq}(\omega, M, \Omega, \theta_{GMST}) \tag{2.41}$$

where $\theta_{GMST} = \omega_E(t - t_0)$, with ω_E equal to Earth's rotation rate. Expressions for the inclination and eccentricity functions, F and G, are given by Kaula [1966]. The function S in Eq. 2.41 is

expressed as,

$$S_{nmpq}(\omega, M, \Omega, \theta_{GMST}) = \begin{cases} C_{nm}\cos(\Theta_{nmpq}) + S_{nm}\sin(\Theta_{nmpq}), & (n-m) \text{ even} \\ -S_{nm}\cos(\Theta_{nmpq}) + C_{nm}\sin(\Theta_{nmpq}), & (n-m) \text{ odd} \end{cases} \tag{2.42}$$

$$\Theta_{nmpq} = (n-2p)\omega + (n-2p+q)M + m(\Omega - \theta_{GMST}) \tag{2.43}$$

Recall that the goal is to determine the effect of aspherical gravity on the satellite's orbital elements. The *Lagrange planetary equations* express time variations in the Keplerian elements due to conservative forces. These will not be presented here, but the reader is referred to [Kaula, 1966; Vallado, 2013] for the complete derivation and final expressions. Importantly, the Lagrange planetary equations require the disturbing potential in terms of orbital elements, which has been shown in Eq. 2.41.

SLR's primary role in gravity field determination has been estimation of the zonals and the remainder of this discussion will focus on its sensitivity to these coefficients. Notably, the even zonals uniquely induce secular variations of the orbit node, argument of periapsis, and mean anomaly. Considering only the secular part of the potential in Eq. 2.41 and substituting it in to the Lagrange equations, one finds the excitation Ψ_α of a particular orbital element α [Cheng, 1988; Cheng et al., 1989; Schutz et al., 1993; Cheng and Ries, 2017],

$$\frac{d\alpha}{dt} = \Delta\Psi_\alpha \approx \sum_n D_{\alpha,n}\delta J_n \tag{2.44}$$

where, for the even zonals, it can be shown that the excitation coefficients D_α of the orbit node are

$$D_{\Omega,n} = -\frac{\bar{n}}{\sin i}\left(\frac{R_E}{a}\right)^n G_{np0}(e)(1-e^2)^{-1/2}\frac{\partial F_{n0p}(i)}{\partial i} \qquad p = n/2,\ n = 2, 4, 6, \ldots \tag{2.45}$$

with $\bar{n}$ equal to the mean motion. One can also formulate an expression for excitations in the along-track, $T = M + \omega + \Omega\cos i$ similar to Eq. 2.45, but a number of forces besides gravity can affect this quantity [Yoder et al., 1983; Cheng, 1988]. It should be reemphasized that this section does not aim to present a comprehensive perturbation analysis, but instead seeks to provide a general framework to support numerical results. The odd zonals induce long-period variations in

eccentricity e and the argument of periapsis ω. However, analysis of these elements suffers from the same non-uniqueness as the along-track. Regardless, the eccentricity excitation is found to be,

$$D_{e,n} = (n-1)\bar{n}\left(\frac{R_E}{a}\right)^n F_{n0p}(i) \qquad p = (n-1)/2,\ n = 3, 5, 7, \ldots \tag{2.46}$$

Equations 2.45 and 2.46 have been used to quantify SLR satellites' sensitivity to the zonal harmonics [Cheng et al., 1989; Schutz et al., 1993; Cheng and Ries, 2017]. For a particular degree, the magnitude of the excitation coefficient shows a satellite's sensitivity to that coefficient. The overall perturbation, however, is a linear combination of the effects of multiple degrees as seen in Eq. 2.44. Taking the ratio $D_{\alpha,k}/D_{\alpha,j}$ shows the influence of higher degree k on lower degree j [Cheng and Ries, 2017]. A smaller ratio indicates better separability and provides information in a relative sense for a given satellite.

Chapter 3

Numerical SLR Simulations

3.1 Overview

As described in Section 1.4, numerical simulations have been used extensively to study gravity field recovery with SST configurations and, to a much lesser extent, SLR configurations. The benefit of a simulation is that the inputs are known and the effect of new SLR additions can be studied precisely. To apply these techniques to SLR requires some unique considerations that will be developed and discussed in this chapter. Additionally, tests are ran to ensure the simulation works as required.

3.2 Simulation Procedure

The simulation workflow generally follows the widely accepted methods of previous work such as Loomis et al. [2012] and Wiese et al. [2012]. A flowchart of the overall procedure is presented in Figure 3.1. In the first step, the orbit and station positions are defined and a set of *truth* force models is used to generate a set of *truth* observations. Zero-mean Gaussian noise with 1 cm standard deviation is then added to these *truth* station-satellite range data. The *nominal* run processes these noisy data using a slightly different set of force models to form the normal equations. The difference between the *truth* and *nominal* models represents the uncertainty in the process. Table 3.1 reports the simulation force models. NASA/GSFC's orbit determination and parameter estimation software GEODYN is used to simulate observations and calculate partial derivatives [McCarthy et al., 2015].

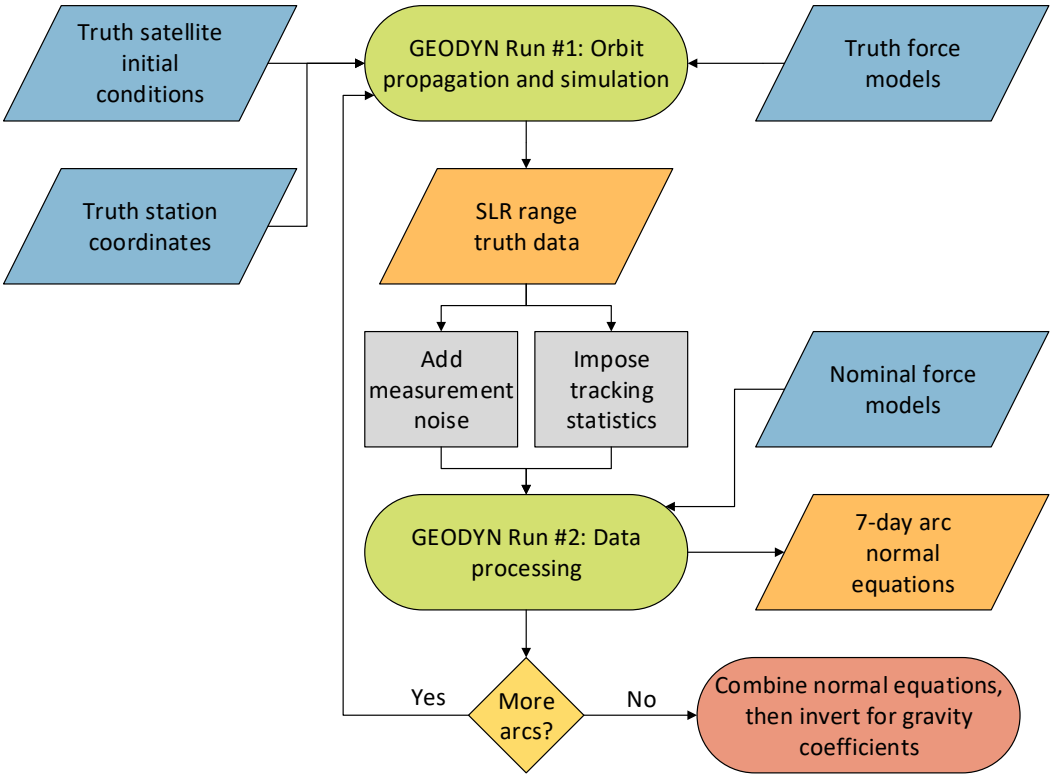

Figure 3.1: Overview of simulation procedure.

Table 3.1: Simulation Force Models

Force	**Truth Model**	**Nominal Model**
Static Gravity	GOCO06s	GOCO06s
Ocean Tides	EOT11a	FES 2014
Non-Tidal Atmosphere & Ocean	ESA ESM A+O	ESA ESM DEAL+AOerr
Hydrology & Ice	ESA ESM H+I	None

The time-varying gravity field is defined with respect to a static field. This work uses the GOCO06s model for static gravity to degree and order 180, though a much lower degree ($n_{max} \approx 60 - 90$) would be suitable in practice for SLR [Kvas et al., 2021]. Errors in the static gravity field are not considered since TVG is the primary signal of interest and the static field is generally well-known. The primary sources of high frequency mass redistribution are ocean and atmospheric tides, non-tidal atmosphere and ocean (e.g., weather), ice movement, and continental water movement. Ocean tides are given by the Empirical Ocean Tide (EOT) Model 11a in the *truth* case and the Finite Element Solution (FES) 2014 model in the *nominal* case [Savcenko and Bosch, 2012; Lyard et al., 2021].

Non-tidal atmospheric and oceanic variability presents a challenge for mass change missions due to undersampling and subsequent temporal aliasing of these high frequency signals according to the Nyquist-Shannon Sampling Theorem. To remove the high frequency non-tidal effects, one applies an atmosphere and ocean dealiasing model during data processing, such as AOD1B [Dobslaw et al., 2017]. In the *truth* run, the non-tidal atmosphere (A) and ocean (O) come from the simulation specific 6-hour ESA Earth System Model (ESM) [Dobslaw et al., 2015]. The ESA ESM also provides a realistically perturbed dealiasing model, DEAL+AOerr, which contain processes omitted by AOD1B and true errors across large and small scales [Dobslaw et al., 2016]. Thus, the dealiasing process in the simulation introduces errors as it would in actual data processing. Finally, the hydrology (H) and ice (I) signal is defined only in the *truth* run by ESA ESM H+I coefficients [Dobslaw et al., 2015]. The *nominal* run uses no a-priori hydrology or ice model as this is the signal of interest to recover independently in the simulation. Note that the *truth* signal for a given month is the mean of the 6-hourly sampled ESA ESM over that time period since higher frequencies cannot be resolved.

An example month of the TVG models is shown in Figure 3.2. Maps are displayed for the hydrology, ice, and atmosphere plus ocean components computed to degree and order 60 (i.e. GRACE resolution) and 10 (i.e. SLR resolution). Clearly, truncation of the maximum degree acts as a low-pass filter, meaning SLR will only recover long-wavelength signals. The hydrology signal

is strongest in the Amazon and sub-Saharan Africa, with smaller scale features throughout North America, Europe, Southeast Asia, and Northern Australia. The cryosphere signal predominantly comes from the ice sheets (Greenland and Antarctica) as well as major glacier systems (Alaska, Alps, and Himalayas). The atmosphere and ocean signal is overall weaker than HI, but shows signal over mid to high latitudes. Note that the magnitude of the signal for a given month is somewhat arbitrary as it represents a single point in a timeseries with respect to some mean or background field.

3.3 Satellite Modeling

The spherical shape of geodetic SLR satellites greatly simplifies certain aspects of the orbit determination process. Still, consideration must be given to the estimated parameters to reduce orbit and force model errors from leaking in to the gravity solution. Additionally, the results in this thesis will typically be from a timeseries; that is, a minimum of 1 year of data will be generated and analyzed. Whereas GRACE's groundtrack is reasonably consistent month-to-month (except during undesired short-repeat periods), SLR observations can vary in their monthly quantity and geographic distribution. A timeseries allows this variability to be captured versus analysis of only a single month. Furthermore, a timeseries allows the TVG signal to vary and creates a range of signal strengths across different geographic regions for analysis. This also allows investigation of seasonality in the analyses.

The arc parameterization is based on strategies derived from processing real SLR observations [Zelensky et al., 2014; Cheng and Ries, 2017, Kenny Rachlin (personal communication)], with modifications for a simulation environment. Each satellite's state is estimated once per arc. All SLR satellites are defined with a truth drag coefficient C_D equal to 2. No C_D are estimated for LAGEOS-1/2 due to their high altitude. For Starlette, Stella, AJISAI, Larets, and LARES, and the new satellite, C_D are estimated daily. A constant along-track acceleration term is estimated every 3.5 days for both LAGEOS satellites. No once-per-rev (1-cpr) empirical accelerations are estimated because these parameters, while effective at reducing force model errors, also absorb

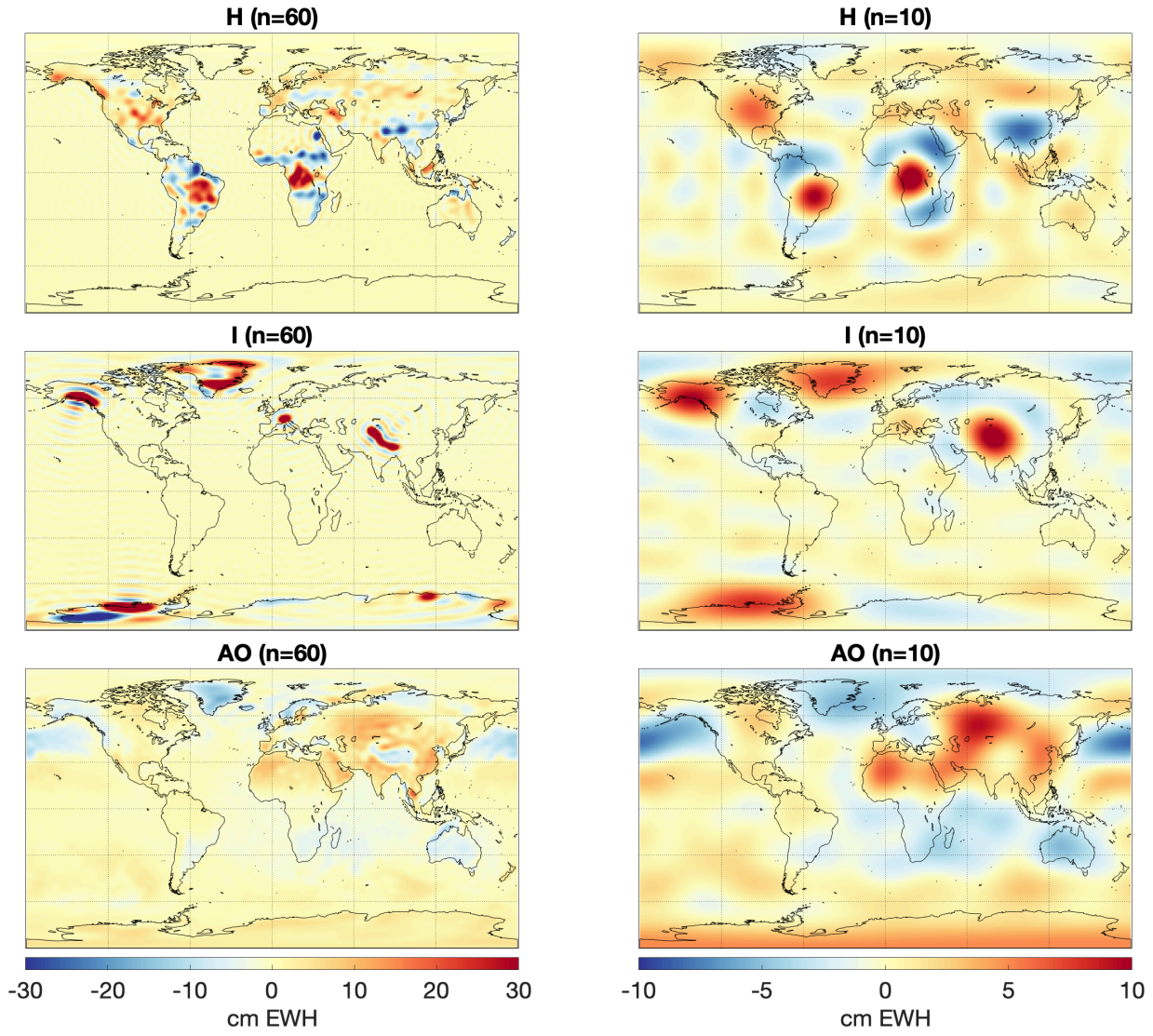

Figure 3.2: Example month of ESA ESM hydrology (H), ice (I), and atmosphere plus ocean (AO) computed in cm EWH to degree and order 60 (left column) and 10 (right column). Note the different colorbar limits for each column.

gravity signals of interest [Cheng and Ries, 2017; Nerem and Klosko, 1996]. In particular, the sine component of the LAGEOS cross-track 1-cpr term directly correlates to $C_{2,0}$ [Sośnica, 2014]. Solar radiation pressure is modeled with the coefficients of reflectivity C_R listed in Table 1.1. The new satellite is assigned an area-to-mass ratio equal to that of LARES.

All satellites are processed in 7-day arcs. At the end of each individual arc, partials for the arc parameters and global parameters (Section 2.3) are output. The global parameters are nominally Stokes coefficients for a $5\times5+C_{6,1}/S_{6,1}$ field, where the 6,1 term is estimated to improve the quality of $C_{2,1}$ [Loomis et al., 2019; Cheng and Ries, 2017]. Solutions are formed monthly by combining 4 7-day normal equations (Eqs. 2.33-2.35) from each satellite using the predefined weights given by Sośnica et al. [2015]. A final inversion of this combined system produces a unified gravity estimate using all available data.

3.4 Tracking Statistics

One particular aspect of SLR simulations that warrants discussion is the implementation of tracking statistics. SST missions are able to make continuous observations, which makes the groundtracks of their observation points fairly homogeneous and consistent. For SLR, the ground stations dictate the quantity and geographic distribution of observations. In an SLR simulation, one must therefore ensure the number of observations is realistic. Figure 3.3 displays a 1 month groundtrack of SLR7 observations, clearly showing the unbalanced geographic distribution.

For the SLR7, the most straightforward approach is to base the simulation tracking statistics on real data. To determine observation numbers and locations, real data files are used for the period beginning January 6, 2019. In all cases, a 15° elevation cutoff is used since stations often cannot observe satellites near the horizon due to trees or other obstacles. Determining the tracking statistics of a hypothetical satellite or ground station presents more of a challenge due to the numerous factors that influence different parts of the observing system (Sections 1.1 - 1.2). One approach is to simply assume a flat observation rate or station-based rates [Otsubo et al., 2016; Kehm et al., 2018, 2019]. The downside to this method is that the performance level of a new

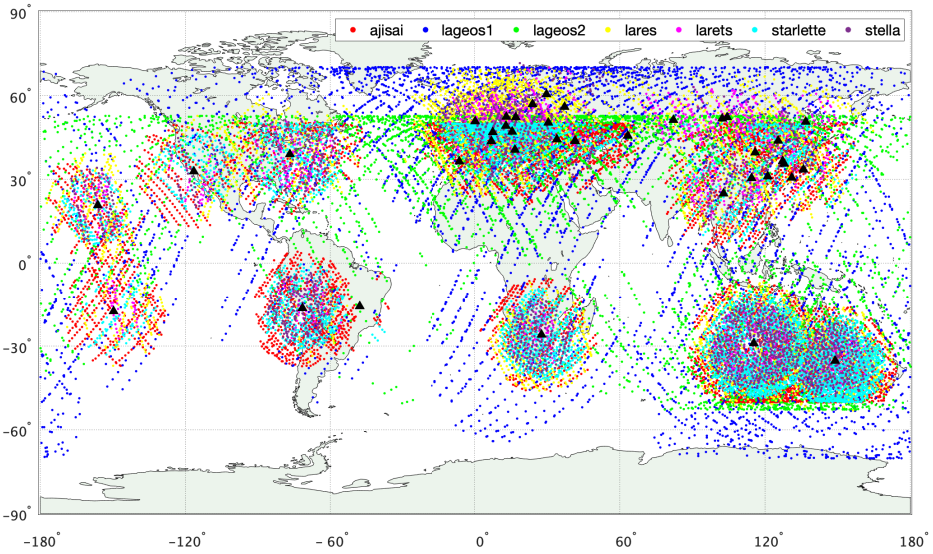

Figure 3.3: 1 month groundtrack of SLR observations to 7 satellites for the period beginning April 28, 2019.

station to a new satellite is unknown. Recognizing SLR's weather dependence, Glaser et al. [2019] averaged 6 years of total cloud cover (TCC) data and defined tracking based on (100-TCC)%. However, they found TCC too optimistic compared to actual tracking statistics and empirically downscaled the final observation percentage [Glaser et al., 2019].

In this work, the tracking statistics for new SLR additions are developed based on NCEP/DOE Reanalysis II total cloud cover data [Kanamitsu et al., 2002]. Figure 3.4 shows 2 example months as well as a 5-year mean of TCC. As one would expect, there is monthly variability that could correlate to SLR tracking. Thus, this spatiotemporal variability will be leveraged to produce the tracking statistics for this thesis. The pass selection scheme occurs in several steps described here. First, all possible passes are generated for a given station-satellite configuration. If the sky coverage exceeds 66% at the observing time and station, then the pass is discarded. For the remaining passes, a Bernoulli trial is then run with probability (1-TCC)/2.5, where TCC is expressed as a fraction. On a success, up to (1-TCC) of the pass is observed and on a failure it is discarded. Ultimately, this method encountered the same problem as in Glaser et al. [2019] regarding optimistic tracking with TCC alone, hence the downscaling factor that was selected to calibrate the number of simulated LARES observations to approximate the actual number over a timespan. The Bernoulli trial attempts to incorporate tracking criteria besides clouds (random success/fail), but there are limitations to the factors a simulation can model. Although the NCEP/DOE Reanalysis II model is somewhat dated, it suffices for its intended purpose in this work. Future work could improve this modeling, but the heuristic procedure here performs as required for the investigation.

3.5 Validation

The methodology and models of the simulation in this thesis have followed from established techniques for simulating mass-change missions. Nonetheless, it is worthwhile to validate the simulation performance through a few test cases. Although no simulation can perfectly reconstruct reality, we should still see the simulation behave as expected. To this end, the validation focuses on the effect of adding satellites as this is well-documented in recent work and is a central part of

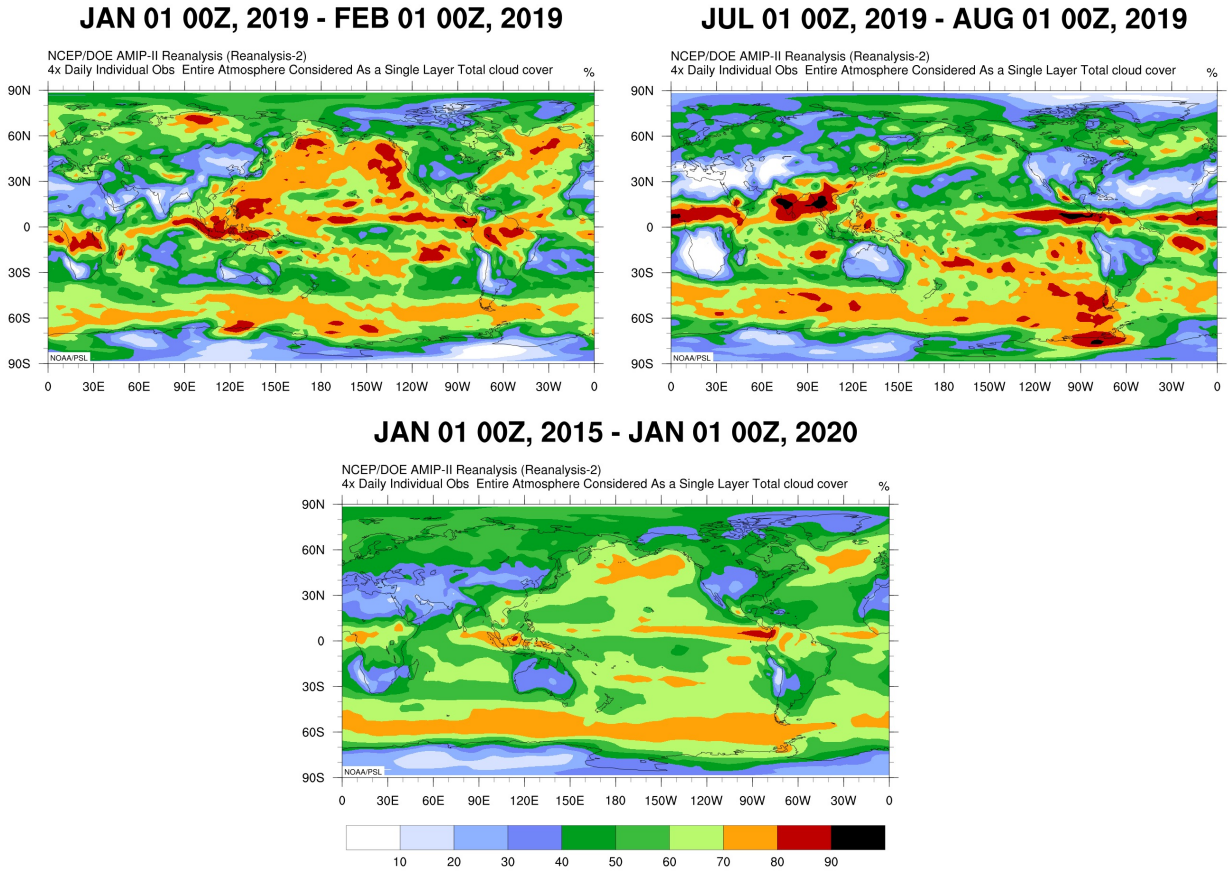

Figure 3.4: NCEP/DOE Reanalysis II TCC for 2 example months (top) and 5-year mean (bottom). Units are percent of sky covered. Plots generated from NOAA PSL (`https://psl.noaa.gov/data/gridded/data.ncep.reanalysis2.html` Accessed: 26 May 2023).

this thesis [e.g., Loomis et al., 2020].

Figure 3.5 shows the logarithm of the formal errors for 3 solutions: LAGEOS-1/2 only, SLR7 without LARES, and SLR7. In this context the formal errors are interpreted as the satellite's sensitivity to the respective coefficient [Sneeuw, 2000; Sośnica, 2014]. Historically, the LAGEOS satellites have been used to estimate temporal variations in the low-degree zonal coefficients [Nerem et al., 1993]. As expected, Figure 3.5 shows these satellites are most sensitive to the zonals. Due to their altitudes of over 5000 km, they lack sensitivity to degrees ≥ 4 as well as many tesserals and sectorals. Adding in the LEOs Ajisai, Starlette, Stella, and Larets, causes the sensitivity to all coefficients to increase by an order of magnitude. This behavior is expected since these satellites orbit at lower altitudes ($\leq$ 1500 km) with different inclinations and they are therefore more sensitive to perturbations from certain features. Finally, recent work by Loomis et al. [2020] reported improvements to $C_{3,0}$ with the addition of LARES in the solution. Comparing rows 2 and 3 of Figure 3.5, there is a marked increase in the sensitivity to $C_{3,0}$ with LARES in the solution. The formal error is reduced by about a factor of 2.5 for both $C_{3,0}$ and $C_{5,0}$, which compares well with the behavior reported in Loomis et al. [2020].

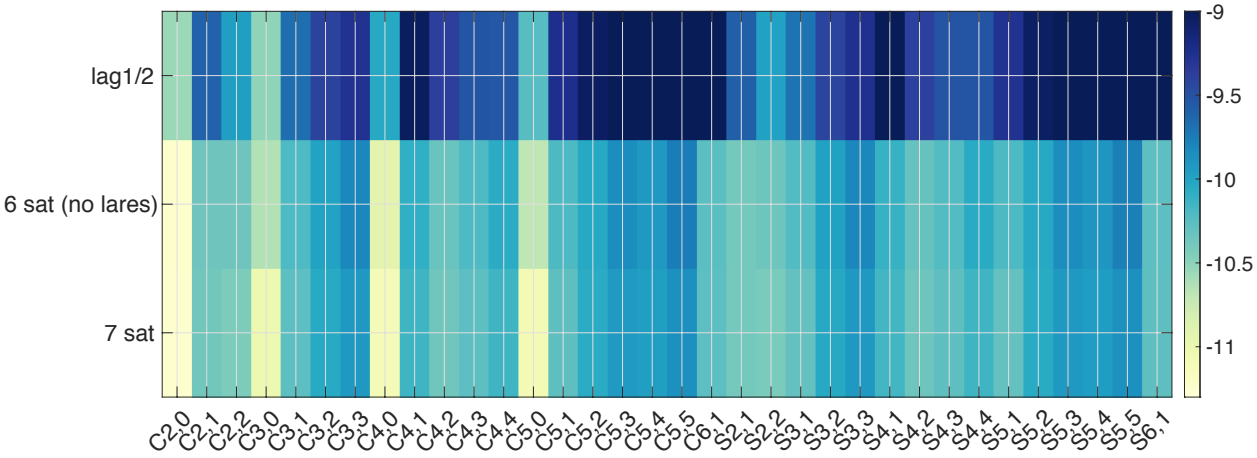

Figure 3.5: Logarithm of the formal errors for 2, 6, and 7-satellite solutions. Lag1/2 refers to the LAGEOS satellites.

As part of this work also focuses on parameter correlations, the simulation is further validated against this metric using the current network to ensure the models give reasonable results. Figure

3.6 reports the timeseries of correlations between the estimated zonal coefficients of the same parity. This figure confirms the simulation reproduces several key characteristics of the real solution. In their 5-satellite solutions, which are the same as the 6-satellite solution minus Larets in this work, both Cheng and Ries [2017] and Loomis et al. [2019] report $\rho^{C_{4,0}}_{C_{2,0}}$ values of about -0.4. The simulation value has strong agreement with this value. Larets' contribution is small and primarily impacts $C_{3,0}$ as well as some higher degree terms due to its orbit. In the actual data, adding LARES to the solution increases the magnitude of this even-zonal correlation by about 0.1, which is exactly the effect observed with the simulation [Bryant Loomis, personal communication; Cheng and Ries, 2017]. Without LARES, the odd zonals in actual solutions show a near perfect correlation with $\rho^{C_{5,0}}_{C_{3,0}} = -0.98$ [Loomis et al., 2020]. Adding LARES only slightly reduces the magnitude of this value by 0.1. Figure 3.6 confirms both of these characteristics with simulation data.

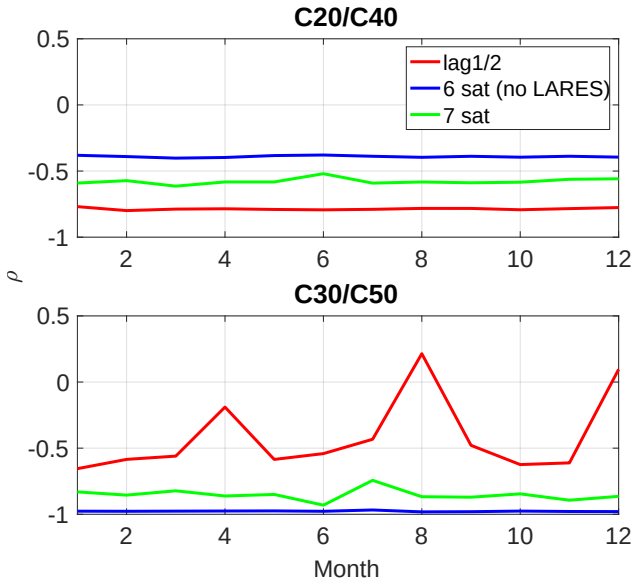

Figure 3.6: Timeseries of correlation coefficient for even zonals (top) and odd zonals (bottom).

Finally, the postfit range residuals are studied to verify their overall quality. Figure 3.7 displays timeseries of these residuals for the SLR7. In the real data, the LAGEOS orbits are consistently fit the best in an RMS sense. The simulation shows these orbits are fit to within the observation noise, which is zero-mean Gaussian with $\sigma = 1$ cm. Amongst the LEO satellites,

the Larets residuals have the most scatter. This is in agreement with actual data and is due to Larets' low altitude (690 km) and its relatively poor area-to-mass ratio. The remaining RMS of the residuals also appear as one would expect. The weighting applied to each normal equation in the combination is approximately proportional to the orbit qualities. However, *a priori* knowledge is also incorporated, such as the fact that LARES, because of its low area-to-mass ratio, is a more desirable target than Ajisai.

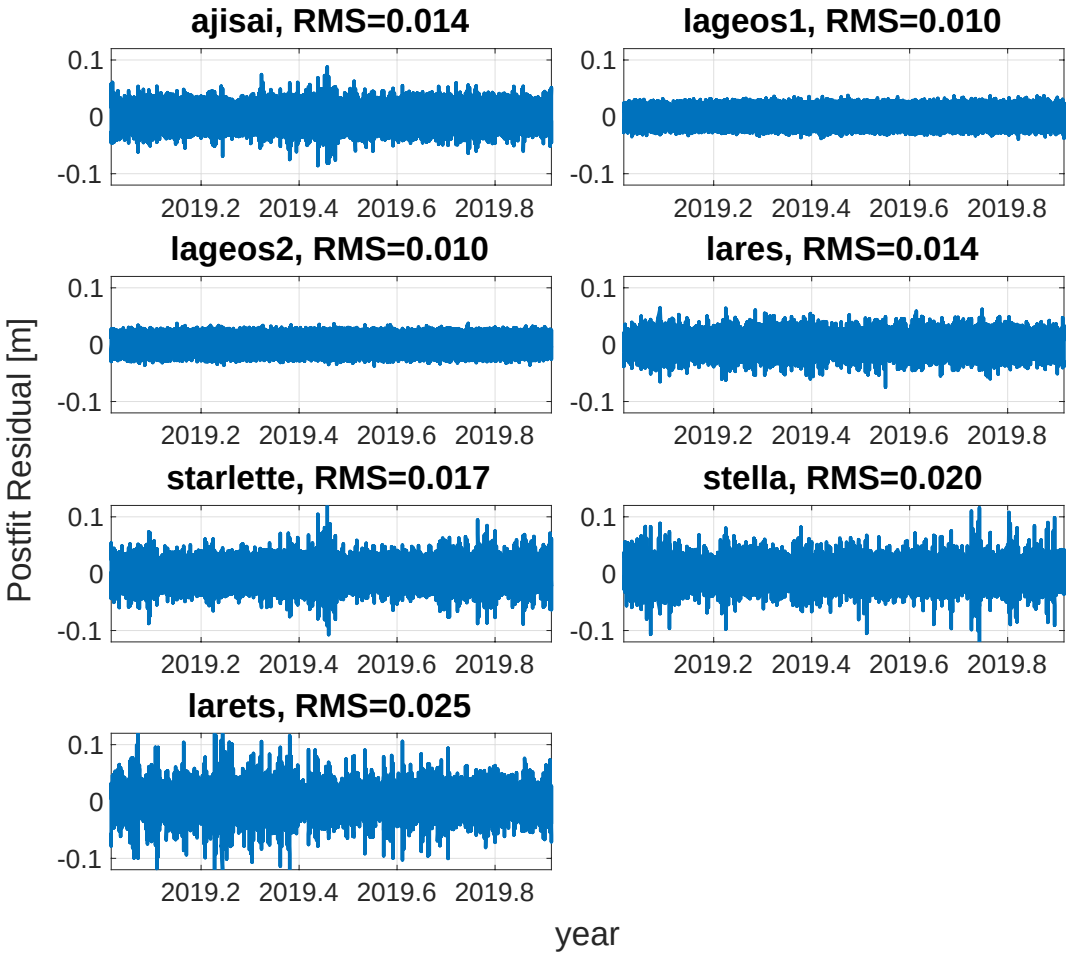

Figure 3.7: Timeseries of postfit range residuals for SLR7.

Chapter 4

New SLR Satellite

4.1 Overview

This chapter presents results from analysis of a potential new SLR satellite designed to improve independent SLR TVG solutions. First, the orbital parameters are discussed and a reasonably sized search space is outlined. Following a suite of simulations that investigates various altitudes and inclinations of an new SLR satellite, it will be shown through numerous performance metrics that the addition of a low inclination satellite most benefits SLR gravity solutions. Finally, a sensitivity analysis and analytical perturbation techniques are applied to support the results and provide a mechanism for the observed improvements.

4.2 Orbital Parameters

A grid-like search is adopted to investigate the orbit of a new SLR satellite. One could try to approach the problem from an optimization standpoint, but the varying goals of SLR means that strict optimization may overlook solutions of interest. To consider all six Keplerian orbital elements is, from a computational perspective, prohibitively expensive and impractical. As discussed in Section 1.5, existing studies have recognized altitude and inclination as the most consequential orbit parameters for determining TVG from SLR. Eccentricity does play some role in sensitivity to the odd zonals, however LARES has substantially improved these coefficients and the search space rapidly expands if e and ω are considered. Furthermore, several sources can induce eccentricity variations, and these can be difficult to disentangle as discussed more in Section 4.5. This work

will therefore assume only circular orbits.

The altitude of a satellite naturally influences its sensitivity to the gravity field as seen explicitly in Eq. 2.5. For dedicated satellite gravity missions, such as GOCE and GRACE, it is often desired to fly the satellite as low as operationally possible. Low altitudes, however, present challenges from increased atmospheric drag, increased orbital maintenance requirements, and shorter mission durations. A different set of considerations arises when it comes to selecting the altitude of SLR satellites:

(1) They are passive, making them unable to alter their trajectory once in orbit.

(2) They are primarily sensitive to low-degree gravity terms.

(3) Their shape and density helps with modeling and resilience to non-conservative perturbations.

(4) A lower altitude can decrease their observability from certain ground stations.

(5) Different geodetic objectives (gravity, frame dragging, reference frame) may benefit from different orbits.

Figure 4.1 shows the attenuation with altitude of the gravitational potential versus spatial wavelength and corresponding spherical harmonic degrees. For GRACE-like missions that desire a high spatial resolution, the benefit of a lower altitude is obvious from this figure as the gravitational signature of small-scale features decays rapidly with increasing altitude. Conversely, SLR satellites can only independently recover up to a maximum degree of about 6. Comparing a satellite at 500 km and 1400 km, one finds the influence of degree 6 attenuated by a factor of ~ 2. This difference increases to a factor of ~ 20 for a satellite at 5000 km compared to one at 500 km.

Based on this analysis, this work will not consider altitude a primary parameter of interest, although it is still investigated. The simulated new satellite will be confined to the LEO regime such that varying the altitude by a couple hundred kilometers does not largely affect the satellite's formal sensitivity to low-degree gravity. Section 4.5 further supports this choice. In fact, it would

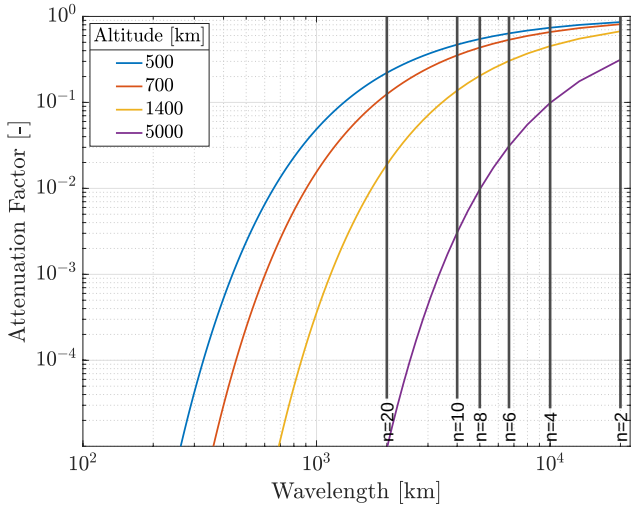

Figure 4.1: Attenuation of gravitational potential as a function spatial wavelength for select satellite altitudes. Black lines show corresponding spherical harmonics of degree n.

be unwise to select the altitude strictly from Figure 4.1 because of factors (1) and (4) listed at the start of this section. Though it remains under-studied, the importance of inclination has been recognized for many years; Kaula [1966] notes this point on several occasions, for example:

> "The ideal method of removing ill-conditioning is to include data from orbits of several different inclinations." (p. 112)

> "The set of satellite orbits used [in determining the even zonals] should have a variety of inclinations sufficient to separate the different harmonics." (p. 116)

With this in mind, a novel simulation and analysis is performed where the inclination of a potential new SLR satellite is varied in 5° steps from 10° to 170°. Inclinations nearer to equatorial ones are not considered as the satellite would have extremely limited visibility from the ground with a LEO altitude. At the investigated inclinations, the number of observations to the satellite will be examined to confirm reasonable visibility in Section 4.4.

4.3 Numerical Simulation Results

Chapter 3 discussed the numerical simulation procedure. The SLR7 and 33 new SLR satellites placed at varied inclinations are simulated according to the presented methods. The new satellite is given an area-to-mass ratio and relative weight equal to that of LARES. The altitude is selected at 1440 km, except where noted. After generating partials, gravity solutions are formed for the SLR7 and SLR7+New, where "new" refers to the addition of a single new satellite. The simulation is run over a minimum of 12 months, though many of the following results are based on an extended 5-year timeseries.

4.3.1 Correlations

A well-established characteristic and limitation of SLR-only gravity estimates is that certain parameters display high formal correlations, denoted by ρ [Sośnica et al., 2015; Cheng and Ries, 2017; Loomis et al., 2020]. This is apparent in several low-order terms of the same degree parity, such as $C_{2,0}/C_{4,0}$ and $C_{3,0}/C_{5,0}$. Figure 4.2 displays the correlation matrix for the baseline SLR7.

In this case, the estimated zonals are correlated such that $\rho_{C_{2,0}}^{C_{4,0}} = -0.58$ and $\rho_{C_{3,0}}^{C_{5,0}} = -0.85$, which agrees with results from processing real data [Loomis et al., 2020; Sośnica et al., 2015]. Estimating $C_{6,0}$ increases the magnitude of $\rho_{C_{2,0}}^{C_{4,0}}$ by about 50%, hence its exclusion from the state space [Loomis et al., 2019]. Likewise, the even order one terms are correlated with $|\rho| \geq 0.8$, for example $\rho_{S_{2,1}}^{S_{6,1}} = 0.85$. Other coefficients of a given order and degree parity are slightly to moderately correlated ($0.1 < \rho < 0.5$). These correlations do not necessarily imply a low-quality solution, but they do indicate that these parameters are not fully separated.

Ideally, a new satellite would reduce the parameter correlations, especially given SLR's role in supporting GRACE through estimates of $C_{2,0}$ and $C_{3,0}$. Figures 4.3 and 4.4 show the correlation coefficients of the zonals and even-degree order 1 terms, respectively, for all SLR7+New solutions as well as the SLR7 for reference. In both cases there is little distinction between the results with a new satellite in a prograde orbit versus its retrograde counterpart. For the zonals, it is immediately clear that the only significant reduction in the correlations occurs with a new satellite inclined at less than about 50°. The impact of a low-inclination satellite is striking, with $\rho_{\text{slr7}}^{C_{2,0}/C_{4,0}} = -0.58$ reduced by nearly an order of magnitude to $\rho_{\text{slr7+30°}}^{C_{2,0}/C_{4,0}} = -0.07$. Even with a new satellite inclined at 45°, the baseline correlation is reduced by half. A new satellite does not affect the odd zonals as dramatically, but still mitigates the correlation. With a new satellite at 25° or 30°, $|\rho_{C_{3,0}}^{C_{5,0}}| = 0.3$, which is a significant reduction from the near-perfect correlation seen with the SLR7. The impact of a low-inclination satellite further shows in the reduction in correlations of the even-degree order 1 terms. Figure 4.4 shows that both the C and S terms are about equally affected, with the smallest correlations occurring with a new satellite inclined around 30°. For the 2,1/4,1 terms (both C and S) a low-inclination satellite reduces the baseline $|\rho_{\text{slr7}}^{2,1/4,1}| = 0.85$ by 2 orders of magnitude to $|\rho_{\text{slr7+30°}}^{2,1/4,1}| = 0.005$. The correlation between $C_{2,1}$ and $C_{6,1}$ is reduced by up to a factor of 10 with the low-inclination satellite, although the S coefficients are less impacted as they are reduced up to a factor of 3. The degree 4 and 6 order 1 terms also show a near total decorrelation for certain cases with $|\rho_{\text{slr7+25°}}^{2,1/4,1}| = 0.04$ and $|\rho_{\text{slr7+30°}}^{2,1/4,1}| \approx 0.10$.

No reviewed literature has suggested or investigated a low-inclination satellite for improving

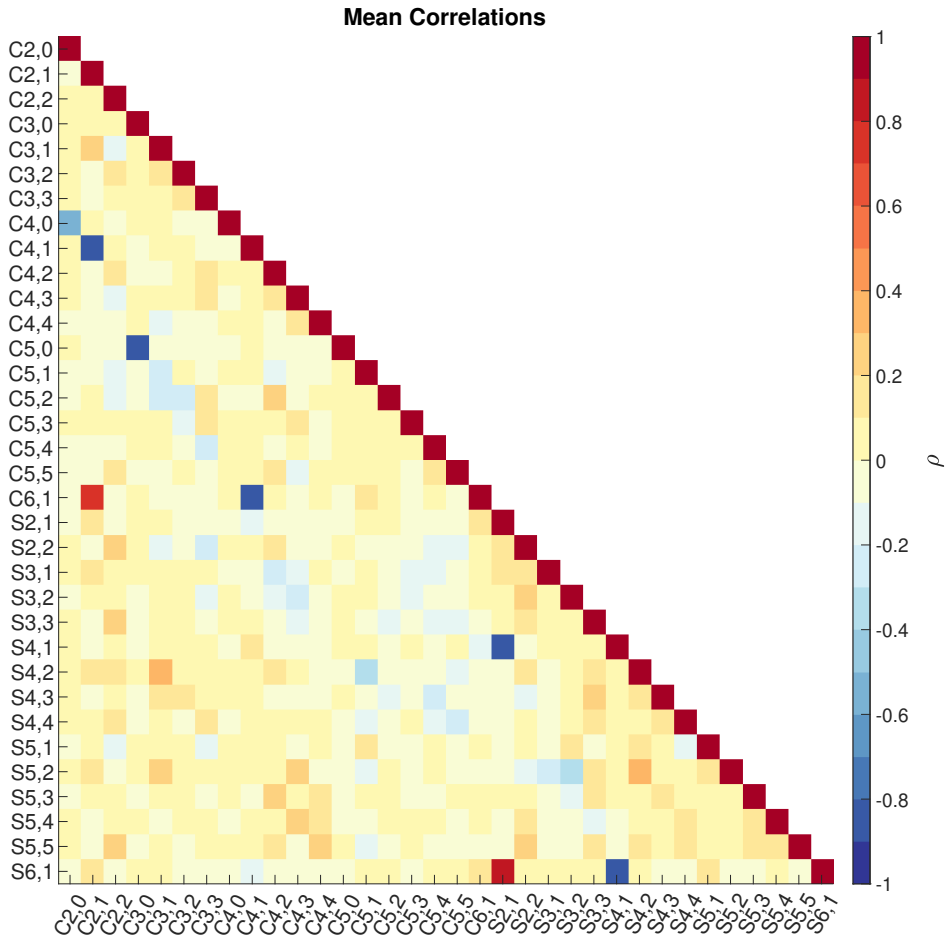

Figure 4.2: Mean correlation matrix for estimated gravity parameters from the SLR7.

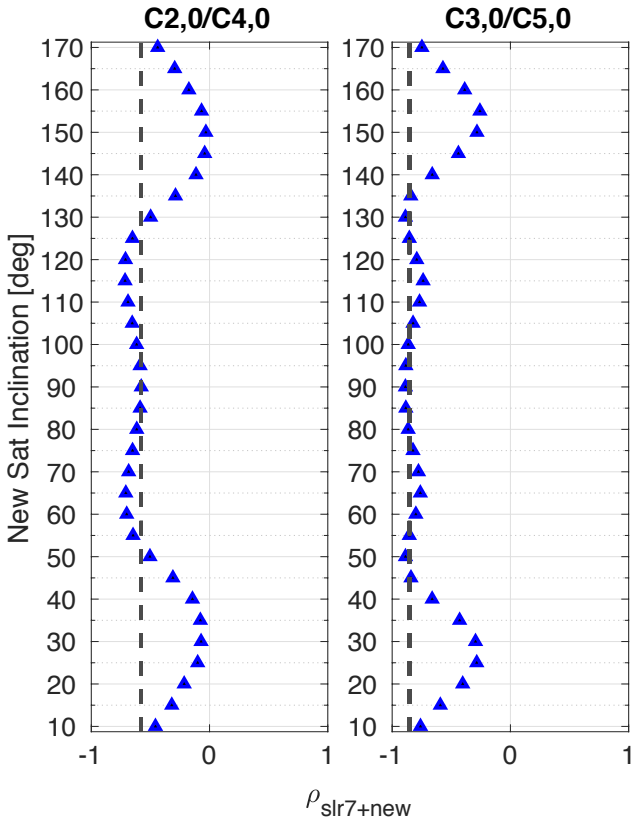

Figure 4.3: Correlation coefficients for estimated zonals for SLR7 (black dash) and SLR7+New (blue triangle), where the new satellite is at the indicated inclination.

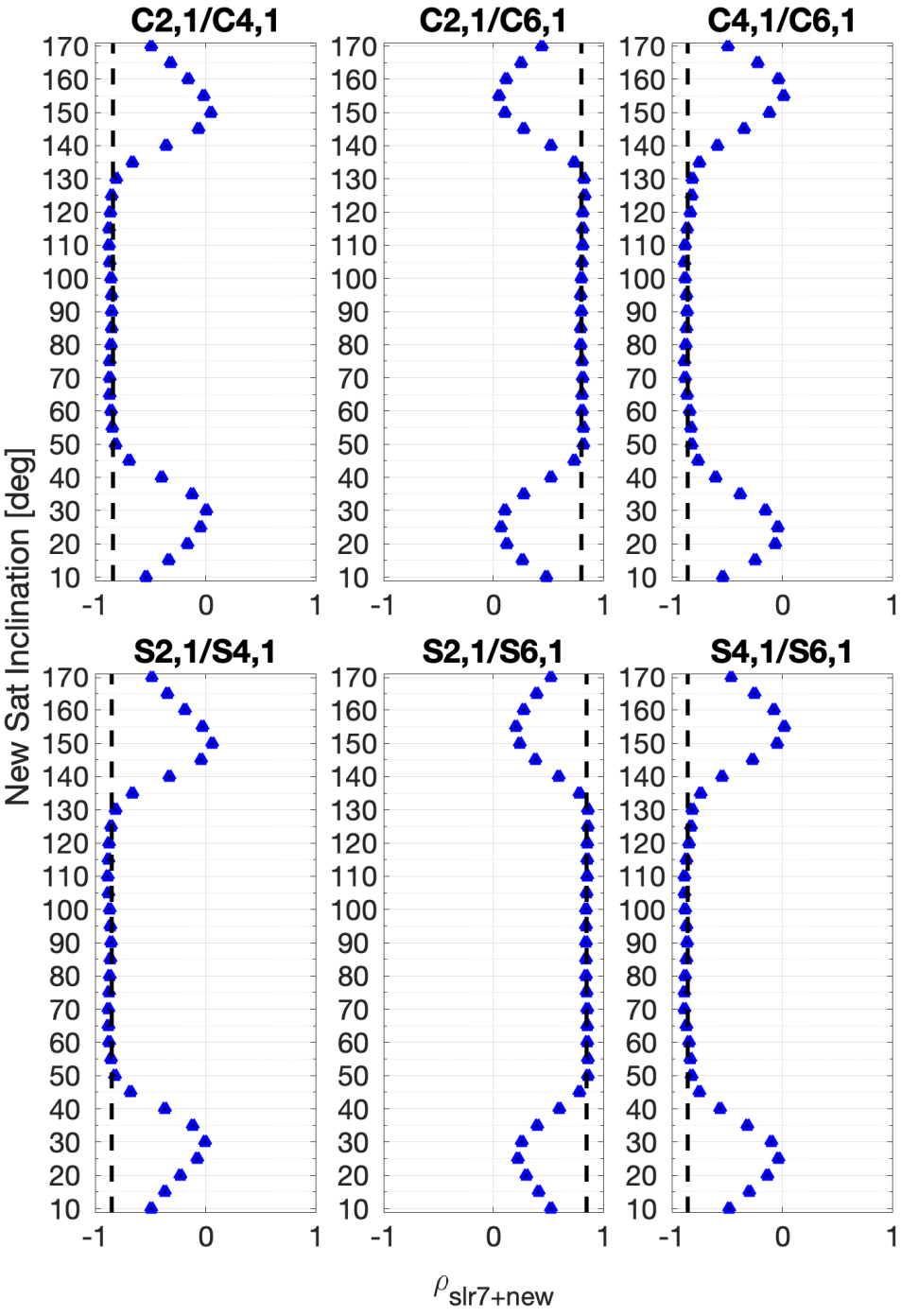

Figure 4.4: Correlation coefficients for estimated even-degree order 1 terms for SLR7 (black dash) and SLR7+New (blue triangle), where the new satellite is at the indicated inclination.

SLR TVG solutions. Some have remarked on the utility of Beacon-C for the zonal coefficients, but it is not a desirable ranging target and its contribution is necessarily downweighted in solutions that include it [Cheng and Ries, 2023]. The idea of a new SLR satellite inclined at $\sim 30^\circ$ is novel, and its contribution to reducing major correlations would be significant as the preceding analysis demonstrates. However, parameter correlations represent only one aspect of SLR gravity solutions. Additional analyses will support more conclusive results.

4.3.2 Recovery of Coefficients

The correlation coefficients provide a metric for solution quality, but they do not depend on the actual data (Eqs. 2.38 and 2.39). The preceding analysis suggests a low-inclination satellite as the most beneficial addition to the SLR7. Here, the simulation environment is leveraged to investigate the quality of the recovered coefficients, as this typically represents the final product for SLR-derived gravity solutions.

Figure 4.5 shows a 62-month timeseries of the zonal coefficients for the truth, SLR7, and two SLR7+New estimates. For the SLR7, the effect of the correlated parameters clearly manifests in the estimates of the even zonals. The amplitude error seen in $C_{2,0}$ is also seen in $C_{4,0}$ as the baseline solution cannot rigorously separate the two coefficients, although $C_{2,0}$ has a larger magnitude and is recovered better. As one would expect with LARES in the solution, the SLR7 recover the odd zonals reasonably well (cf. Figure 1.4), though inspection of Figure 4.5 reveals some errors. Two cases are compared for the new satellite: one inclined at 30° and 90°. Based on the correlation analysis, one would expect the former to improve the solution, while the latter would have a minimal impact. Indeed, the new satellite at 30° has a significant effect on recovering the even zonals. The formal decorrelation of the even zonals clearly leads to a large improvement in the estimated values. Conversely, the addition of a new polar SLR satellite adds little information and its inclusion effectively leaves the estimated zonals unchanged.

Table 4.1 quantifies several of these changes in terms of the annual and semi-annual amplitudes derived from least squares fits. The *truth* value of $C_{2,0}$ has an annual amplitude of

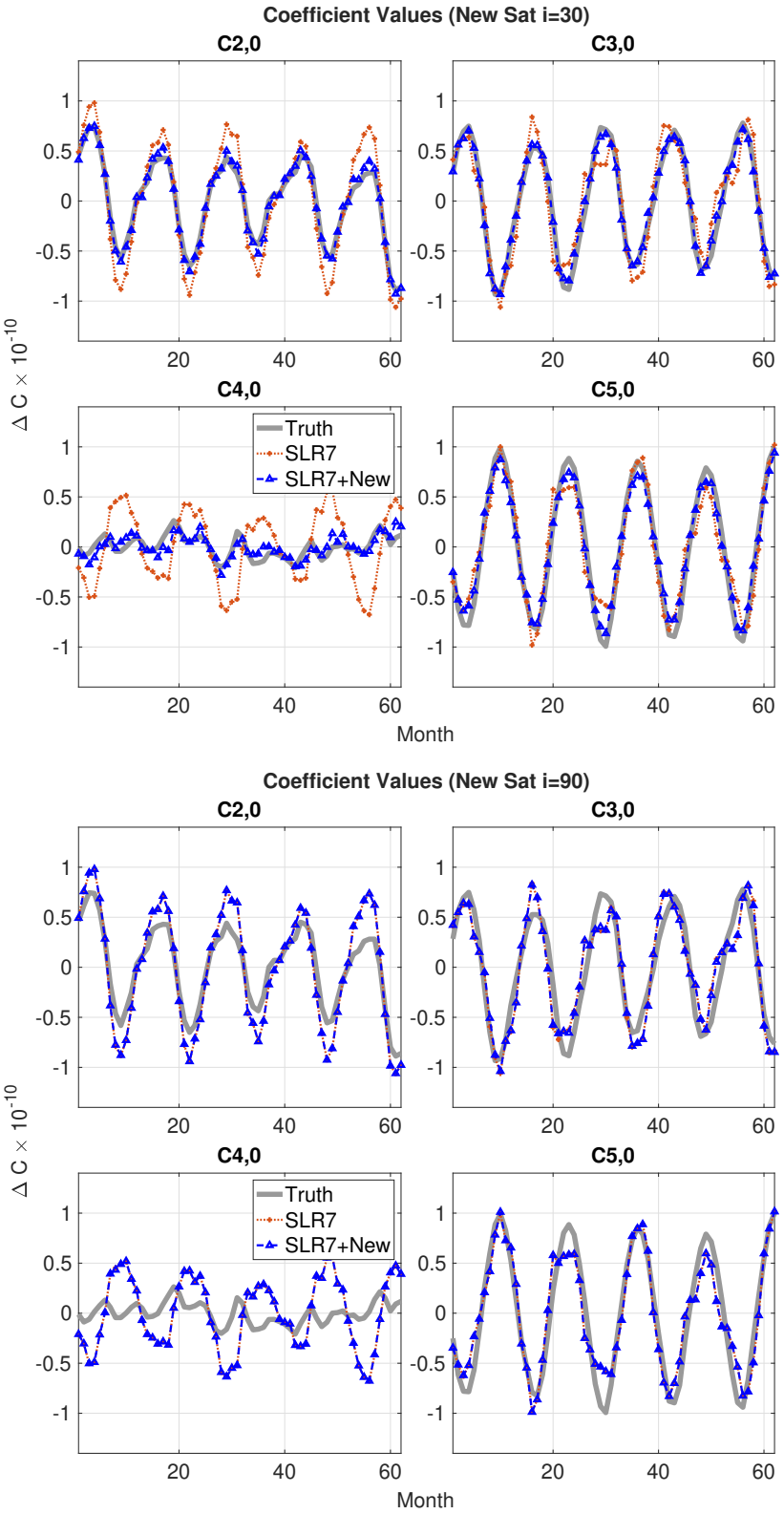

Figure 4.5: Zonal coefficients for truth (grey), SLR7 (red), and SLR7+New (blue), where the new satellite is inclined at 30° (top) and 90° (bottom).

4.945×10^{-11} and the SLR7 estimate this at a value of 7.626×10^{-11}. With the addition of a new SLR satellite, the smallest $C_{2,0}$ amplitude errors are seen with satellites between 15° and 40° (prograde and retrograde), with the impact quickly becoming less significant for higher inclinations. The same pattern holds true for the $C_{2,0}$ semi-annual amplitudes, though the magnitude of this *truth* signal is $\sim 75\%$ smaller than the annual one. The annual signal in $C_{4,0}$ is nearly an order of magnitude smaller than $C_{2,0}$. In cases where the correlation between even zonals stays high (cf. Figure 4.3), the error in the estimated $C_{4,0}$ amplitude remains unsurprisingly large. The "best" estimates of $C_{4,0}$ are seen for a new satellite inclined between and including 20° and 30° when considering the signal-to-noise ratio. The odd zonals $C_{3,0}$ and $C_{5,0}$ have larger annual amplitudes at 7.445×10^{-11} and 8.840×10^{-11}, respectively. Given the presence of LARES in the solution, the SLR7 recover these values better with errors of 0.430×10^{-11} and 1.364×10^{-11}, respectively. The addition of a 25° or 30° reduces the $C_{3,0}/C_{5,0}$ correlation, leading to modest improvements in the recovered annual amplitudes. Furthermore, the amplitude estimates improve slightly with a 75° or 80° satellite. Considering that these are near LARES's inclination (70°), which has been identified as an important factor in its influence, additional observations in this band ought to improve the solution further. In all cases, however, the errors are quite small when considering their magnitude relative to the *truth* signal.

To first order, reducing the correlations between certain coefficients has had a demonstrable impact on the independent SLR gravity solution. However, the behavior of the odd zonals reiterates that the formal correlations comprise only one aspect of the solution. The odd zonals are recovered fairly well despite their strong nominal correlation. As Loomis et al. [2020] point out, LARES's unique physical properties increase its resilience to non-conservative forces and reduce the mapping of data errors into the solution [see also Menke, 2015]. It is therefore necessary to examine multiple metrics when assessing the quality of SLR TVG solutions. The numerical simulation environment provides a useful and configurable method for such analyses.

Another commonly used performance indicator is the root-mean-square (RMS) of the difference between two solutions. Figures 4.6 and 4.7 report the relative improvement in the error RMS

Table 4.1: Truth and estimated zonal amplitudes. For the estimates, the reported value is the error (Truth–Estimate).

Case	**Annual** $\times 10^{-11}$				**Semi-Annual** $\times 10^{-11}$			
	$C_{2,0}$	$C_{3,0}$	$C_{4,0}{}^a$	$C_{5,0}$	$C_{2,0}$	$C_{3,0}$	$C_{4,0}{}^a$	$C_{5,0}$
Truth	4.945	7.445	0.571	8.840	1.379	0.948	0.834	0.306
Estimates (errors)								
SLR7	-2.681	0.430	-4.139	1.364	-0.475	-0.088	0.183	0.136
SLR7+10	-1.556	-1.268	-2.078	-0.264	-0.052	0.454	0.040	-0.217
SLR7+15	-0.617	-1.919	-0.548	-0.905	0.157	0.321	-0.173	-0.092
SLR7+20	-0.233	-1.292	-0.025	-0.332	0.161	0.080	-0.069	0.145
SLR7+25	-0.135	-0.411	0.219	0.483	0.098	0.009	0.140	0.214
SLR7+30	-0.427	0.402	-0.385	1.237	0.019	-0.123	0.343	0.098
SLR7+35	-0.847	1.068	-1.292	1.822	-0.049	-0.083	0.505	0.072
SLR7+40	-1.345	1.510	-2.282	2.153	-0.097	-0.119	0.538	0.064
SLR7+45	-2.026	1.117	-3.383	1.756	-0.274	-0.116	0.423	0.256
SLR7+50	-2.585	0.476	-4.060	1.321	-0.470	-0.103	0.216	0.094
SLR7+55	-2.920	0.514	-4.150	1.514	-0.577	-0.155	0.186	0.217
SLR7+60	-2.867	0.475	-3.894	1.445	-0.601	-0.282	0.291	0.115
SLR7+65	-2.731	0.380	-3.842	1.317	-0.500	0.004	0.220	0.140
SLR7+70	-2.672	0.585	-4.102	1.526	-0.463	0.096	0.215	0.094
SLR7+75	-2.668	-0.065	-3.945	1.043	-0.478	-0.145	0.273	0.134
SLR7+80	-2.698	-0.167	-4.199	1.100	-0.489	-0.112	0.243	0.132
SLR7+85	-2.718	0.533	-4.494	1.371	-0.456	-0.106	0.354	0.118
SLR7+90	-2.668	0.473	-4.128	1.370	-0.458	0.030	0.196	0.145
SLR7+95	-2.628	0.412	-3.819	1.359	-0.491	-0.060	0.014	0.133
SLR7+100	-2.646	-0.086	-3.794	1.143	-0.489	-0.048	0.053	0.057
SLR7+105	-2.704	0.122	-4.375	1.228	-0.475	-0.162	0.186	0.230
SLR7+110	-2.683	0.770	-4.144	1.683	-0.457	-0.035	0.099	-0.069
SLR7+115	-2.742	0.683	-3.877	1.621	-0.482	-0.595	0.234	-0.232
SLR7+120	-2.916	0.531	-3.842	1.511	-0.570	-0.567	0.299	-0.219
SLR7+125	-2.931	0.406	-4.149	1.374	-0.604	-0.084	0.198	0.157
SLR7+130	-2.644	0.481	-4.104	1.315	-0.354	-0.120	0.245	0.099
SLR7+135	-1.987	1.056	-3.333	1.721	-0.181	-0.169	0.527	0.150
SLR7+140	-1.321	1.447	-2.244	2.099	-0.150	-0.027	0.653	0.041
SLR7+145	-0.819	1.133	-1.238	1.868	-0.074	-0.102	0.548	0.211
SLR7+150	-0.338	0.486	-0.226	1.301	0.048	-0.124	0.299	0.224
SLR7+155	-0.061	-0.345	0.346	0.537	0.151	-0.070	0.061	0.286
SLR7+160	-0.128	-1.326	0.071	-0.362	0.194	0.071	-0.112	0.166
SLR7+165	-0.483	-1.974	-0.401	-0.954	0.186	0.109	-0.233	0.118
SLR7+170	-1.406	-1.340	-1.833	-0.340	-0.011	0.497	0.040	-0.227

[a] $C_{4,0}$ fits are not statistically significant, but are reported for completeness.

between the SLR7 and SLR7+New expressed as a percent,

$$\%\text{Improvement} = \left(1 - \frac{\text{RMS}_{\text{slr7+new}}}{\text{RMS}_{\text{slr7}}}\right) \times 100 \tag{4.1}$$

where $\text{RMS}_i = \text{RMS}(\text{Truth} - \text{Est}_i)$ and i refers to a particular estimate. For example, if the baseline RMS equals 1 and the new RMS equals 0.9, then by Eq. 4.1 the improvement is 10% (i.e. the new error RMS is relatively closer to 0). Of course, the ability to compute this metric with respect to the known truth is unique to the simulation environment and it gives a raw indicator of how a new satellite can affect individual terms.

Inspecting the improvements to the zonal terms in Figure 4.6, the largest changes continue to come from the addition of a low-inclination satellite, most notably for the even zonals. For $C_{2,0}$ and $C_{4,0}$, a new satellite inclined between 10° and 45° reduces the RMS of the errors in these coefficients, with the maximum improvements of nearly 80% seen with inclinations of 25° or 30°. This follows logically from the previous discussions regarding the correlations and seasonal fits as the low-inclination satellite clearly benefits the solution's sensitivity to the even zonals. The odd zonals display a somewhat similar pattern, although the low-inclination improvement band is less pronounced than with the even zonals. Error reductions of $\sim 70\%$ are seen with the same low-inclination satellites as with the even zonals. In discussing Table 4.1 it was noted that adding a satellite near LARES's inclination slightly improved the estimated amplitudes. Figure 4.6 also shows this in terms of the errors, but the improvements in these mid-inclinations are quite minimal. Recall that the baseline SLR7 error in the odd zonals is comparatively small and the improvements of $10 - 20\%$ are less significant in an absolute sense. Still, the improved recovery with the low-inclination satellites is encouraging.

The $C_{2,1}/S_{2,1}$ pair physically represent Earth's principal figure axis, and their analysis quickly becomes complex in reality as numerous processes contribute to their variations (e.g., solid Earth, tides) [Cheng et al., 2011]. In processing SLR data, the recovery of these coefficients may also depend on selected geophysical models and more rigorous analysis of these coefficients is left for future studies. Figure 4.7 does still show minor improvements in $C_{2,1}$ with a low-inclination satellite,

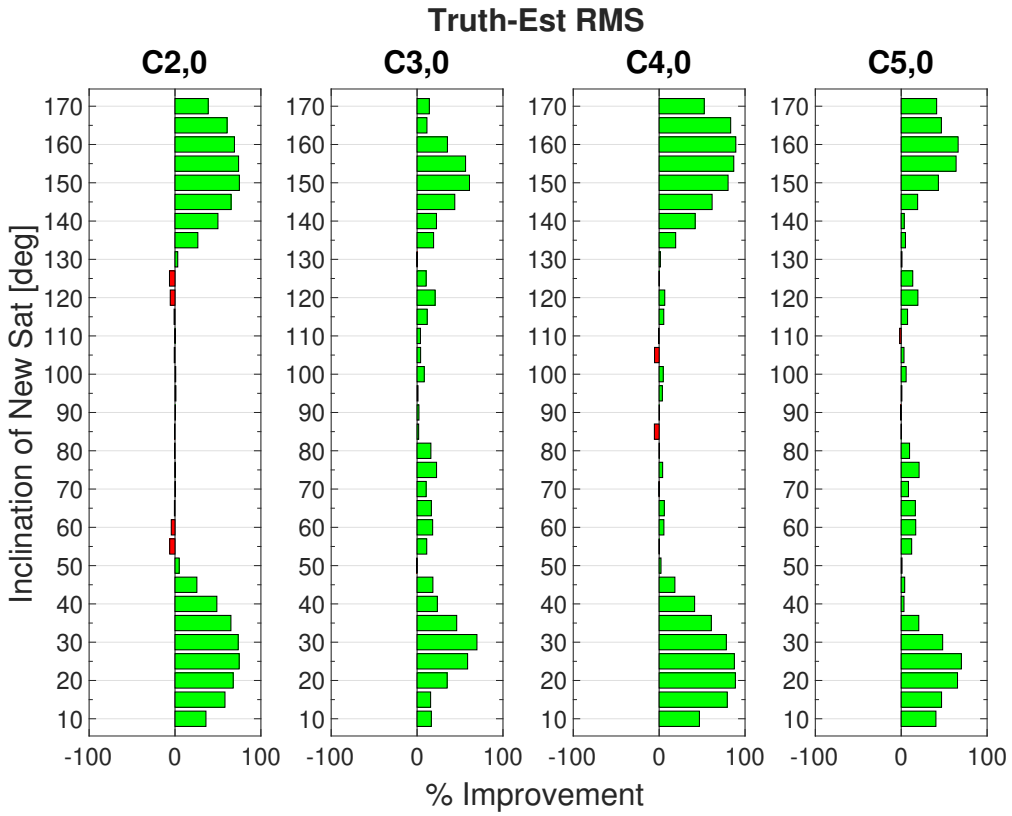

Figure 4.6: Relative improvement in error RMS of estimated zonals with a new satellite at varied inclinations.

but virtually no change in $S_{2,1}$, possibly due to the fact that it is not fully separated from $S_{6,1}$ (Figure 4.4). The odd-degree order 1 terms show small changes that lack significance compared to the overall estimate. The $C_{4,1}$, $C_{6,1}$, and $S_{6,1}$ improve more systematically with a satellite at or below 30° reducing the RMS by up to about 50%, while $S_{4,1}$ shows comparatively modest improvements at these inclinations. These coefficients more strongly decorrelate with the low-inclination satellite, which could explain the RMS behavior. Figure 4.8 displays the timeseries of the truth and estimates (SLR7 and SLR7+30°) for these coefficients to show how their magnitude is influenced. While the SLR7 captures the general signal in these coefficients, there is a notable benefit with the added sensitivity of the 30° satellite.

4.3.3 Higher Degree Influences

Thus far there has been much discussion around changes in the correlations and coefficient estimates both in an absolute and in a relative sense. The correlations between coefficients do not necessarily preclude a quality solution, but their presence does indicate that certain coefficients are not fully separated. Furthermore, non-estimated higher degree terms will influence the estimated lower degree terms. For example, variations in $C_{6,0}$ will influence $C_{2,0}$ and $C_{4,0}$, but the estimation of $C_{6,0}$ dramatically increases $\rho_{C_{2,0}}^{C_{4,0}}$ and the solution becomes unreliable [Cheng and Ries, 2017; Loomis et al., 2019]. Cheng et al. [1997] describe one technique to quantify these higher degree influences by defining $x = \hat{x} + S\bar{c}$, where x is the estimated coefficient vector that includes higher degree errors, $\hat{x}$ is the $n \times 1$ current estimate vector, $\bar{c}$ is the $u \times 1$ *a priori* vector of the unestimated parameters, and the $n \times u$ sensitivity matrix S is given as,

$$S = -P_x H_x^T R^{-1} H_c \tag{4.2}$$

where P_x is the solution covariance matrix, H_x is the partials for the estimated parameters, R is the observation error covariance matrix, and H_c is the partials of the unestimated parameters. Note that this is essentially the sensitivity matrix that arises out of consider covariance analysis [see Tapley et al., 2004a, Eq. 6.4.4]. Observe that S_{ij} quantifies the influence of unestimated parameter

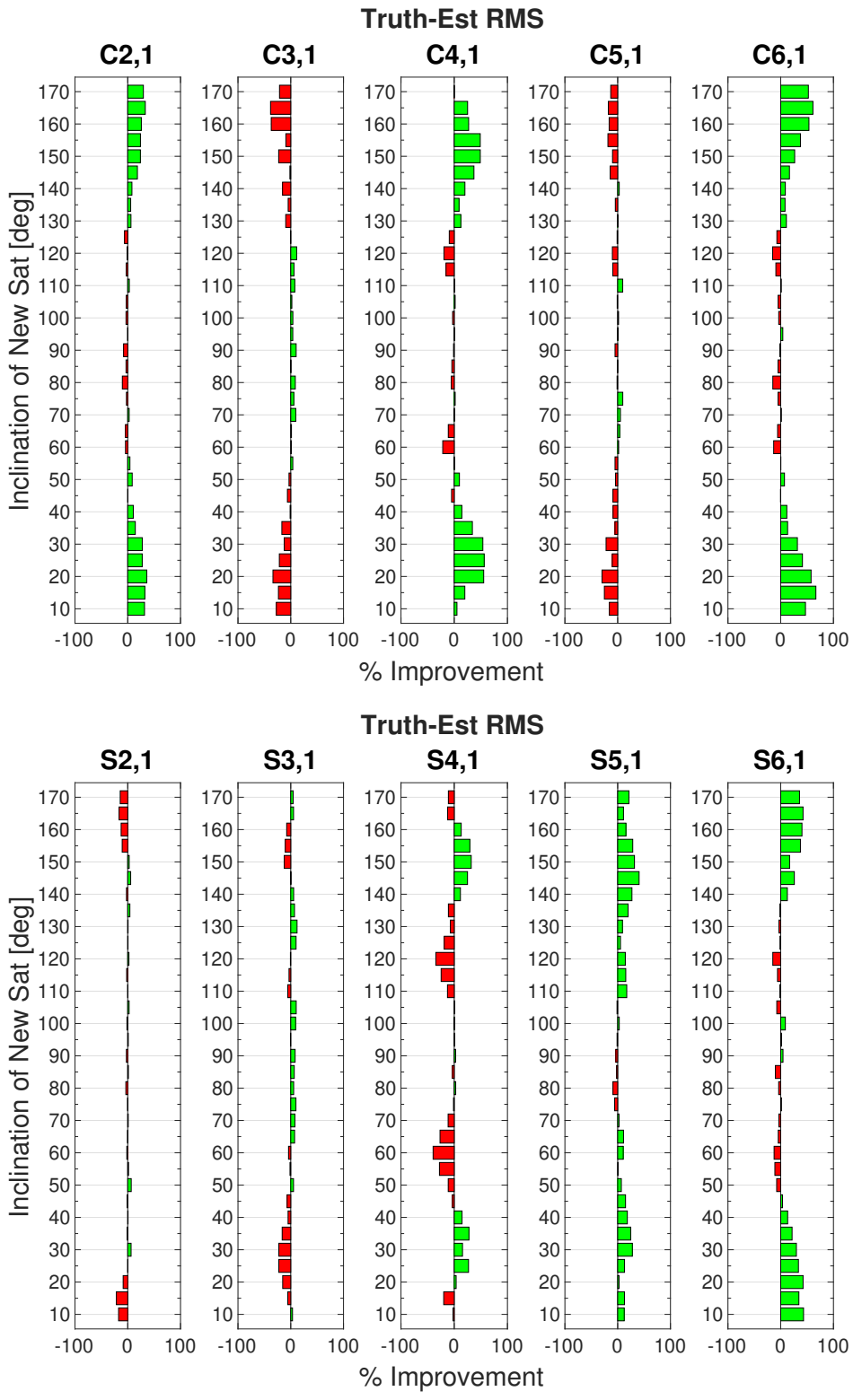

Figure 4.7: Relative improvement in error RMS of estimated order 1 coefficients with a new satellite at varied inclinations.

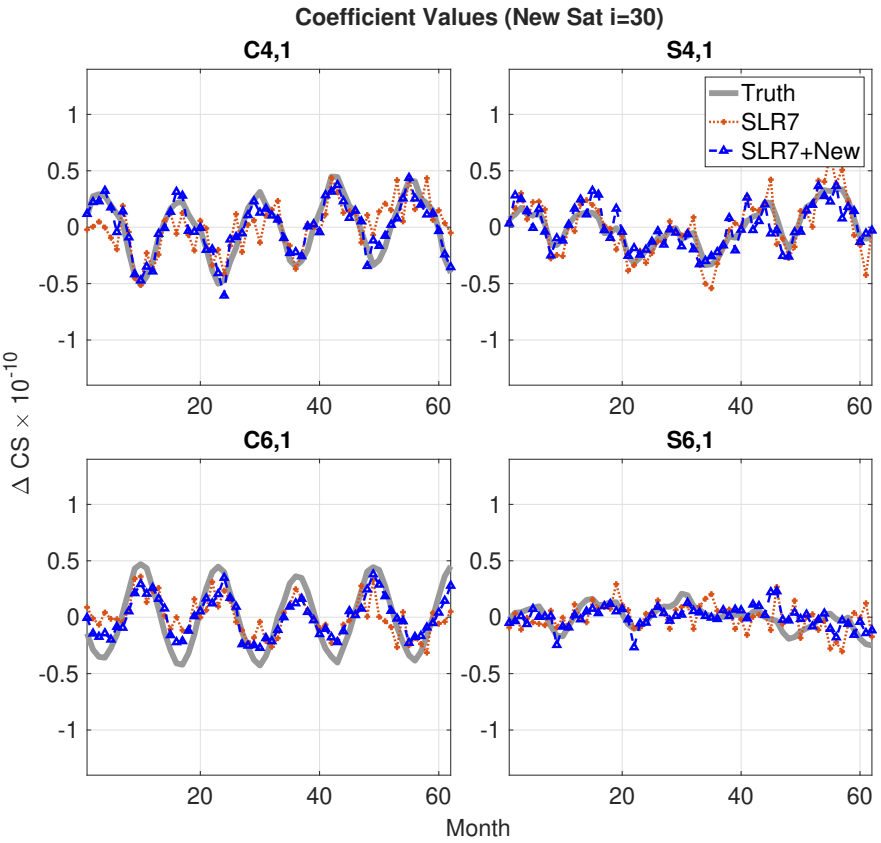

Figure 4.8: Truth and estimated order 1 coefficients for degrees 4 and 6. The new satellite is inclined at 30°.

c_j on estimated parameter $\hat{x}_i$.

Figure 4.9 shows the magnitude of these sensitivity matrices for the SLR7 and SLR7+30°, where the unestimated set of parameters up to degree and order 10 are considered. Table 4.2 reports values from S for the zonal coefficients. This information reveals some of the interplay between correlations and solution quality. A larger value of S_{ij} means the particular unestimated parameter will have a larger influence on the particular estimated one. For the SLR7, the $C_{2,0}$ and $C_{4,0}$ estimate suffer strongly from the effects of higher degree even zonals. This is readily apparent when examining the impact of $C_{6,0}$, with $S^{\text{slr7}}_{C_{2,0}/C_{6,0}} = 6.31$ and $S^{\text{slr7}}_{C_{4,0}/C_{6,0}} = -9.50$ according to Table 4.2. Errors in $C_{8,0}$ influence $C_{4,0}$ more than twice as much as they do $C_{2,0}$, with $S^{\text{slr7}}_{C_{4,0}/C_{8,0}} = -5.54$. With the addition of the low-inclination 30° satellite, the separation of the estimated even zonals from the higher degree ones is rather remarkable. The sensitivity of both estimated even zonals to $C_{6,0}$ is reduced by over a factor of 3 in both cases such that $S^{\text{slr7+30}}_{C_{2,0}/C_{6,0}} = 1.87$ and $S^{\text{slr7+30}}_{C_{4,0}/C_{6,0}} = -2.30$. For $C_{8,0}$, the influence on $C_{2,0}$ becomes negligible and the influence on $C_{4,0}$ is reduced by a factor of 3.5. $C_{10,0}$ does not separate as well, but the impact of the low-inclination satellite still clearly benefits the zonals. In the baseline SLR7 solution, the odd zonals are better recovered than the even ones despite their correlation, as discussed previously. Overall, the unestimated odd zonals influence the estimated odd zonals less than the even degree ones. The maximum sensitivity is $S^{\text{slr7}}_{C_{3,0}/C_{9,0}} = 3.55$. Thus, in addition to LARES's favorable material properties that reduce the mapping of data errors, it also likely helps to separate the effects of higher degree coefficients. Given that S relates errors in the unestimated coefficients to the estimated ones, one should further consider the magnitude of the coefficients. $C_{4,0}$, for example, has a smaller signal than the other low-degree zonals and errors from higher degree terms may get amplified more noticeably.

4.3.4 Global Improvements

This chapter has so far focused mainly on a new SLR satellite's ability to improve the time-varying zonal estimates. After all, one of SLR's main purposes over the past 2 decades has been to provide estimates of the first two zonals to support GRACE. SST missions have a spatial resolution

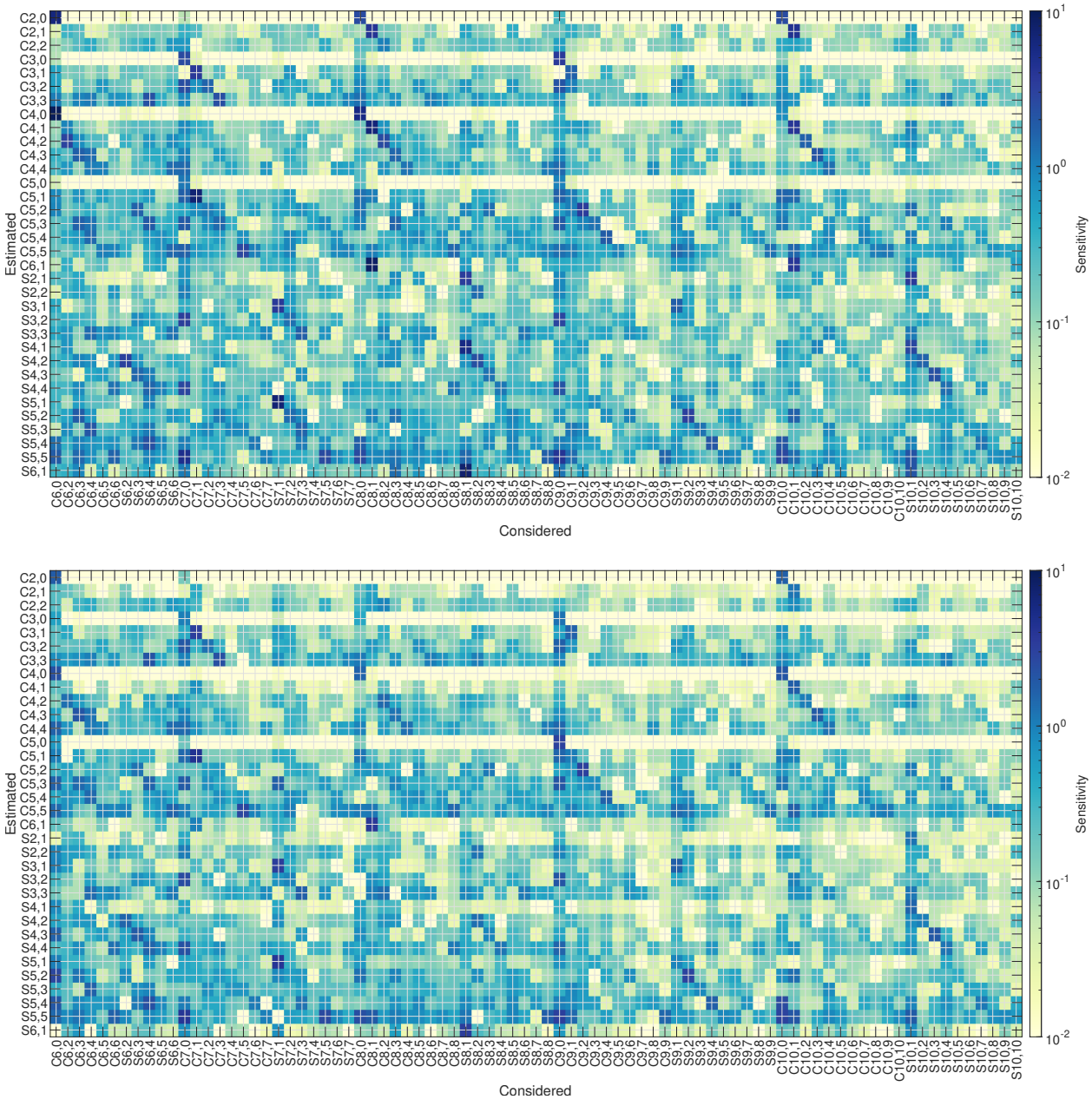

Figure 4.9: Magnitude of sensitivity matrices for SLR7 (top) and SLR7+30° (bottom).

Table 4.2: Sensitivity matrix values for zonal coefficients (see also Figure 4.9).

	$\mathbf{C_{2,0}}$		$\mathbf{C_{3,0}}$		$\mathbf{C_{4,0}}$		$\mathbf{C_{5,0}}$	
	S	SN	S	SN	S	SN	S	SN
$\mathbf{C_{6,0}}$	6.31	1.87	0.07	0.53	-9.50	-2.30	0.04	-0.62
$\mathbf{C_{7,0}}$	0.07	0.15	2.55	1.03	0.04	-0.01	-1.15	0.18
$\mathbf{C_{8,0}}$	2.46	<0.01	0.17	0.44	-5.54	-1.56	0.24	-0.14
$\mathbf{C_{9,0}}$	-0.30	<0.01	3.52	1.22	0.32	-0.03	0.97	2.98
$\mathbf{C_{10,0}}$	-2.52	-1.73	0.13	0.01	-0.79	-2.06	0.07	0.22

S=SLR7, SN=SLR7+30°

∼10x finer than SLR, which means that simulation studies of such missions can explore regional improvements [Wiese et al., 2011; Loomis et al., 2012]. These basin scale investigations are simply not possible at the spatial scale of SLR-only gravity solutions. At the global level, the spatial representation of a degree and order 5 solution will not appear physically meaningful, but it can characterize the solution as a whole. Other spectral methods, such as the degree variance, will provide further insight for the full SLR solution.

After fitting bias, trend, annual, and semi-annual terms to each coefficient (Table 4.1) the sine and cosine components of the annual part are synthesized in terms of cm EWH with Eq. 2.14. This metric has been used in previous SLR gravity studies [Nerem et al., 2000]. Figures 4.10 and 4.11 show the sine and cosine components, respectively, in terms of error with respect to the truth and computed to degree and order 5. For each figure, the results for the baseline SLR7 are shown in the top left and SLR7+New in each subsequent plot, where the inclination is as indicated. Note that only prograde results are shown due to the previously established symmetry. Also reported for each plot is the area-weighted RMS of the errors. Inspecting Figure 4.10, one sees the SLR7 has its largest error bands throughout the Southern hemisphere and near the equator. The largest reduction in the errors occurs with the addition of a satellite inclined below 40° and especially for the 20-30° cases. It is seen that these satellites reduce the RMS of the error in the sine component by up to 39%. Smaller improvements of ∼10% are made with the addition of a satellite at 40° or 45°. The remaining satellites have little impact on the solution, likely due to the fact that the

SLR7 already contain satellites near these orbits. The errors in the cosine component are overall smaller for the SLR7 (Figure 4.11). Modest improvements in the RMSE of 15% are seen with the previously discussed low-inclination set. The 60°, 65°, and polar case make a similar, though slightly reduced, contribution. The spatial pattern of the errors for these 3 cases differs from the low-inclination set, indicating that the mid to high inclination satellites make small improvements to different coefficients in the solution. Generally, the patterns observed here follow the previous sections with respect the the low-inclination satellites providing the most benefit to the solution. Diminishing improvements occur with too low of an inclination (i.e. below 20°), likely due to visibility issues described in 4.4.

When quantifying improvements to individual coefficients, the RMS was computed between the estimate and the truth. This technique can be extended to provide insight for the full solution. First, maps of the full solution in terms of equivalent water height are formed for the truth and estimated cases. These maps are then differenced and the area-weighted RMS is computed. This resembles the RMS discussed in terms of the annual fits, but now the actual solutions are investigated. Figure 4.12 shows the median of this value over the full timeseries for the SLR7 and SLR7+New cases. While this metric is compact and useful for this study, it should be noted that it can vary month-to-month and must be considered along with the other performance indicators. For the SLR7, the RMS is 1.30 cm EWH and the addition of the 30° satellite maximally reduces this by 10% to 1.17 cm EWH. Inclinations between 60° and 95° show varying levels of moderate improvements. Near 50° no improvements are observed because Starlette, AJISAI, and LAGEOS-2 already cover this orbit. Thus, these results support the addition of a low-inclination satellite for improving the full solution. By reducing these errors and increasing the separation of the estimated coefficients, new gap-filling methods may become feasible if another gap between GRACE missions occurs [Bonin et al., 2018].

Perhaps the most prolific quantity in gravity field analysis is the degree variance or amplitude, which assesses spectrally the power of the gravity field degree-wise (or order-wise). Figure 4.13 presents these values for the SLR7 as well as 3 cases of SLR7+New: a low, mid, and polar

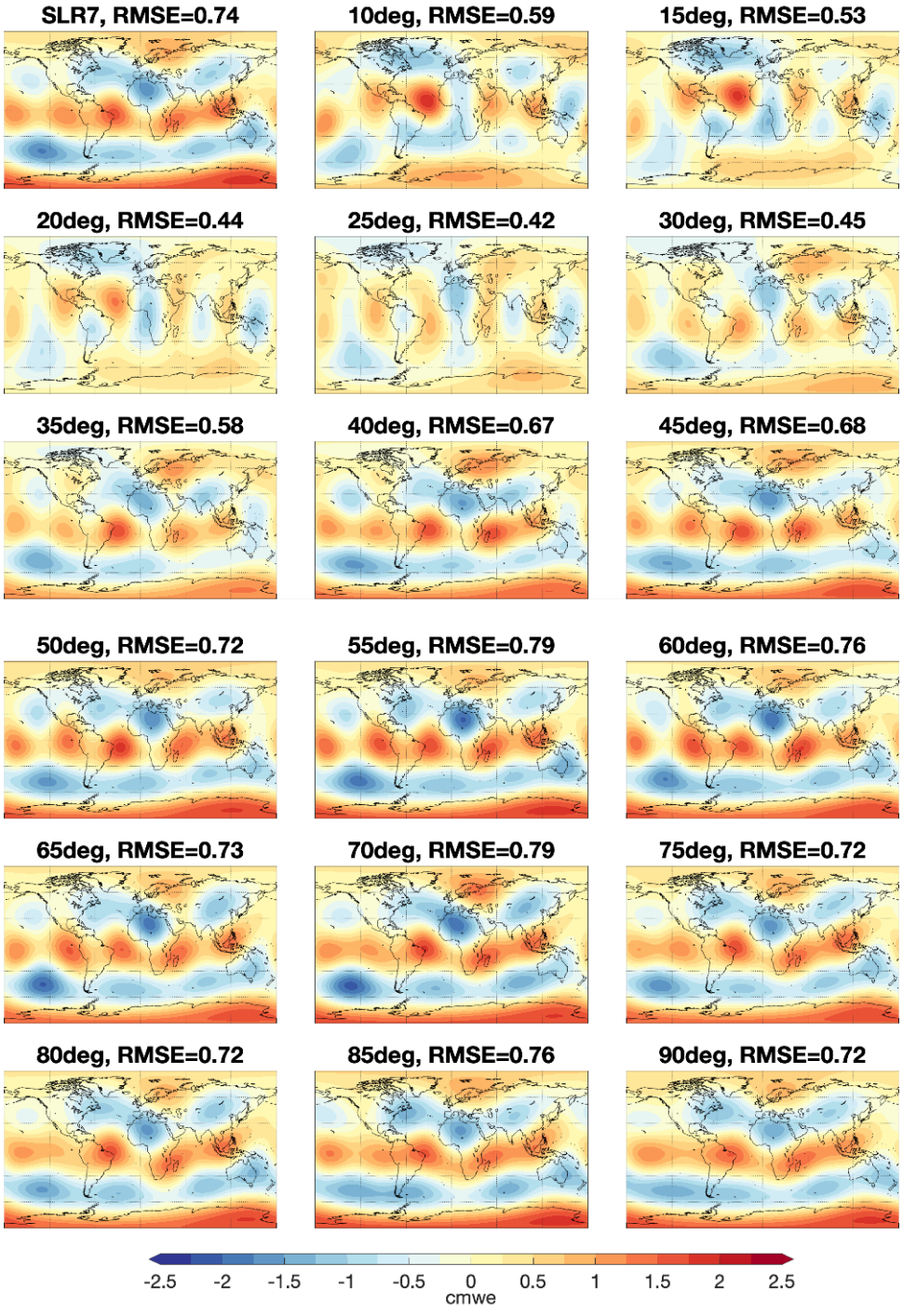

Figure 4.10: Error with respect to the truth of the sine component of the annual variation to degree and order 5.

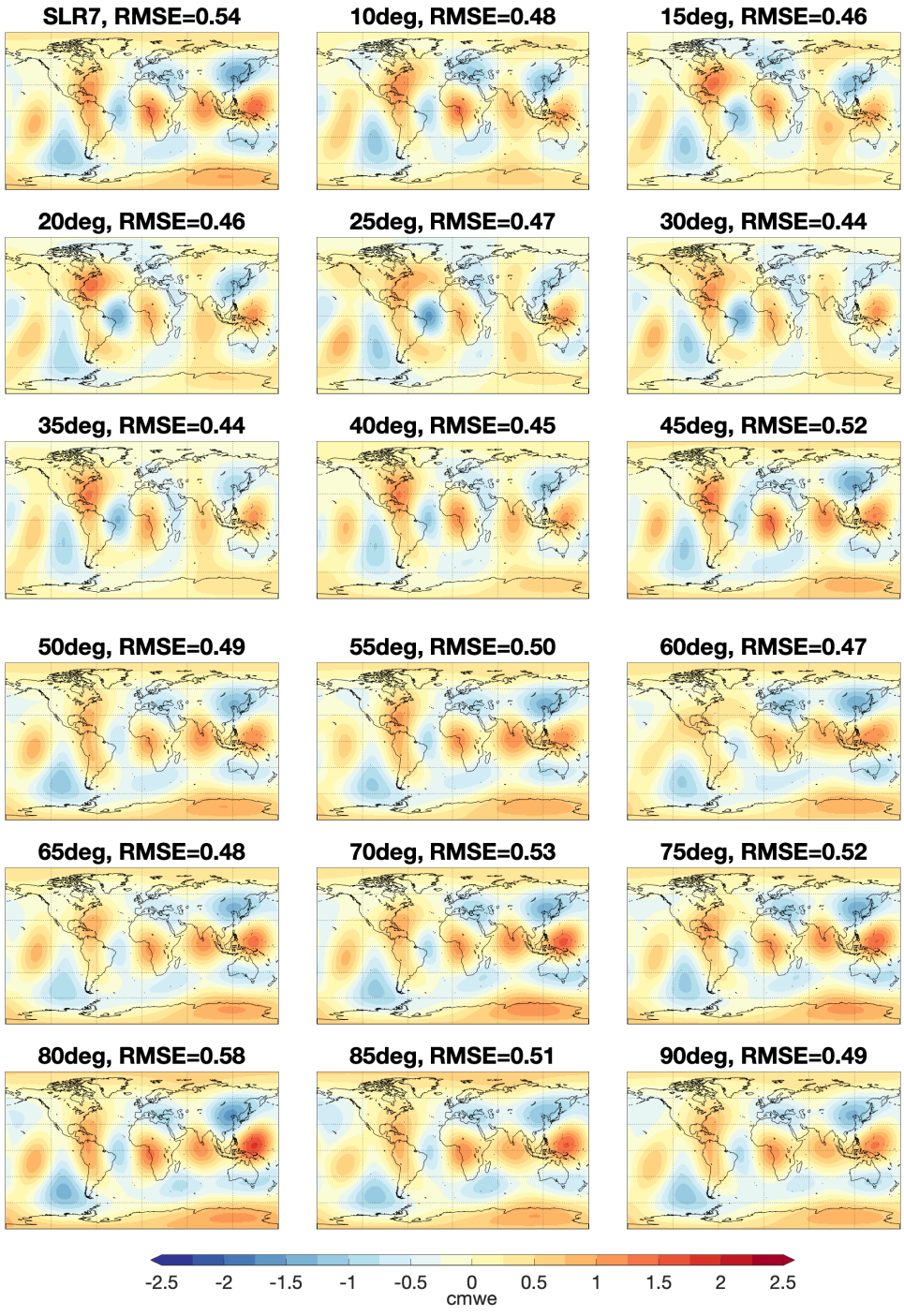

Figure 4.11: Error with respect to the truth of the cosine component of the annual variation to degree and order 5.

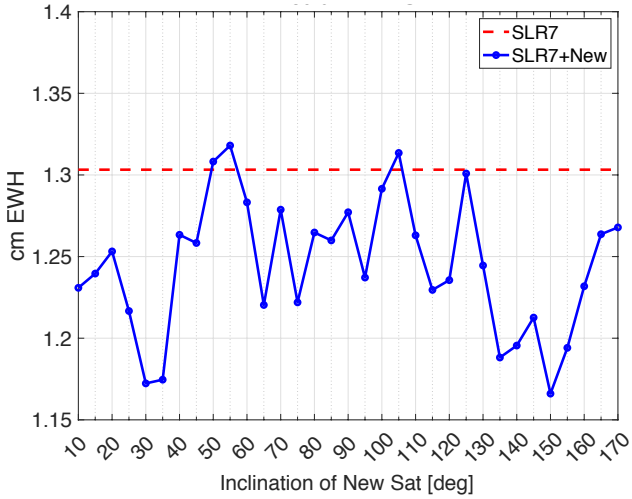

Figure 4.12: Median RMS of spatial errors computed to degree and order 5. The baseline SLR7 value is shown in red.

inclination. Also shown is the power in the hydrology and ice model, allowing for a quick assessment of the signal-to-noise ratio. Degree 6 and order 5 are not shown since these only contain 1 coefficient. For GRACE fields, the degree variance is typically computed to degree ≥ 60, whereas the nature of SLR limits the solution to the first few degrees. For the degree plot, the low-inclination satellite significantly reduces the errors in degrees 2 and 4. Almost no overall change is observed in the odd degrees. The mid and polar inclination satellites have a rather small impact on degree 3 errors, with minimal effects relative to the SLR7 elsewhere. From the order-wise plot, it is clear the largest improvements with the low-inclination satellite come from the zonal and order 1 terms as recognized earlier in Figures 4.6 and 4.7. The low-inclination improvements to the odd zonals do not appear in the degree-wise plot since these are initially well-recovered and certain tesserals are slightly degraded. The mid and high inclination satellites show some promise in improving tesserals, but these gains did not improve the overall solution to the extent that the lower inclination did. In all cases the signal-to-noise ratio remains favorable.

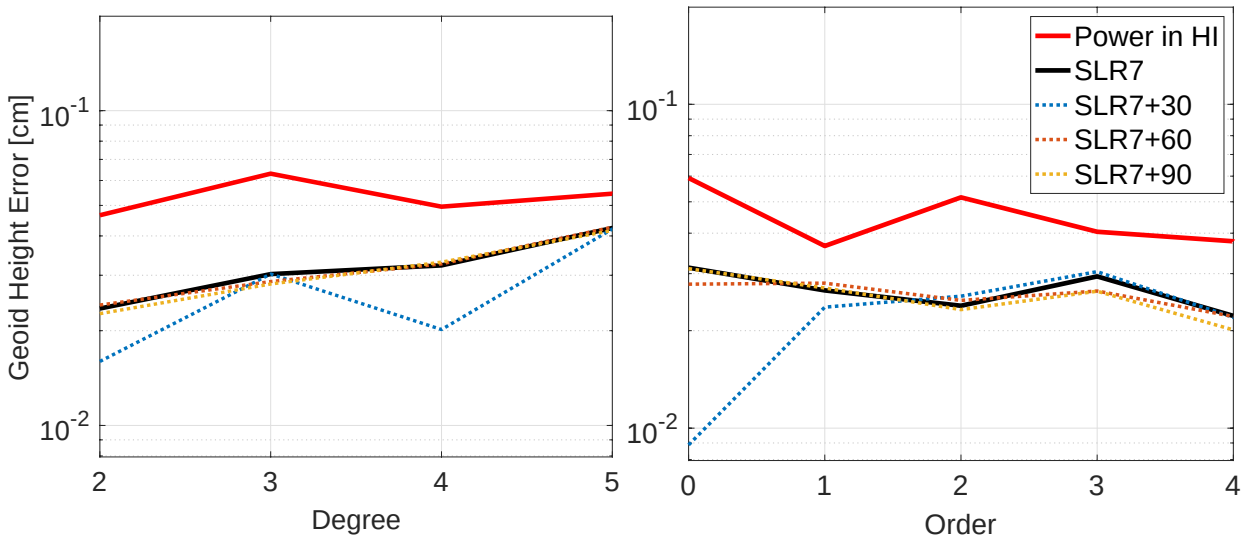

Figure 4.13: Error degree (left) and order (right) amplitudes expressed in cm geoid height for SLR7 and 3 cases of SLR7+New. Also shown is the power in the hydrology (H) and ice (I) signal.

This section examined a number of global metrics to assess the benefit of a new SLR satellite. Even though the 30° satellite mainly improves the even-degree zonal and certain order 1 coefficients,

the overall solution significantly improves in the spatial and spectral domains as these coefficients can carry prominent signals. Although independent SLR solutions have a coarse spatial resolution, they remain important for monitoring global scale mass redistribution and improving their quality can provide additional validation for GRACE.

4.4 Altitude

In this section, particular aspects of a potential new satellite's altitude are explored. The results so far have favored the low-inclination satellite for improving SLR gravity estimates. Naturally, this brings up questions surrounding the number of observations to such a satellite. The collection of SLR data depends wholly on the ground stations. As briefly mentioned in 4.2, lower altitudes can reduce the satellite's visibility from ground stations. This mechanism can be two-fold because the lower altitude will (1) reduce the satellite's time above the horizon at a particular station and (2) possibly make the satellite invisible to certain stations, depending on its inclination and the station's latitude. The latter point becomes a concern when considering the addition of a low-inclination satellite.

Simulations were run over 2 years for the 30° satellite where the altitude was varied in 100 km increments ranging from 600 km to 1,900 km. The average number of monthly observations is reported in Figure 4.14 as a function of the satellite's altitude. In all cases a 15° elevation cutoff is used. For altitudes at or below 1,000 km, the number of observations increases slowly with altitude from just above 1,500 to about 2,500. Between 1,000 km and and 1,300 km, there are two sharp jumps in the observation numbers. For higher altitudes, the observation numbers climb slower with increasing altitude as they did for the lower altitudes. The changes seen in the two "slower" regions ($\leq$ 1000 km and $\geq$ 1300 km) come from the satellite spending more time above the horizon at a particular station. The larger jumps occur as the result of more stations tracking the satellite, namely the mid to high latitude ones in the Northern hemisphere (see Figure 1.2 for the station locations). It is therefore desirable to select an altitude higher than these "transition" zones such that a larger number of stations can track the hypothetical satellite. The altitude of the proposed

satellite throughout this chapter has been sufficiently above this area. Recall also that a satellite's sensitivity to the gravity field diminishes with increasing altitude.

Of course, the next question is whether the actual number of observations is reasonable. For the selected altitude of ∼1400 km, the number of simulated observations depends on inclination, with the mean number of monthly observations varying from about 1200 to 6000. Near lower inclinations, the observation numbers are roughly linear with inclination as they decrease from about 4000 to 2000 for a satellite inclined at 40 degrees versus 20 degrees, respectively. LARES, for example, averaged 5416 ± 1172 (1σ) observations per month over the simulation timespan where this number follows from the actual data. Considering the variability and inclination, the numbers simulated to the new low-inclination satellite are reasonable. Here it is reiterated that there exist a large number of factors that influence the observation numbers. While the simulation incorporates TCC data and has been calibrated to approximate the real data, future studies could seek to improve this approach. However, the results of this section demonstrate (1) that the simulation produces a realistic number of observations and (2) that the network could sufficiently track the hypothetical low-inclination satellite, if an appropriate altitude is selected.

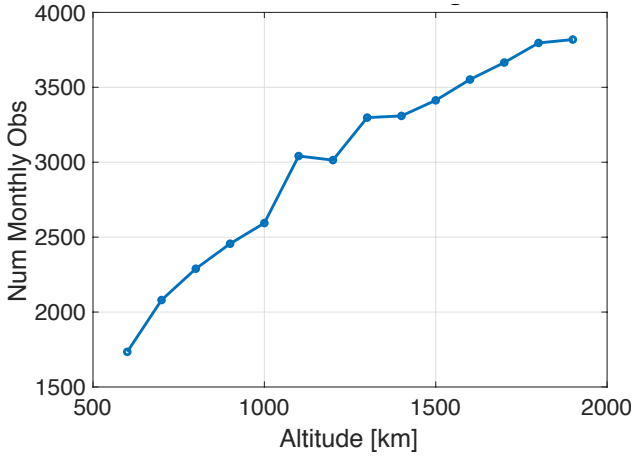

Figure 4.14: Average number of simulated monthly observations versus altitude for a satellite inclined at 30°.

Analytically, one expects the altitude to play a less influential role than inclination on the solution (see Figure 4.1 and Section 4.5). To verify this, the simulation data in this section is

analyzed, where the altitude of the low-inclination satellite is varied. Figure 4.15 shows the changes in the zonal correlations with the new satellite at various altitudes. For the even zonals, there is only a very small change in this value as it becomes slightly more correlated with increasing altitude. The odd zonals show a more distinct, yet still moderate, dependence on altitude where the correlation also increases with altitude. The previous discussions noted that the correlations represent only one aspect of the solution and they do not depend on the actual data. The odd zonals are mainly determined through their periodic effect on the orbit eccentricity and argument of periapsis; however, these elements are also susceptible to mis-modeling of non-conservative forces [Cheng and Ries, 2023; Vallado, 2013]. While the lower altitudes may produce a more favorable correlation, the increased drag environment could corrupt the gravity estimate. Above about 800 km altitude, SRP exceeds the drag force [cf. Table 9-6, Vallado, 2013]. Reflectivity coefficients are often estimated over long data spans (compared to daily/hourly for C_D) and modeling of SRP shows less variability than drag [Vallado, 2013]. The slightly higher altitudes are therefore more favorable for the proposed SLR satellite when considering the drag effects, number of observations, and the fact that SLR gravity solutions are limited to the low degrees. Figures 4.16 and 4.17 show the errors in the sine and cosine components, respectively, of the annual amplitude at the simulated altitudes. The sine component in particular shows a decrease in the overall error for altitudes above 1200 km except for 1700 km, which causes a few tesserals to degrade. As with the varied inclination case, the cosine component does not change much. Overall, the altitude variations clearly impact the solution much less than the inclination variations. All investigated altitudes for the low-inclination case still improve the solution relative to the baseline case.

4.5 Analytical Sensitivity

This section presents results from linear perturbation theory following the techniques described in Section 2.6. Table 4.3 reports D_Ω, the node excitation coefficients (Eq. 2.45), for GRACE, the SLR7, and a 30° inclination satellite. These values agree with those reported in literature and only their magnitude is relevant [e.g., Cheng and Ries, 2017]. Table 4.3 reveals key

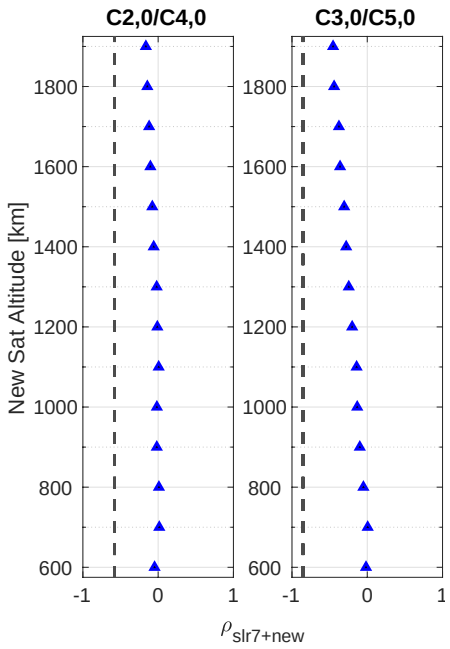

Figure 4.15: Zonal correlations for a new satellite with varied altitude and inclination of 30°. The black dashed line is the SLR7 correlation.

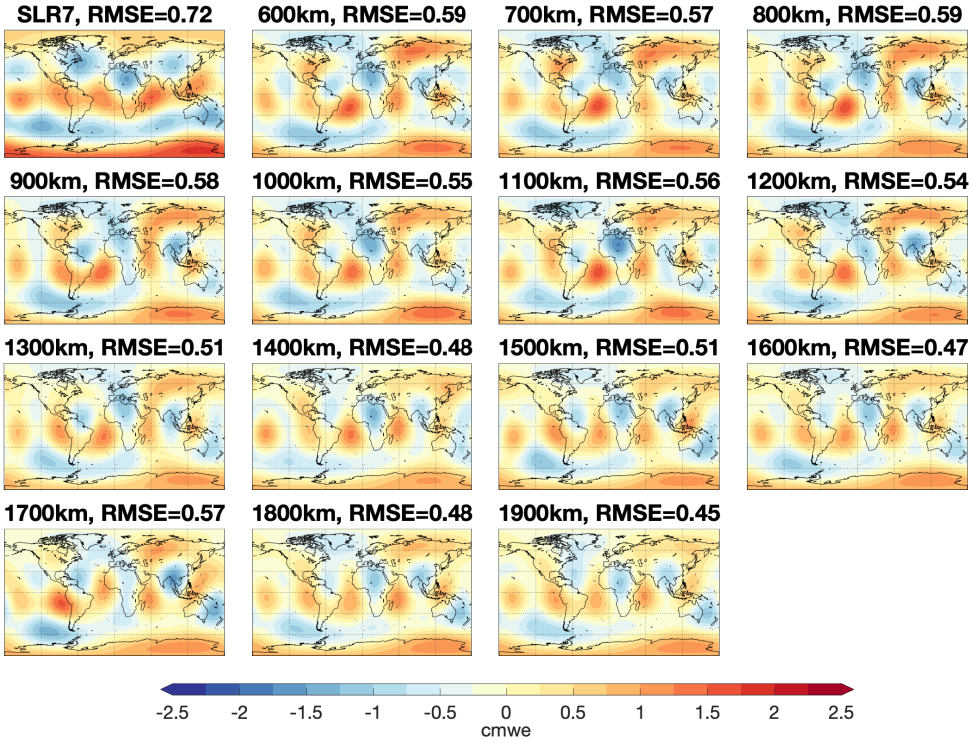

Figure 4.16: Error with respect to the truth of the sine component of the annual variation to degree and order 5 for a satellite inclined at 30°.

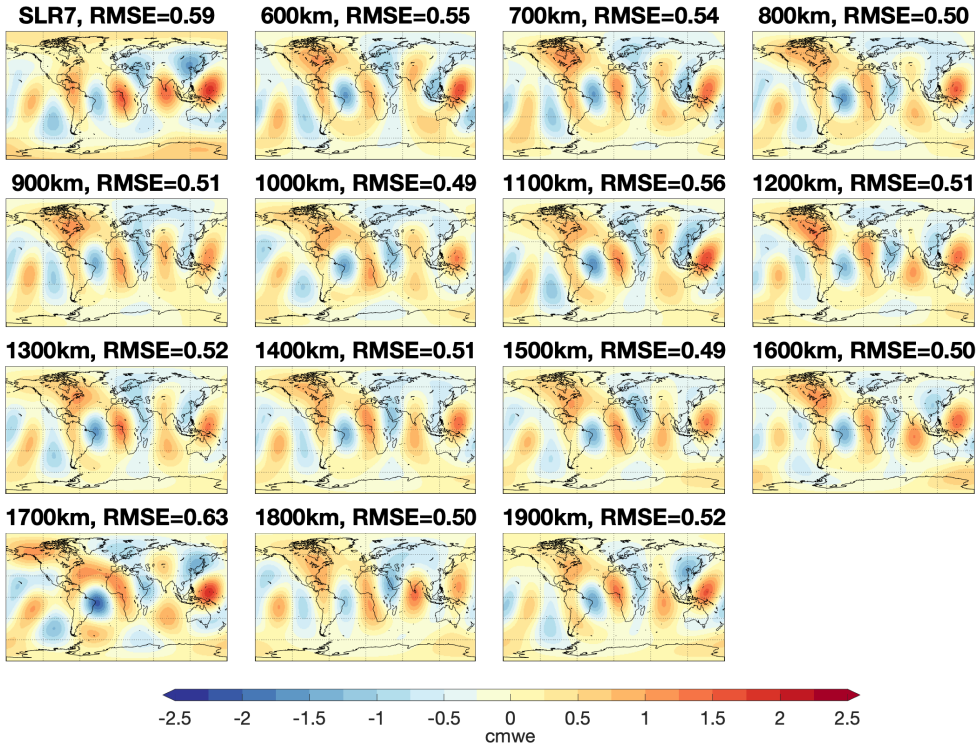

Figure 4.17: Error with respect to the truth of the cosine component of the annual variation to degree and order 5 for a satellite inclined at 30°.

properties of the presented satellites. J_2 represents the dominant perturbation on both LAGEOS satellites, hence their well-known importance in estimating this coefficient. Due to their altitude (> 5500 km), they have almost no sensitivity to terms above degree 6 and the magnitude of the excitation from J_2 is about a factor of 3-10 less than the LEOs. For a particular satellite, the ratio of the sensitivity coefficients between two degrees can reveal the extent of separation between the two degrees [Cheng and Ries, 2017]. Starlette and Ajisai show strong sensitivity to J_2 and very little to J_4. However, the ratios $D_{\Omega,6}/D_{\Omega,4}$ and $D_{\Omega,6}/D_{\Omega,2}$ are high, which indicate influence from this higher degree on the lower ones. Although this is consistent with the discussion in 4.3.3, note that the results in that section came from the combined solution, while individual satellites are investigated here. Stella and Larets show near equal sensitivity to the first 10 zonals, including J_4. LARES also has a near equal sensitivity to J_2 and J_4, and its sensitivity to J_6 is about half this value. Compared to LARES, the hypothetical new satellite is 2.5x more sensitive to J_2 and J_4, but only 1.4x as sensitive to J_6. This sensitivity analysis reveals that a combination solution remains necessary to estimate gravity coefficients from SLR since each satellite effectively senses a "lumped" coefficient. The information from the new satellite becomes extremely valuable and unique when combined with the SLR7. GRACE, due to its polar inclination, lacks sensitivity to the zonals. This insight from perturbation theory supports the numerical results seen so far and demonstrates a possible mechanism for how a low-inclination satellite could benefit the even zonals when combined with the SLR7.

Perturbation analysis of the odd zonals is less straightforward since these coefficients do not induce secular variations on the orbital elements. Further complications arise from mismodeling of non-conservative forces that affect the argument of perigee and eccentricity, which are the most useful elements in studying the odd zonals. With these caveats in mind, the eccentricity excitation (Eq. 2.46) provides some insight regarding the sensitivity of satellites to the odd zonal harmonics as seen in Table 4.4. The limitations of this metric become clear when examining LARES, which significantly improves the recovery of the odd zonals, but shows rather unremarkable sensitivity coefficients. Still, it is known that LARES provides good quality data due to its area-to-mass ratio.

Table 4.3: Magnitude of orbit node excitation coefficients due to zonal harmonics of degree n (mas/yr $\times 10^{-11}$).

n	**GRACE**	**STL**	**LRS**	**STR**	**LAG1**	**LAG2**	**AJI**	**LTS**	**New (30°)**
2	1.5	11.9	20.7	47.9	4.2	7.7	37.3	11.4	51.3
4	2.4	16.7	18.5	2.0	1.5	0.6	1.7	16.8	48.0
6	2.9	17.7	9.2	26.5	0.3	0.5	15.5	18.6	13.2
8	3.2	16.2	1.0	7.3	0.0	0.1	3.9	18.0	11.9
10	3.3	13.3	3.0	13.4	0.0	0.0	5.8	15.9	14.0
12	3.3	10.1	3.5	7.4	0.0	0.0	3.0	13.0	4.2
14	3.2	6.8	2.2	5.8	0.0	0.0	1.8	9.9	3.3

STL=Stella, LRS=LARES, STR=Starlette, LAG1=LAGEOS1, LAG2=LAGEOS2, AJI=AJISAI, LTS=Larets

Stella, Starlette, AJISAI, and Larets are about equally sensitive to J_3 and J_5 and they are all about half as sensitive to J_7. This could explain why J_3 and J_5 are correlated in the SLR7 solution, and why the addition of LARES does not decorrelate these terms, but still improves their recovery. Adding the new low-inclination satellite introduces sensitivity to J_3 and J_5 similar to Stella and Larets. However, it is an order of magnitude less sensitive to J_7, and this reduction of the higher degree influence could explain the notable decorrelation of the lower degree zonals seen from the simulations. The combination of these factors may account for the new satellite's ability to improve J_3 and J_5. Again it is stressed that the analytic theory for the odd zonals is complex and must be considered with other results. While other analytic sensitivity measures for the odd zonals are available, such as those related to argument of periapsis, these will not be presented due to the complications described earlier and because the values in Table 4.4 have been used in the literature [Cheng et al., 1997; Schutz et al., 1993].

Table 4.4: Magnitude of orbit eccentricity excitation coefficients due to zonal harmonics of degree n (mas/yr $\times 10^{-11}$).

n	**GRACE**	**STL**	**LRS**	**STR**	**LAG1**	**LAG2**	**AJI**	**LTS**	**New (30°)**
3	20.3	15.6	4.4	13.3	0.6	1.1	9.6	17.2	16.6
5	21.2	12.1	3.7	13.9	0.2	0.6	8.9	14.5	11.6
7	19.3	6.6	6.7	7.0	0.1	0.0	3.7	9.3	0.9
9	16.9	1.9	5.1	10.8	0.0	0.1	5.2	4.2	6.5
11	14.5	1.5	2.1	1.6	0.0	0.0	0.5	0.2	4.2
13	12.3	3.6	0.2	6.9	0.0	0.0	2.5	2.7	0.2
15	10.4	4.5	1.2	0.8	0.0	0.0	0.3	4.4	2.0

STL=Stella, LRS=LARES, STR=Starlette, LAG1=LAGEOS1, LAG2=LAGEOS2, AJI=AJISAI, LTS=Larets

Focusing on the addition of a new satellite, Figure 4.18 shows contour plots of the even zonal sensitivity coefficients as a function of altitude and inclination for the orbit node. From this plot it is evident that inclination primarily dictates the satellite's sensitivity, followed by altitude to a lesser extent. Also clear is the fact that the satellite's sensitivity declines rapidly with increasing degree regardless of its orbit, although the gradient for altitude becomes steeper for higher degrees (i.e. it

is a more important factor for $n \geq \sim 10$). The lowest inclinations provide the largest sensitivity to the even zonals and there are $n/2 - 1$ "nodes" for each plot where the satellite becomes insensitive to the coefficient. Note that these plots do not consider observation numbers. Considering the first two zonals, Figure 4.18 supports the numerical results seen from varying the inclination. That is, the increasingly polar inclinations provide less sensitivity to the even zonals, and their impact is reduced.

4.6 Conclusions

Novel satellite laser ranging simulations have been conducted to investigate the potential impact of a future satellite on improving time-varying gravity estimates. The simulation procedure applied GRACE-like methods to SLR by including force model errors and a time dependent gravity signal to mimic "real" world data and processing. A multi-year simulation allowed for the application of timeseries analysis techniques. The baseline case comprised 7 currently orbiting geodetic SLR satellites, which were combined to solve for 34 low degree gravity coefficients on a monthly basis. To investigate a new satellite, this work leveraged *a priori* knowledge to determine inclination as the most influential orbital parameter, followed by altitude. The main results of this chapter came from the inclination investigation in which 33 potential new satellites were simulated across possible inclinations. Each one could then be combined with the baseline SLR7 to investigate the impact of the new satellite on the gravity solution.

The numerical simulation environment permitted the computation of a suite of important performance metrics. In discussing SLR-only gravity solutions, one of the first points that comes up is the parameter correlations. Notably, the zonal coefficients of the same parity display non-trivial correlations that means, at a minimum, their accuracy must be carefully assessed in real solutions. This characteristic is also undesirable when substituting SLR coefficients into GRACE data and when applying gap-filling methods that push the limits of SLR's resolution. When adding in a new SLR satellite, a substantial decorrelation of the even zonals was seen with a satellite inclined around 30°. The correlation of the odd zonals reduces as well, although less drastically than the

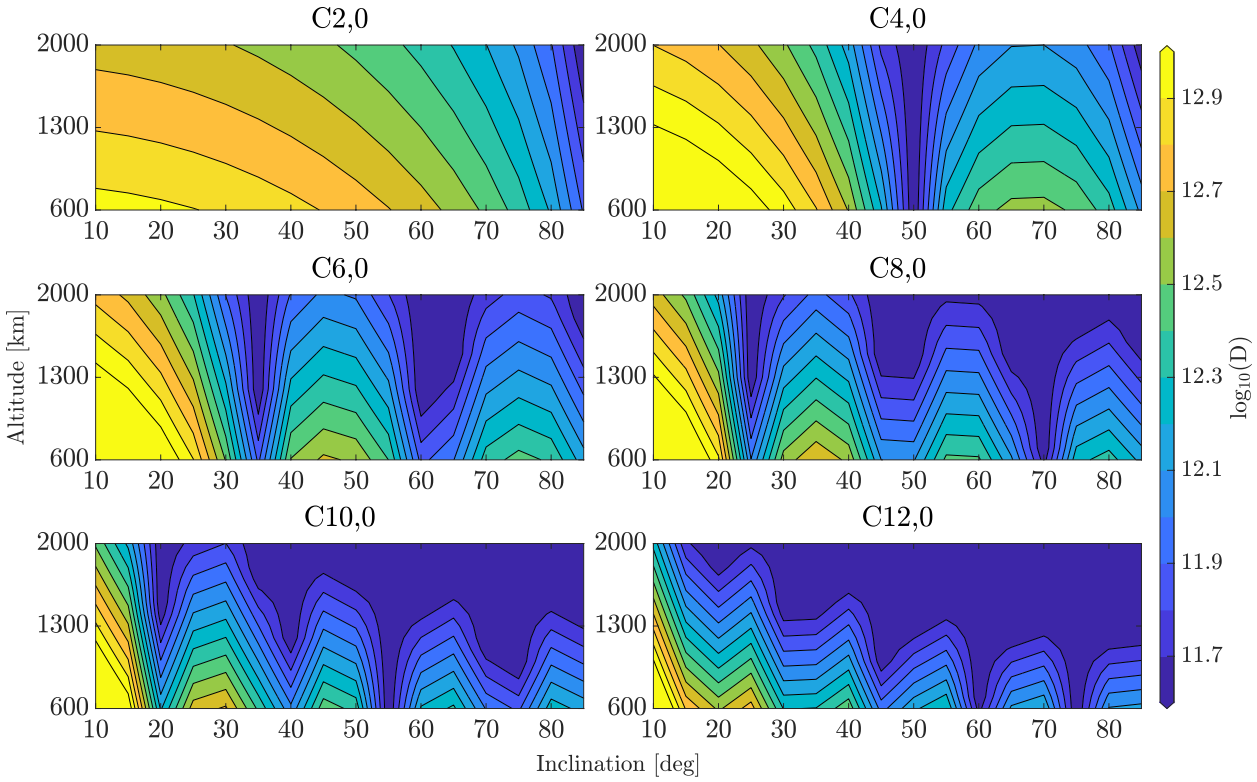

Figure 4.18: Logarithm of node excitation coefficients D_Ω as a function of altitude and inclination for even zonals to degree 12.

even zonals. Such a satellite further reduces the order 1 correlations significantly, but to somewhat varying levels. Following from this, the recovery of the coefficients was directly investigated by comparison to the known truth values. Seasonal fits were computed using least squares for the estimated zonals. In comparing the annual amplitudes, the low-inclination satellites proved most impactful, especially for the even zonals whose amplitude errors saw significant reductions with the new satellite. Likewise, the $\sim 30^\circ$ satellite appreciably reduced the RMS of the zonal and order 1 errors. Overall, the pattern of improvements tended to follow to the pattern of the correlations, although there are factors besides correlation that influence the quality of the solution.

The complete solution with a low-inclination satellite showed improvements in the spatial and spectral domain. Spatially, the recovered annual components as well as the RMS of the retrieval error improved noticeably when considering the full solution complete to degree and order 5. The degree and order variances revealed that the improvements continued to be driven by the zonal and order 1 terms with little changes observed elsewhere. A sensitivity analysis demonstrated that the low-inclination satellite reduces the influence of higher degree terms, particularly for the even zonals. The lower impact of higher degree coefficients on the odd zonals may be due to LARES and could partially explain their good baseline recovery despite their correlation.

Finally, the altitude of a potential new satellite was investigated not only for its impact on the gravity solution, but also for its effect on the low-inclination satellite's visibility. Ideally, the 30° satellite should have a large enough altitude such that high latitude stations can observe it. The additional benefit of a higher LEO altitude is that the drag environment is lessened. In terms of its effect on the solution, the altitude was confirmed to be a minor factor. While the lower altitude improved the zonal decorrelation, the increased perturbations and decreased observations were found to negatively impact the actual solution. Thus, the approximately 30° inclined, 1400 km satellite has been demonstrated through numerical simulations to have a major benefit to SLR TVG solutions. Linear perturbation theory served as an independent check on this result.

Chapter 5

New SLR Ground Stations

5.1 Overview

This chapter focuses on possible improvements to SLR TVG recovery that could come from expansion of the ground segment. Multiple cases are investigated to study the effect of improved network geographic distribution as well as a realistic scenario that could be realized in the coming decade. The impact of a single station is found to be fairly small, though relatively significant given that there are currently over 40 operational SLR ground stations. The largest effects are seen with a new station that fills a geographical gap, most notably in the Southern hemisphere and polar regions. To investigate the limitations of ground stations, a test case is run involving a uniformly distributed network that reveals new ground stations cannot decorrelate key coefficients in the way new satellites can. Despite this result, the additional data from new ground stations benefits the recovery of the gravity field.

5.2 Investigated Cases

As with new satellites, the search space for a new station must first be defined. The overall search space for a new station is smaller than for the new satellite since latitude and longitude represent the only two parameters for placing a single station, assuming it sits on the surface of the Earth. Realistically, ocean covers 70% of the Earth and numerous geopolitical, environmental, and logistical factors influence the ability to construct new stations. Most of these considerations fall outside the scope of this work, although the simulation does consider total cloud cover in generating

data. The ILRS maintains a list of future stations, which has been reproduced in Table 5.1. In the coming years, several new stations are planned although publicly available up-to-date information regarding timelines cannot always be located. Additionally, a "new" station can sometimes mean an upgrade to an existing system, which may also pause operations at that station. Notwithstanding this list, the analysis in this chapter will also consider stations in other locations. There is insight to be gained through studying fringe or unrealistic cases, such as hypothetical stations placed in open ocean, and the overarching question of this chapter deals with the overall potential impact of new tracking stations.

Table 5.1: ILRS Future Stations List[1]

Station	Country	Timeframe	Notes
Irkustk	Russia	2022	Co-located with IRKL 1891
La Plata	Argentina	2022	Relocation from Concepción, Chile
Mendeleevo	Russia	2022	Co-located with MDVS 1874
San Juan	Argentina	2022	Upgrading existing system
Yebes	Spain	2023	New station
Metsahovi	Finland	2023	Replacing METL 7806
Mount Abu	India	2023	New station
Ponmudi	India	2023	New station
Tsukuba	Japan	2023	New station
Ny-Ålesund	Norway	2024	New station
McDonald, Texas	USA	2025	Upgrading existing system
Haleakala, Hawaii	USA	2027	Upgrading existing system

[1] `https://ilrs.gsfc.nasa.gov/network/stations/future/index.html`. Accessed: 6 February 2023.

Three cases are defined that form the core of this analysis, in addition to the current or baseline SLR ground network (hereby called N-0). Figure 5.1 displays maps of each setup. In case N-1, single new stations are placed at regular geographic intervals and a solution is formed that combines N-0 plus each individual new station (Figure 5.1a). This case considers the 72-point grid spaced 20°by 45°in latitude/longitude, respectively, and bounded latitudinally at ±80°. Case N-2 presents a more realistic scenario. From Table 5.1 5 stations have been selected that would geographically diversify the network, all of which are simultaneously combined with N-0 to form a single solution (Figure 5.1b). Two of these stations, La Plata and San Juan, will be in Argentina as

a relocation and upgrade, respectively. Two more, Mount Abu and Ponmudi, are planned for India where no stations currently exist. The Ny-Ålesund station will sit at a latitude of nearly 79°N in the archipelago of Svalbard, Norway, making it the only SLR station in the Arctic circle. Finally, case N-3 explores the impact of a geographically uniform network (Figure 5.1c). Such a layout is obviously impossible, but this is done so that the limits of new ground stations can be quantified in terms of their ability to improve SLR TVG estimates.

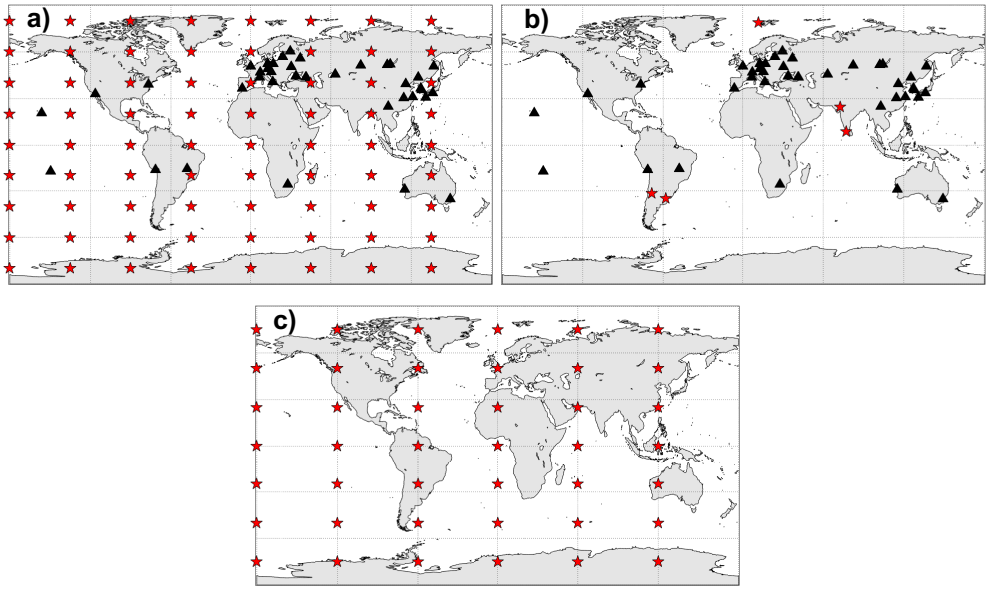

Figure 5.1: Maps of simulated cases. The baseline network (N-0) is shown as black triangles and new stations as red stars. Case N-1 (a) evaluates N-0 plus individual new stations along the displayed grid. Case N-2 (b) considers N-0 plus 5 potential future stations. Case N-3 (c) considers a 42-station geographically uniform network (not combined with N-0).

5.3 Numerical Simulation Results

5.3.1 Single New Station

Case N-1, where a new station is placed at predefined grid points, is evaluated to assess the geographic dependence of a new station's benefit to TVG (Figure 5.1a). While this method introduces locations where a station could not practically exist, such as open ocean, it has proven successful for investigating global patterns [Otsubo et al., 2016; Kehm et al., 2019]. This case

effectively assesses influences from a single new station relative to the current SLR ground station geometry.

Compared to new SLR satellites, one may reasonably expect a new station to have an overall lower impact on the gravity solution given that there are only 7 geodetic SLR satellites compared to over 40 ground stations. Since a new station is only $2-3\%$ of the total network, the results are best analyzed using formal statistical metrics. The changes from a new station are quantified by (1) reductions in the formal uncertainties, which relate to the network's geometric sensitivity and ability to observe a parameter and (2) changes in the normal matrix condition number [Otsubo et al., 2016; Kehm et al., 2019; Glaser et al., 2019]. Figure 5.2 displays the relative improvement in the median formal error for all estimated C_{nm} and S_{nm} gravity coefficients of degree n and order m. With a near-equatorial station, the even zonals ($m = 0$) show small improvements of about 4%. The odd zonals, however, benefit most from an Antarctic station with the network becoming up to 12% and 10% more sensitive to $C_{3,0}$ and $C_{5,0}$, respectively. The C and S odd-degree order 1 tesserals ($0 < m < n$) display a similar pattern, but also show reductions in the formal errors with the addition of a mid-latitude Southern hemisphere station ($\leq -40°$). For the even-degree order 1 coefficients, a Southern hemisphere or equatorial station generally improves the sensitivity $3-5\%$.

The sensitivity of the network to the sectoral coefficients ($m = n$), especially the even ones, increases most with the addition of a station near either pole, although a South polar station is more impactful. An Antarctic station improves $C_{2,2}$ and $S_{2,2}$ up to 13% as well as $C_{4,4}$ and $S_{4,4}$ up to 16%. Such a station also benefits the odd sectorals by up to 10%. The relative improvements in the remaining tesseral terms tend to follow the previously described patterns. For example, an Antarctic station would improve $C_{4,2}$ and $S_{4,2}$ up to 13% with smaller changes of $3-7\%$ seen at mid-latitudes and high Northern latitudes. These results demonstrate that adding stations in the Southern hemisphere would provide the network additional sensitivity to the low-degree gravity coefficients.

The qualitative patterns in Figure 5.2 have some agreement with those reported in Otsubo et al. [2016], who found that a low, mid, or high latitude station most improves the zonals, tesserals,

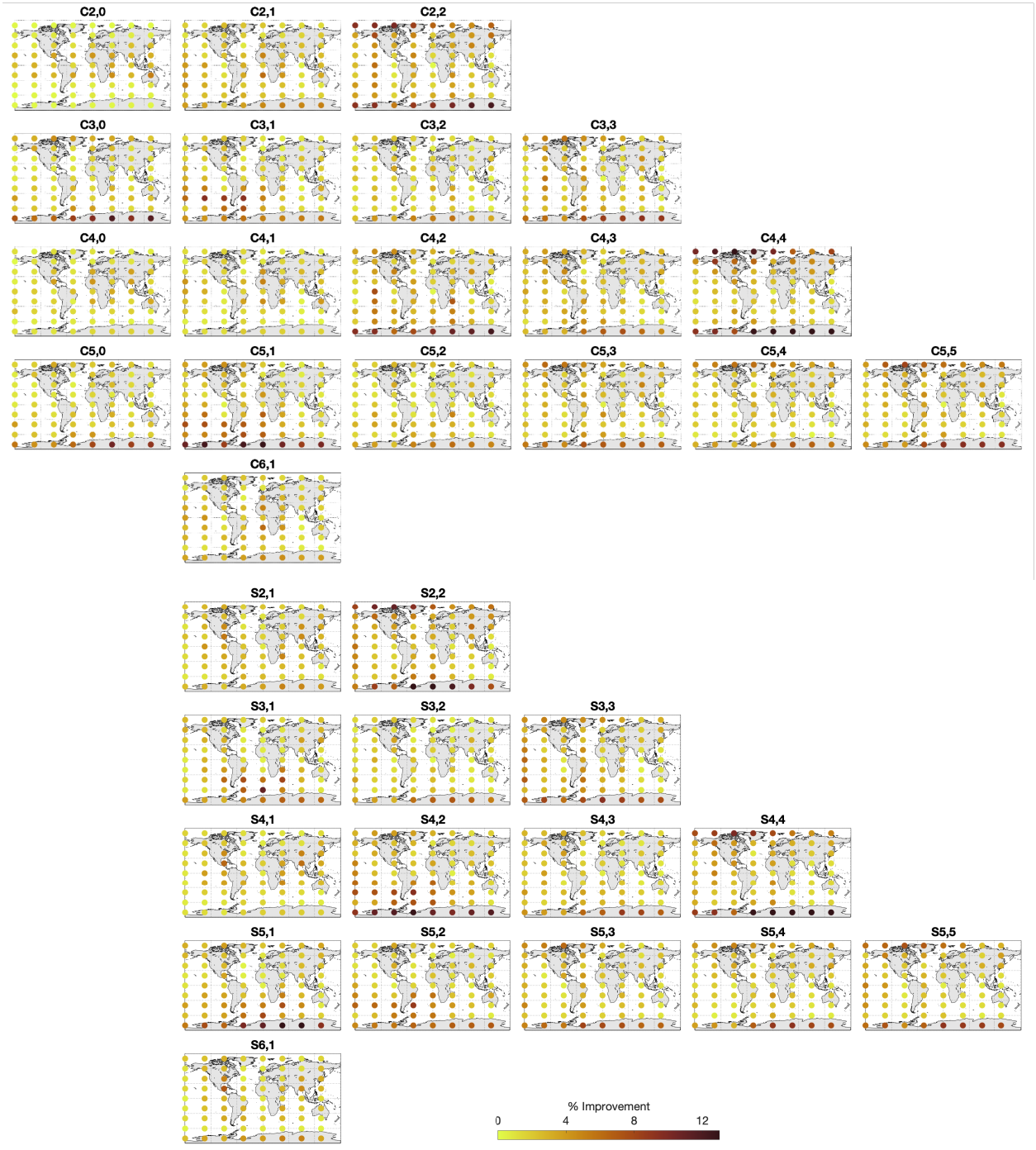

Figure 5.2: Case N-1 improvements in the median formal error to estimated gravity coefficients with a new station at indicated grid points.

or sectorals, respectively. The results agree for the sectoral and even zonal coefficients, but the odd zonals and odd order 1 terms favor an Antarctic station in this study. The even-degree order 1 terms in the results of this work show comparatively smaller improvements. The slight disagreements likely come from methodological differences since we have included TVG models and estimated a larger, monthly set of gravity coefficients.

The condition number (κ) of the normal matrix N, defined as the ratio of its maximum eigenvalue λ to its minimum one, relates to the stability of the inversion and solution quality,

$$\kappa(N) = \frac{|\lambda_{\max}|}{|\lambda_{\min}|} \tag{5.1}$$

A high condition number means the solution will have a large response to small changes in the input data due to noise, observation errors, or model errors. Figure 5.3 shows the relative improvement (reduction) in the median condition number of the normal matrix with the addition of new stations in N-1. Qualitatively, the improvements appear where a new station either fills an observational gap or adds data to a poorly covered region compared to Western Europe or East Asia. The addition of an Antarctic station again has the largest impact at $\sim 12\%$, followed by low to mid-latitude stations in the Pacific, which affect the condition number by $5-12\%$. Similar improvements of $5-10\%$ are seen with a Northern high-latitude station. In discussing condition numbers, these improvements are fairly small. Recall, however, that the new station would exist among over 40 current stations, meaning a new station will have inherent limits in the magnitude of the improvements it provides. Still, the effect of improving the uniformity of observations is clear from Figure 5.3.

5.3.2 Multiple Future Stations

In case N-2, 5 potential future stations are added to N-0 to form a solution that could represent the SLR ground network within the next decade (Figure 5.1b). Figure 5.4 shows the relative improvement in the median formal errors for each coefficient and is comparable to the information content provided in Figure 5.2. Also shown are the improvements for N-1 with a best-case Antarctic station (case N-1A) and N-3, which is discussed in 5.3.3. Most coefficients in N-2

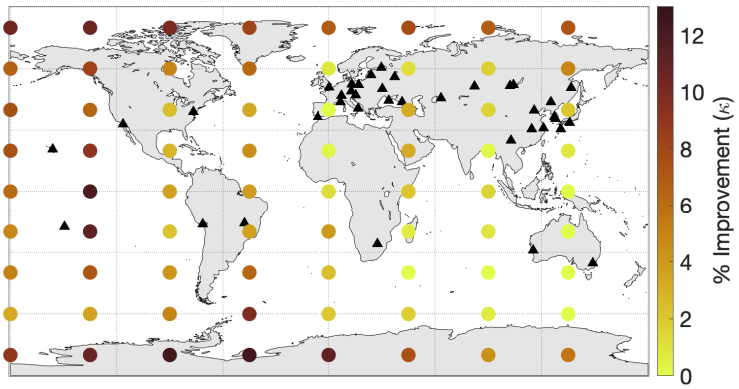

Figure 5.3: Case N-1 relative improvement in the median condition number (κ) of the normal matrix with a new station at indicated grid points.

improve by $> 10\%$ and it is clear that, for individual coefficients, the addition of multiple stations generally increases the magnitude of the improvements compared to N-1A. From the analysis of N-1 one would expect the sectorals and tesserals to improve more than the zonals given the addition of 2 Southern hemisphere stations and one in Ny-Ålesund. As a whole, the median improvement in the zonals, tesserals, and sectorals is 11%, 13%, and 15%, respectively. The solution has a range of improvements within each group, especially the tesserals since this category has the most coefficients. $C_{4,1}$ and $S_{3,2}$ change only by 7% whereas $S_{4,2}$ improves by 19%. The odd-degree order 1 C and S terms all benefit over 16%. While the even zonals only improved up to 4% in N-1, we now see a 10% and 12% improvement in $C_{2,0}$ and $C_{4,0}$, respectively, that could be driven by the relatively low latitude of the proposed stations in India. The median condition number in N-2 reduces by 12% compared to N-0, which is the maximum improvement seen with a single Antarctic station in N-1. Based on Figure 5.3, the improved conditioning seen in N-2 likely comes from the combination of the South American and Ny-Ålesund stations. These results clearly highlight that diversifying the geographic distribution of stations would improve SLR-derived TVG estimates.

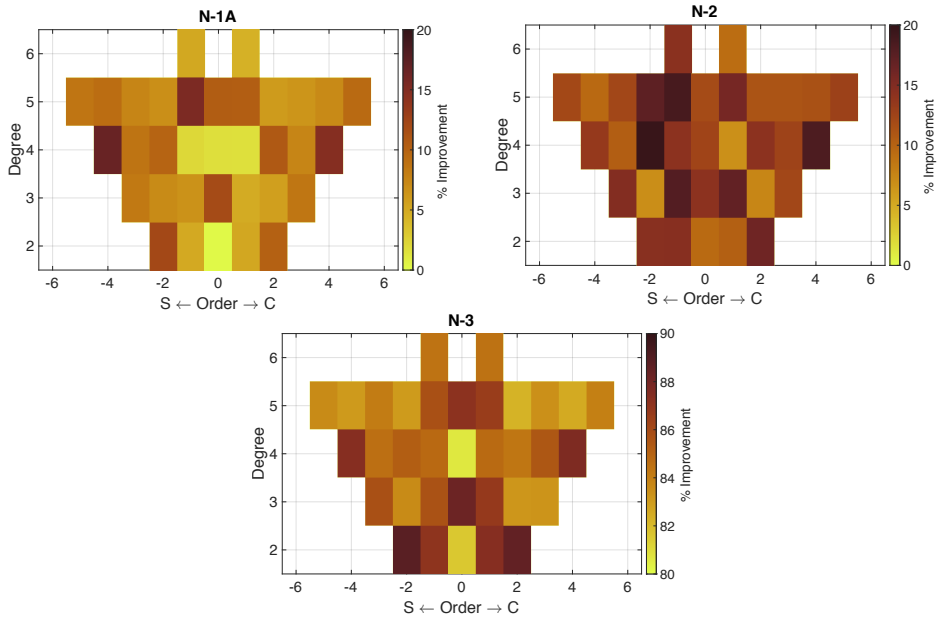

Figure 5.4: Percent improvements relative to N-0 in the median formal errors for estimated coefficients for cases N-1A, N-2, and N-3. Note the different colorbar limits for N-3.

5.3.3 Uniform Network

To assess the upper limit of the impact new stations can have on TVG, an extreme test case (N-3) is run with complete and homogeneous tracking. The goal of this test is to reveal upper limits on the magnitude and pattern of improvements from a uniform SLR network with dense tracking because a new station mainly benefits the existing network in one or both of these ways. This case has 42 tracking stations in a 25° by 60° latitude/longitude grid, respectively (Figure 5.1c). For this test, the latitude of the stations is bounded at ±75° and, relative to realistic tracking, the number of observations increases by a factor > 10. With the current SLR constellation, a polar station would not produce observations directly over the poles due to the satellites' inclinations. Although this test case is an unrealistic scenario, it will highlight important properties of the network by exploring its potential limits.

Figure 5.4 shows the improvements in the formal errors relative to N-0. With N-3, we see the formal errors reduced by $> 80\%$ for all estimated coefficients. $C_{2,0}$ and $C_{4,0}$ improve 82% and 81%, respectively. The odd zonals benefit slightly more than the even ones, improving by 87-88%. The even-degree sectorals also show large changes, with $C_{2,2}$ and $S_{2,2}$ improving 89% and $C_{4,4}$ and $S_{4,4}$ improving 88% and 87%, respectively. The odd-degree sectorals benefit about 2-3% less than the even-degree ones. Relative to N-0, the normal matrix condition number in N-3 is reduced nearly 30%. This is relatively large compared to the changes in N-1 and N-2 and highlights the overall value of uniform observations.

5.4 Parameter Correlations

An established property of SLR-only gravity estimates is that certain parameters display high formal correlations as discussed in 4.3.1. Recall that this is apparent in several low-order terms of the same degree parity. Figure 5.5 shows the mean correlation matrices for cases N-0, N-1A, N-2, and N-3. For N-0, we see $\rho_{C_{2,0}}^{C_{4,0}} = -0.58$ and $\rho_{C_{3,0}}^{C_{5,0}} = -0.85$. Likewise, the even order one terms are correlated with $|\rho| \geq 0.8$, for example $\rho_{S_{2,1}}^{S_{6,1}} = 0.85$. Other coefficients of a given order and

degree parity are slightly to moderately correlated ($0.1 < \rho < 0.5$). No station in N-1 has a notable effect on these correlations. Even with the 5 additional stations in N-2, the zonal and even-degree order 1 correlations remain unchanged. In N-3, where stations were distributed globally, nearly all coefficients decorrelate except for the zonals, order 1, and odd-degree order 2 terms as seen in Figure 5.5. This result suggests a limitation of the geographic distribution of stations to decorrelate certain coefficients given the current satellite constellation.

Correlations between parameters can present challenges in assessing the reliability of real solutions. These limitations can be overcome, but care must be taken during the data processing and solution validation. A significant reduction in the formal errors can mitigate the impact of correlated parameters. Loomis et al. [2020] observe this kind of behavior when adding the LARES satellite to the solution, as $\rho_{C_{3,0}}^{C_{5,0}}$ decreases only slightly, but the formal errors reduce by a factor of 3 and both $C_{3,0}$ and $C_{5,0}$ improve overall. When adding new stations, the solution improves as a whole even if certain parameters remain correlated. This is seen in Figure 5.6, which shows the median error degree amplitudes with respect to the truth for N-0, N-1A, N-2, and N-3. N-1A most improves the odd degrees, with little change to the even degrees. N-2 improves the odd degrees about the same as N-1A and further improves degree 4. As expected, N-3 significantly reduces errors across all degrees, with a slight preference to the odd ones. These results demonstrate that adding new stations is essential to improving the overall solution quality even if a geographically uniform network does not decorrelate certain parameters.

One should bear in mind that correlations are a formal metric arising out of covariance analysis and they do not necessarily invalidate increases to parameter sensitivity as the results have shown. Other steps could also be taken mitigate the impact of the correlations, such as including a TVG forward model during data processing [Loomis et al., 2019]. This requires *a priori* data and is not analyzed here. While it is disappointing that new stations are limited in their ability to decorrelate certain gravity parameters, the result makes sense if they are compared to the mathematical basis of estimating the gravity field from SLR. Estimation of TVG from SLR relies on the satellites' sensitivity to gravitational perturbations. Consider the even zonal harmonics, for

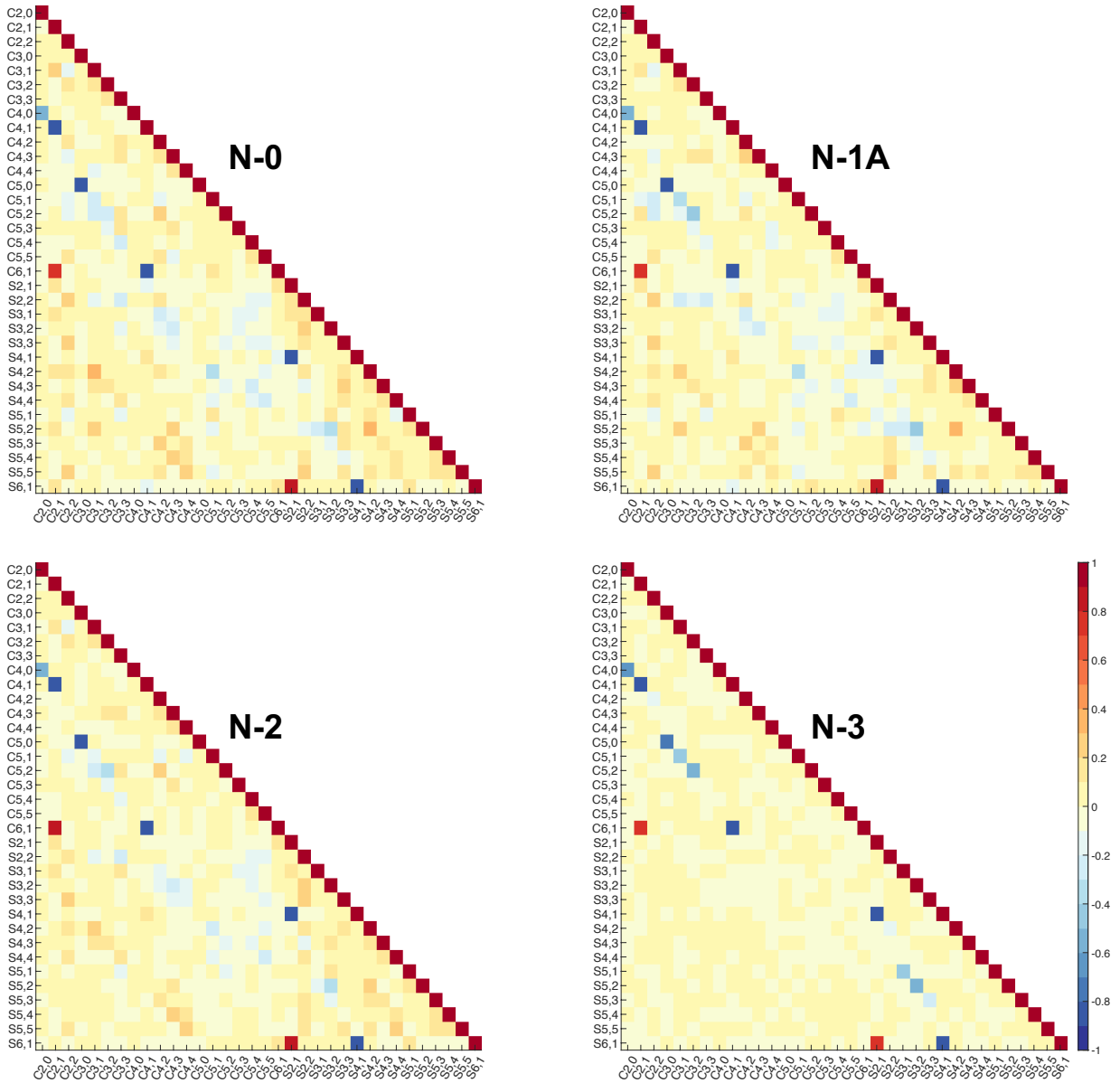

Figure 5.5: Correlation matrices for cases N-0, N-1A, N-2, and N-3.

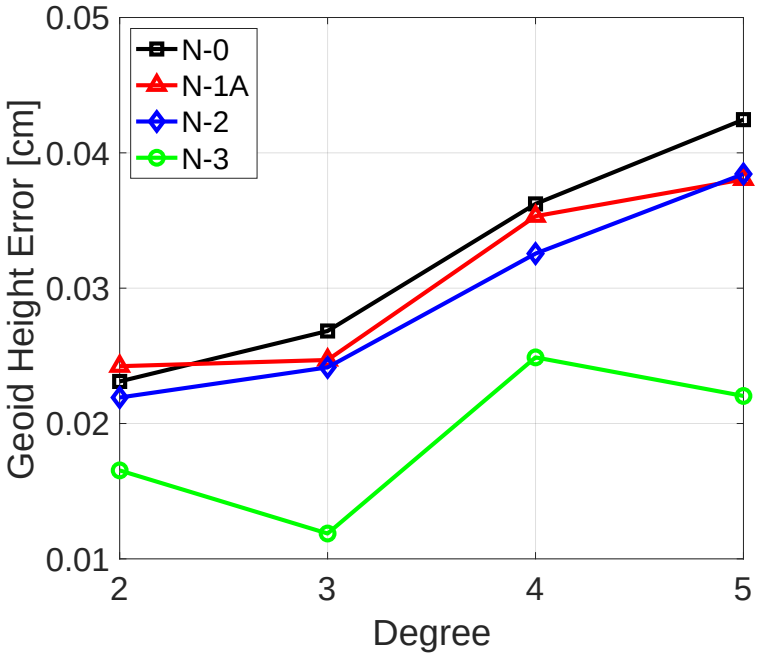

Figure 5.6: Median error degree amplitude with respect to the simulated truth for cases N-0 (black squares), case N-1A (red triangles), case N-2 (blue diamonds), and case N-3 (green circles).

example, which induce secular variations on the orbit node (Ω) of a satellite [Kaula, 1966]. The even zonals also cause secular variation of the mean anomaly (M) and argument of perigee (ω), but these are less useful in practice as atmospheric drag affects M and most SLR satellites are in near-circular orbits [Yoder et al., 1983]. The secular rate of the orbit node due to the even zonals can be expressed using well-known linear perturbation theory as seen in Eqs. 2.44 and 2.45. Inspection of these equations reveals the primary dependence of the correlations on SLR satellites instead of ground stations. To decorrelate certain parameters in SLR-derived TVG estimates, new satellites are required with unique sensitivities that could separate the low-order terms. For each SLR satellite, geophysical mass variations induce a spectrum of gravitational perturbations, with its orbital parameters dictating its sensitivity to the perturbations as seen in Eqs. 2.41-2.44 and as noted in prior work [Cheng et al., 1997; Dong et al., 1996; Kaula, 1966]. Therefore, SLR satellites at a variety of altitudes and inclinations are required to separate these so-called lumped effects, and there will exist an inherent limitation of ground stations to mathematically decorrelate these coefficients. Chapter 4 simulated the impact of a hypothetical new SLR satellite on TVG estimates. These analyses found that a new low-inclination SLR satellite, when combined with the current SLR satellite constellation, would significantly decorrelate the even zonals and order 1 terms and lead to greatly improved recovery of these coefficients. Although the results of this chapter highlight limitations of dealing with correlated parameters, they also demonstrate that such parameters can still improve as new stations generate more data and diversify the network's geometry.

5.5 Practical Aspects

In reality, the tracking network will never have an ideal geographic distribution. The most reasonable cases for the near future are N-1 or N-2. In N-1, an Antarctic station was shown to provide the most benefit for TVG recovery. Existing work has also demonstrated the potential improvement an Antarctic station would have on other geodetic parameters [Otsubo et al., 2016; Kehm et al., 2019; Glaser et al., 2019]. Yet despite these investigations, an Antarctic SLR station has not materialized, with the only known current proposal being the Japanese-led station in

Syowa that is still in its conceptual stage [Otsubo et al., 2019]. No reviewed sources contained a timeline for this station and the ILRS does not list it as a future addition. Here, several challenges are deduced in constructing and operating an Antarctic station. Selecting a location does not appear to present a problem as Antarctica already hosts numerous scientific observatories, such as McMurdo and Syowa Station. Perhaps the largest initial hurdle that all new stations face is securing adequate funds for building and equipment. The remote location and harsh weather conditions of Antarctica likely increase the required capital to develop a new SLR station. The upcoming arctic Ny-Ålesund SLR station, for example, comes as a collaboration between the Norwegian Mapping Authority and NASA; thus, an Antarctic station may benefit if funds were sought from multiple agencies as part of an international cooperation [Breivik et al., 2022]. Besides the initial costs, an Antarctic station would face logistical challenges related to the unique operating environment. A combination of extreme temperatures, strong winds, icing, and high levels of cloud cover could inhibit the performance of an Antarctic station as Kehm et al. [2019] note. Of course, this could lead to increased maintenance requirements, which may pose further challenges depending on the frequency and complexity of issues. Many of the points described here remain speculative and future technical investigations should study these in more detail.

Although an Antarctic SLR station does not appear to be coming in the near future, there are several other new stations set to come online this decade. A single new station from Table 5.1 may only have a small impact on SLR gravity estimates since its location is not strictly "ideal" based on the results of case N-1. However, the results of N-2 show that combining several new stations in feasible locations could provide improvements in excess of any single station in N-1 (Figures 5.4 and 5.6). While there exists some dependence of the improvements on latitude, the more apparent pattern is that the network benefits from stations in new geographic areas. Even in well-covered areas, new stations increase tracking capabilities and provide redundancy in case nearby stations need to go offline.

5.6 Conclusions

This chapter has presented a simulation study of the possible impacts of new SLR tracking stations on low-degree TVG estimates. While systematic improvements to the coefficients were not obtained as was the case with a new satellite, new stations can improve the overall sensitivity to certain groups of coefficients. The results highlight the benefit of polar and Southern hemisphere stations for gravity recovery (see case N-1). The odd zonals, tesserals, and sectorals all show improvements up to 16% with such stations. The even zonals improve about 4% with a low latitude station. Given the magnitude of $C_{2,0}$ compared to other coefficients, an improvement of this size could have significant geophysical implications. A potential future scenario with 5 new stations was also investigated (see case N-2) that included the upcoming Ny-Ålesund station. The increased data volume and geographic diversity increased the network's sensitivity to all estimated parameters, especially the sectoral coefficients. This study expands upon recent work that has noted the impacts of new stations on Earth orientation and reference frame parameters Otsubo et al. [2016]; Kehm et al. [2018, 2019]; Glaser et al. [2019]. To assess the upper limits of new stations, case N-3 analyzed an ideal geographic configuration in which large amounts of data were simulated to a uniformly distributed SLR tracking network. This achieved significant reductions in the formal errors, while the zonal and order 1 coefficients still displayed high correlations as they do in the baseline solution. This case demonstrate that new stations have a limited ability to decorrelate low-order gravity terms, a result supported by analytical perturbation theory. However, the results showed that new stations improve the error degree variance despite correlated parameters.

Chapter 6

Combining SLR and GRACE

6.1 Overview

The GRACE and GRACE-FO missions have undeniably revolutionized our ability to observe global mass-change. The preceding investigations in Chapters 4 and 5 focused on independent SLR solutions of low degree TVG, which remain critically important despite GRACE's success. As discussed in Chapter 1, SLR supports GRACE through its estimates of $C_{2,0}$ and $C_{3,0}$. This chapter investigates strategies for combining GRACE and SLR data. Mathematically, the term "combination" refers to a joint GRACE and SLR solution in which the data (observations or normal equations, see Eqs. 2.23, 2.34, and 2.35) are merged prior to the inversion. At the time of this study, however, analyses involving GRACE data overwhelmingly favor the "substitution" method. In this procedure, GRACE and SLR solutions are formed independently and the SLR-only estimates of $C_{2,0}$ and $C_{3,0}$ are substituted directly into the GRACE solution. Typically in this thesis, *combination* and *substitution* will refer to their respective methodology, except where otherwise noted. This chapter leverages the simulation setup to uniquely compare these two analysis procedures and their impact on signal recovery. The focus is primarily on quantifying improvements with the combination solution given the straightforward nature of the substitution approach.

6.2 Simulating GRACE

The general process for simulating GRACE follows the same *truth* and *nominal* process used for simulating SLR. GRACE K-band range-rate data (KBRR) are simulated in 1-day arcs. Prior

to forming the normal equations, an orbit convergence run is conducted that estimates the daily Cartesian state, daily accelerometer biases and trends, and 3-hourly KBRR bias, trend, and once-per-rev parameters. The data reduction run then forms the normal equations containing partials for the daily satellite state, daily accelerometer biases, trends, and scale factors, 3-hourly KBRR once-per-rev parameters, and the gravity coefficients.

To replicate the actual GRACE mission, noise from the accelerometers and ranging instrument is added to the simulation. Instrument noise on the K-band microwave ranging system is approximated by white noise with spectral density of 1.8 $\mu\text{m}/\sqrt{\text{Hz}}$ [Loomis et al., 2012]. Also included in the GRACE simulation are noise models for the accelerometer and star cameras based on the best GRACE-FO pre-launch estimates [Wiese et al., 2022, David Wiese, personal communication]. The amplitude spectral densities (ASD) of the accelerometer errors are given in the spacecraft body frame with units $\text{m/s}^2/\sqrt{\text{Hz}}$,

$$d_{acc,x} = 3 \times 10^{-11} \sqrt{1 + \left(\frac{f}{0.6}\right)^4 + \frac{0.014}{f}}$$

$$d_{acc,y} = 4.6 \times 10^{-10} \sqrt{1 + \left(\frac{f}{7.4}\right)^4 + \frac{0.013}{f}}$$

$$d_{acc,z} = 3 \times 10^{-11} \sqrt{1 + \left(\frac{f}{0.0.57}\right)^4 + \frac{0.014}{f}}$$

In practice, these errors are mapped on to the simulated range-rate data by applying a transfer function from the perturbed satellite motion [Loomis et al., 2012; Kim, 2000]. The ASD of the attitude error is given in the pitch and roll axes as 2.1×10^{-5} $\text{rad}/\sqrt{\text{Hz}}$ and in the yaw axis as 1.7×10^{-4} $\text{rad}/\sqrt{\text{Hz}}$. Properly simulating the low-degree GRACE errors remains a challenge since they come from different sources (e.g., orbit configuration, single accelerometer). The degraded estimate of $C_{2,0}$ from GRACE is due in part to thermal effects related to the satellites' beta-prime angle [Cheng and Ries, 2017]. These manifest in the observation data as sinusoidal tone-errors at multiples of the orbit frequency [Pfaffenzeller et al., 2022; Kornfeld et al., 2019]. A tone-error with an amplitude of 100 μm and a frequency of 2 cycles-per-revolution (cpr) is therefore included in the GRACE simulation on the range-rate data as it was found that this sufficiently degrades the

GRACE $C_{2,0}$ estimate. The ASD of the accelerometer and ranging instrument errors is shown in Figure 6.1 in terms of range-rate. The accelerometer error dominates at low frequencies, while the ranging instrument noise dominates at higher frequencies. Figure 6.2 shows the GRACE error degree amplitudes for the 12-month mean GRACE errors and the truth signal as well as each monthly solution, with the latter showing some variability as the underlying signal evolves and affects recovery in certain regions.

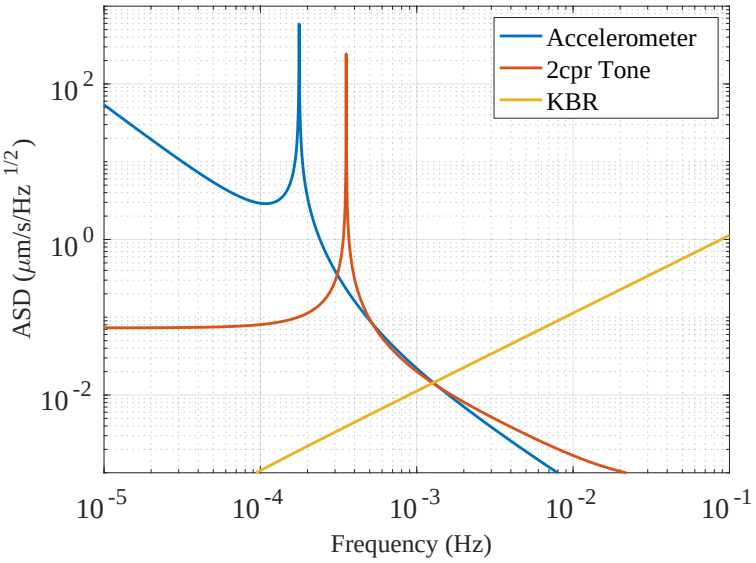

Figure 6.1: ASD of accelerometer, 2cpr tone, and KBR noise in terms of range-rate.

An additional case was run with accelerometer errors defined as the difference between the older ACT and newer ACH data transplant products with the intention of increasing the $C_{3,0}$ error by approximating the accelerometer complications [Ghobadi-Far et al., 2023]. While this case increased the overall GRACE errors as seen in Figure 6.3 (including the $C_{2,0}$ error), $C_{3,0}$ failed to degrade. The GRACE errors in this coefficient have complex underlying causes that are difficult to produce in a simulation [Chris McCullough, personal communication]. Relative to the tone-error case, this transplant-error case mainly affected the near sectoral terms at the mid to high degrees (Figure 6.3). This chapter will therefore examine the full combination solution using the tone-error case, and the topic of simulating GRACE $C_{3,0}$ error is left for future work as the presented case will prove insightful on its own.

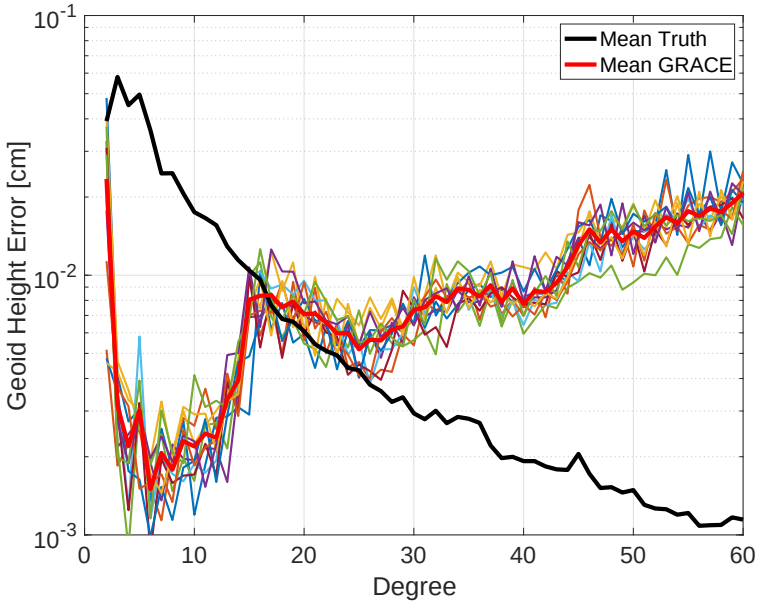

Figure 6.2: Error degree amplitude from GRACE simulation. The thin colored lines are individual months, the red line is the GRACE mean, and the black line is the truth signal mean. No smoothing or destriping has been applied.

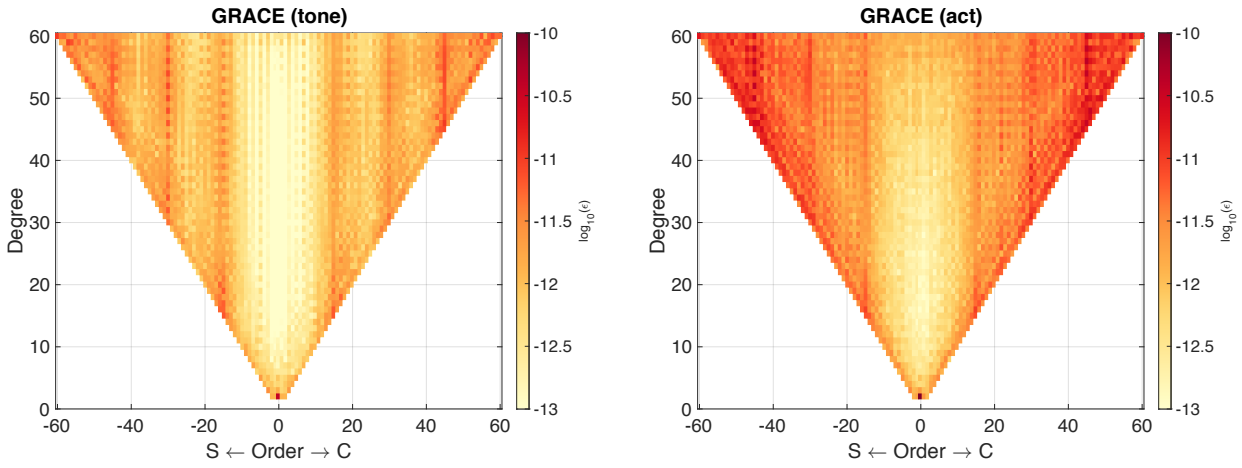

Figure 6.3: Comparison of GRACE errors for tone-error case (left) and accelerometer transplant error case (right).

6.3 Combination Procedures

The *substitution* method is straightforward and the framework has largely been established throughout this thesis. Following the methods in Chapter 3, SLR data are simulated and processed to estimate a set of $5 \times 5 + C_{6,1}/S_{6,1}$ gravity coefficients. A set of GRACE data are also simulated and processed according to Section 6.2 and a set of gravity coefficients is estimated to degree and order 60. The desired SLR-derived coefficients can now be compared with or substituted into the GRACE solution.

The *combination* method requires a more rigorous fusion of data that can be done at the observation level (Eq. 2.23) or at the normal equation level (Eqs. 2.34 and 2.35). The combination solutions presented here are done at the normal equation level. Combinations with the normal equations allow one to work with matrices of a more manageable size– the N matrix is square with dimensions equal to n gravity parameters whereas the H matrix has one dimension equal to the number of observations m. Additionally, arc parameters are pre-reduced (Eq. 2.33), which greatly simplifies the bookkeeping when combining different data types. One drawback to using normal equations is that extreme care must be taken to ensure consistent processing of the different data sets. This is especially true if one analysis center processes the SLR data and another the GRACE data. However, combining data at the normal equation level can facilitate the sharing of data between centers if the processing is done correctly.

Once the normal equations from each technique have been formed, there still remain some design choices prior to the final inversion. The first is the size of the SLR gravity expansion to combine with GRACE. An SLR-only solution to degree and order 20, for example, is poorly conditioned and the coefficients cannot be meaningfully resolved. Combining 20×20 SLR normal equations with GRACE, however, provides stability that can allow the SLR data to influence the higher degree and non-zonal terms. The size and importance of the SLR expansion will be investigated in the following sections. The other consideration is the relative weighting between the techniques. One can select weights heuristically, using the *a posteriori* variances, or by optimizing

some desired criteria. Since the truth is known in a simulation, one possible weight is the one that minimizes the total geoid degree difference variance such that

$$\underset{\lambda}{\text{argmin}}\ \sigma_N^2 = r_E^2 \sum_{n=2}^{N} \sum_{m=0}^{n} (\Delta C_{nm}^2 + \Delta S_{nm}^2) \tag{6.1}$$

where the relative weight λ is contained implicitly in the estimated Stokes coefficients. To understand the influence of SLR on GRACE, it will be useful to test a range of weighting factors, but Eq. 6.1 provides a useful starting point.

6.4 Design Choices

Although there exists some literature on GRACE and SLR combination solutions, no reviewed sources have investigated and compared the maximum degree of the SLR partials used in the combination. Haberkorn et al. [2016] use 20×20 SLR partials and found the formal errors of the combination most improved for low degree, sectoral, and resonant order terms. Kang et al. [2022] included the full 60×60 partials and show that, depending on GRACE's orbit, the SLR data influence the low-degree zonals and the GRACE resonant orders. It is computationally expensive to generate normal equations of this size as the size of the matrices increase nonlinearly with increasing maximum degree. One must also verify that SLR does not degrade the higher degrees that GRACE better resolves. The simulation environment is used to compare the influence of SLR using partials of size 10×10, 20×20, 40×40, and 60×60. For the relative weighting, Haberkorn et al. [2016] presented 2 cases, one of which had a lower SLR weight and another which had a higher one. They found large differences between the two weightings. This section therefore studies the relative weighting concurrently with the expansion size by testing 3 weights each 10^2 larger than the previous.

Figure 6.4 compares the aforementioned weighting and expansions in terms of the error degree and order amplitudes. The effects of over-weighting the SLR data are clear in the case with the largest weight. As one may expect, nearly all coefficients degrade for this case given GRACE's superior ability to resolve the mid and high degrees. With the intermediate SLR weight, the

10×10 has little impact besides $C_{2,0}$, while the other expansion effect the mid-degrees. These larger expansions improve the near-sectoral resonant orders ($m \approx 15, 30, 45$), although the SLR 40×40 and 60×60 still show signs of over-weighting around degrees 26-30 and order 25. Decreasing the SLR weight further essentially limits its influence to $C_{2,0}$ regardless of the size of the partials used.

Ultimately this analysis suggests that the relative weighting needs to be selected carefully so that the SLR data can influence the low to mid degrees without degrading the higher ones. The 20×20 appears to be the minimum expansion one should use in a combination, but the 60×60 also produces positive results with an appropriate weight. These partials benefit GRACE through improvements to the zonal terms and to the resonant order terms, particularly the near-sectoral ones (i.e. where $m \approx n$). SLR satellites orbit higher than GRACE and contain less useful information about the higher degrees (see also Figure 4.1). Still, there does not appear to be negative effects of using higher degree SLR partials if higher order GRACE resonances ($m = 30, 45, ...$) were of concern and a reasonable weight were selected. Using the full 60×60 SLR partials will further benefit the combination during months when GRACE enters a near-repeat orbit configuration as Kang et al. [2022] observe. Even in the nominal orbit, Figure 6.4 shows GRACE having the largest errors around $C_{2,0}$ and the resonant orders. Thus, if GRACE were in a less favorable orbit, one could reasonably expect the 60×60 SLR partials to have a greater influence at the higher degree coefficients.

6.5 Combination Results

Simulated combination solutions are formed for a 12-month period using the described processing. A series of tests determined an ideal relative weight of SLR to GRACE in the setup to be 8×10^{-13}. Note that the magnitude largely depends on the processing and may vary between analysis centers. Also presented are GRACE-only and SLR-only solutions, where the former estimates the full gravity field to degree and order 60, and the latter only estimates the gravity coefficients to degree and order 5 plus $C_{6,1}$ and $S_{6,1}$ as in Chapters 4 and 5. A bias is removed from all solutions. Figure 6.5 shows a timeseries of $C_{2,0}$. The GRACE estimate of $C_{2,0}$ appears noisy with large jumps

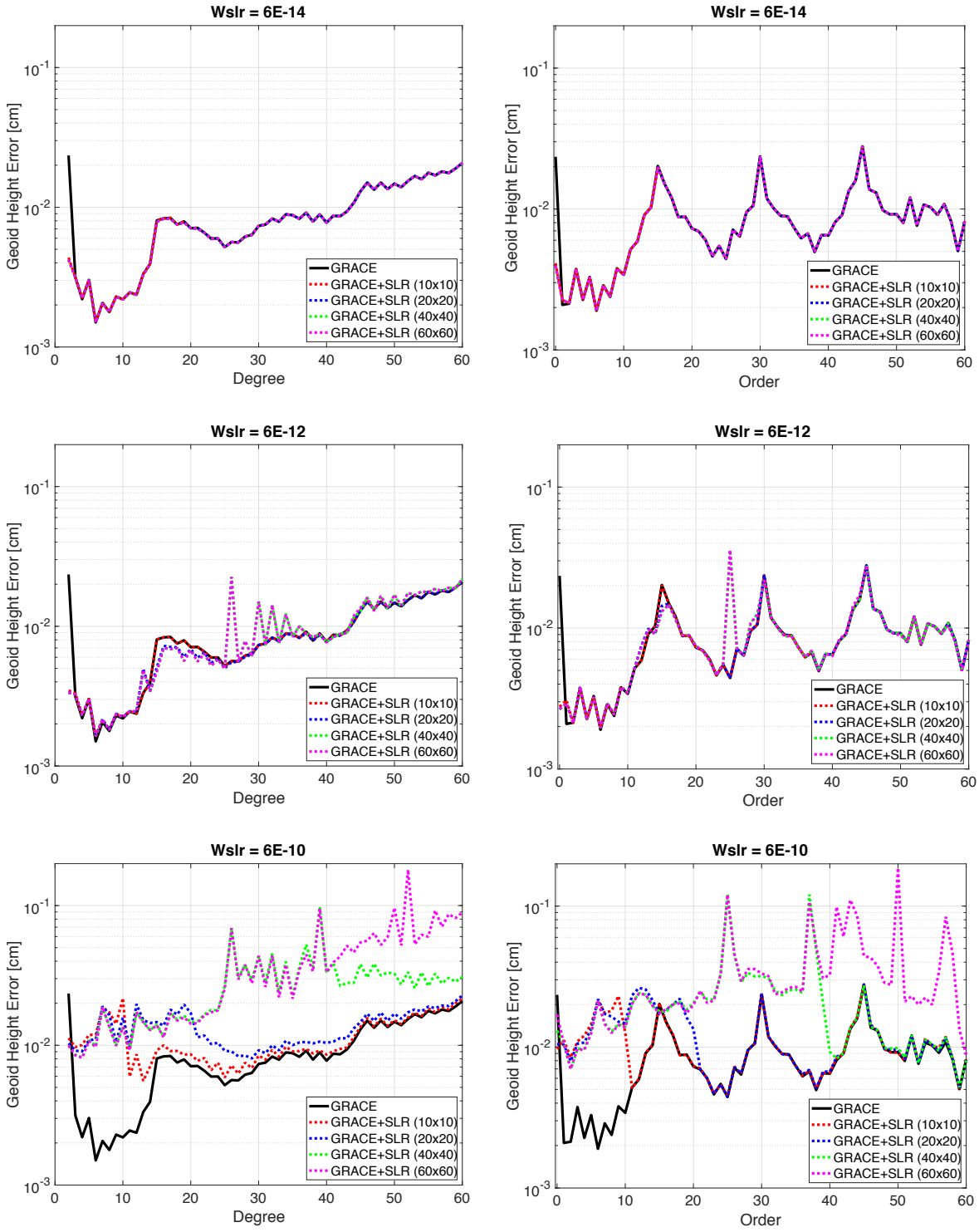

Figure 6.4: Geoid error degree (left column) and order (right column) amplitude for 3 row-wise SLR data weights and 4 SLR expansions: 10×10 (red), 20×20 (blue), 40×40 (green), and 60×60 (magenta). GRACE-only is shown in black.

between months as one may expect. SLR independently recovers this coefficient much better than GRACE, although it overestimates the annual amplitude relative to the truth. Upon combining the GRACE and SLR data at the normal equation level and jointly inverting for a single solution, one can observe a remarkable improvement in the recovered $C_{2,0}$ coefficient. An insightful way to quantify this improvement is to simply compute the RMS of the difference between an estimate and the truth as done in Chapter 4. The GRACE-only solution has an RMS difference of 4.3×10^{-11}. The SLR-only solution is over 50% better, with an RMS difference of 2.0×10^{-11}. The combination has the lowest RMS difference at 3.1×10^{-12}, showing an improvement of about an order of magnitude with respect to the independent solutions.

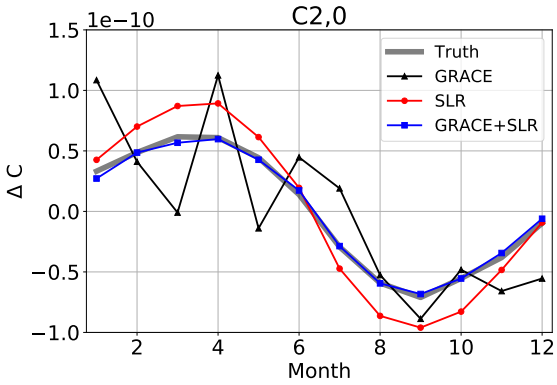

Figure 6.5: Simulation results for timeseries of $C_{2,0}$.

For a particular orbit, certain gravity coefficients can induce resonant effects that amplify variations in some orbital elements [Kaula, 1966]. With GRACE's orbit, the resonant coefficients are of order $m \approx 15$ and its integer multiples [Cheng and Ries, 2017]. The effects of resonance vary in strength over the mission lifetime as the orbit evolves and are particularly strong when the satellite enters a short repeat-cycle (e.g., 61 revolutions to repeat in 4 days). While this GRACE simulation considers only a nominal orbit (i.e. not exactly or deeply resonant), the errors in the resonant orders tend to be elevated compared to other coefficients. Figure 6.6 shows timeseries for the $C_{15,15}$ and $S_{15,15}$ coefficients, respectively. The general sawtooth nature of the GRACE-only estimates demonstrates the poor recovery of the coefficients. The combination solution leads

to a small but systematic improvement for these coefficients. For $C_{15,15}$ the RMS difference of the combination is 5.0×10^{-12} compared to 7.2×10^{-12} for GRACE-only. Likewise, the $S_{15,15}$ coefficient improves to an RMS of 5.4×10^{-12} in the combination compared to 7.8×10^{-12} in the GRACE-only solution. This reveals SLR's ability to impact GRACE beyond $C_{2,0}$, even in months where GRACE is in a nominal orbit. Although errors remain in these coefficients, the simulation environment uniquely confirms that these terms do benefit from the combination, and the level of improvement agrees well with the differences in Kang et al. [2022, cf. Figure 3].

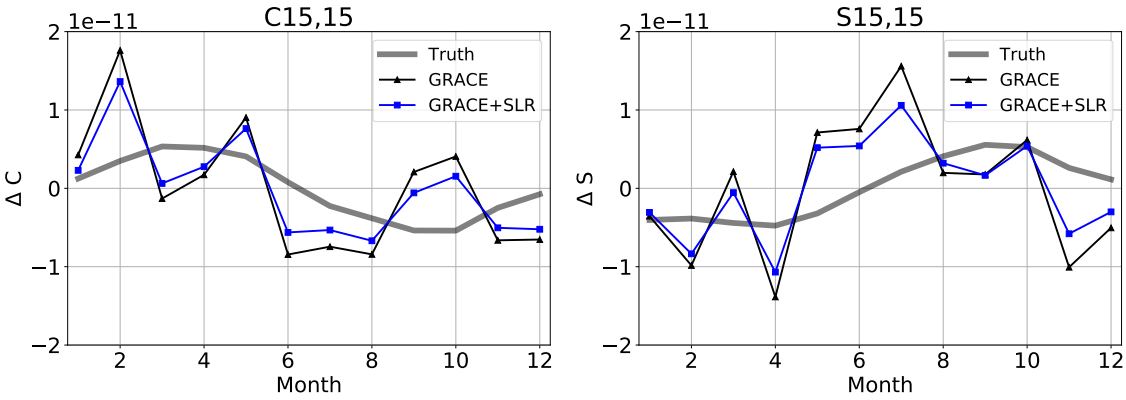

Figure 6.6: Simulation results for timeseries of $C_{15,15}$ and $S_{15,15}$

Turning to a more global perspective, the error degree and order amplitudes are computed in terms of geoid height. Figure 6.7 shows these quantities for the GRACE-only and combination solutions. The GRACE data most influence the solution as one would expect given its superior resolution to SLR. The largest low-degree error in GRACE comes from $C_{2,0}$, which is recovered significantly worse than other coefficients as a consequence of the simulation setup. The SLR data also noticeably influence the solution around degrees 15-20. Looking at the order-wise plot, there are 4 areas of large errors in the GRACE-only solution: order 0 and 3 spikes corresponding to the resonant orders. The combination has some improvement around $m = 15$ indicating that SLR is sensitive to these terms. An increase in the errors at degree 26, order 25 shows that the combination degrades this coefficient, but the signal and overall errors in this term are quite small in an absolute sense.

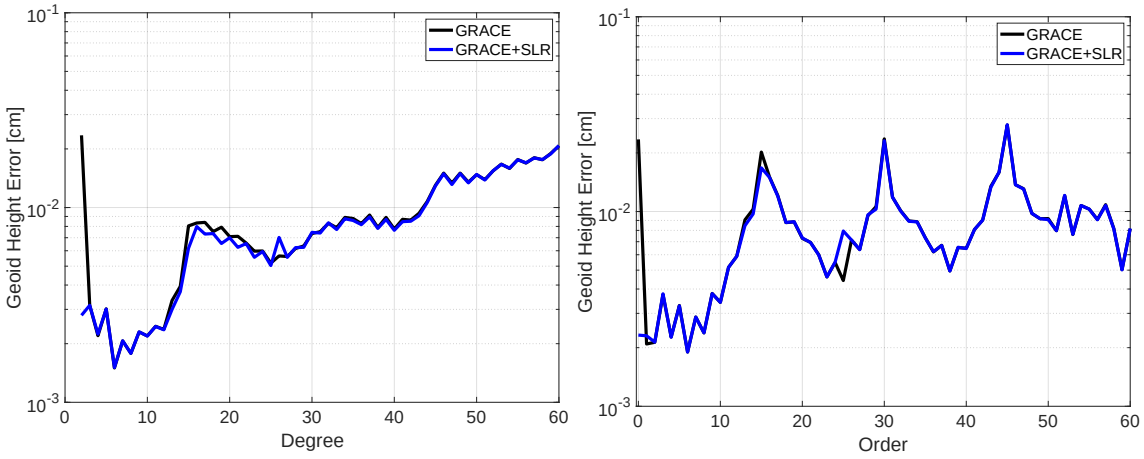

Figure 6.7: 12-month mean (a) error degree amplitude and (b) error order amplitude expressed in centimeters of geoid.

To examine the results spatially, the results are synthesized into global maps of equivalent water height (EWH) in Figure 6.8, which shows maps for the first 6 monthly solutions [Swenson and Wahr, 2002]. Figure 6.9 reports the remaining months. Having established the large improvement in $C_{2,0}$ with the combination, these maps exclude this coefficient here to focus on SLR's secondary contributions. Additional processing includes truncation of the expansion at degree and order 40 to suppress GRACE's characteristic striping and application of a 500 km Gaussian smoothing. Figure 6.8 further reports the area-weighted RMS of the maps to quantify the global errors. Despite monthly variability in the truth signal, the combination solution generally shows an improvement over the GRACE-only solution. In some months the combination has a lesser impact, such as the first month where the RMS decreases from the GRACE-only 0.78 cm EWH to 0.77 cm EWH with the combination. In other months the SLR data have a much larger effect. The RMS improves about 9% for months 2, 4, and 6. The remaining months 7 through 12 follow a similar pattern (Figure 6.9), with some combination solutions giving improvements of 10%. While the SLR data do not necessarily change the spatial structure of the errors, they do have a notable impact on the magnitudes of these errors. Recall also that the $C_{2,0}$ contribution is omitted here, which has the most substantial impact (Figure 6.5).

Assessing the solutions regionally can provide a more physically meaningful quantification of the impact of the combination solution. To do this, averaging kernels were formed for the polar ice sheets, global ocean, and 9 major river basins (Figure 6.10) following commonly used methods [Swenson and Wahr, 2002]. For Greenland, Antarctica, and the global ocean, a 300 km coastal buffer is used. In all regions, the solution is computed to degree and order 60 with 300 km Gaussian smoothing applied. Figures 6.11 and 6.12 report the timeseries of results for each basin with and without the $C_{2,0}$ contribution, respectively. Table 6.1 quantifies these basin-level errors as the RMS of the difference with respect to the truth for GRACE and the combination. Comparing Figures 6.11 and 6.12 confirms that the GRACE-only $C_{2,0}$ dominates the error in most regions. Given that $C_{2,0}$ physically describes Earth's oblateness, this effect is most apparent in the ice sheets. The combination solution reduces the RMS error (with $C_{2,0}$ considered) by a factor of about 10

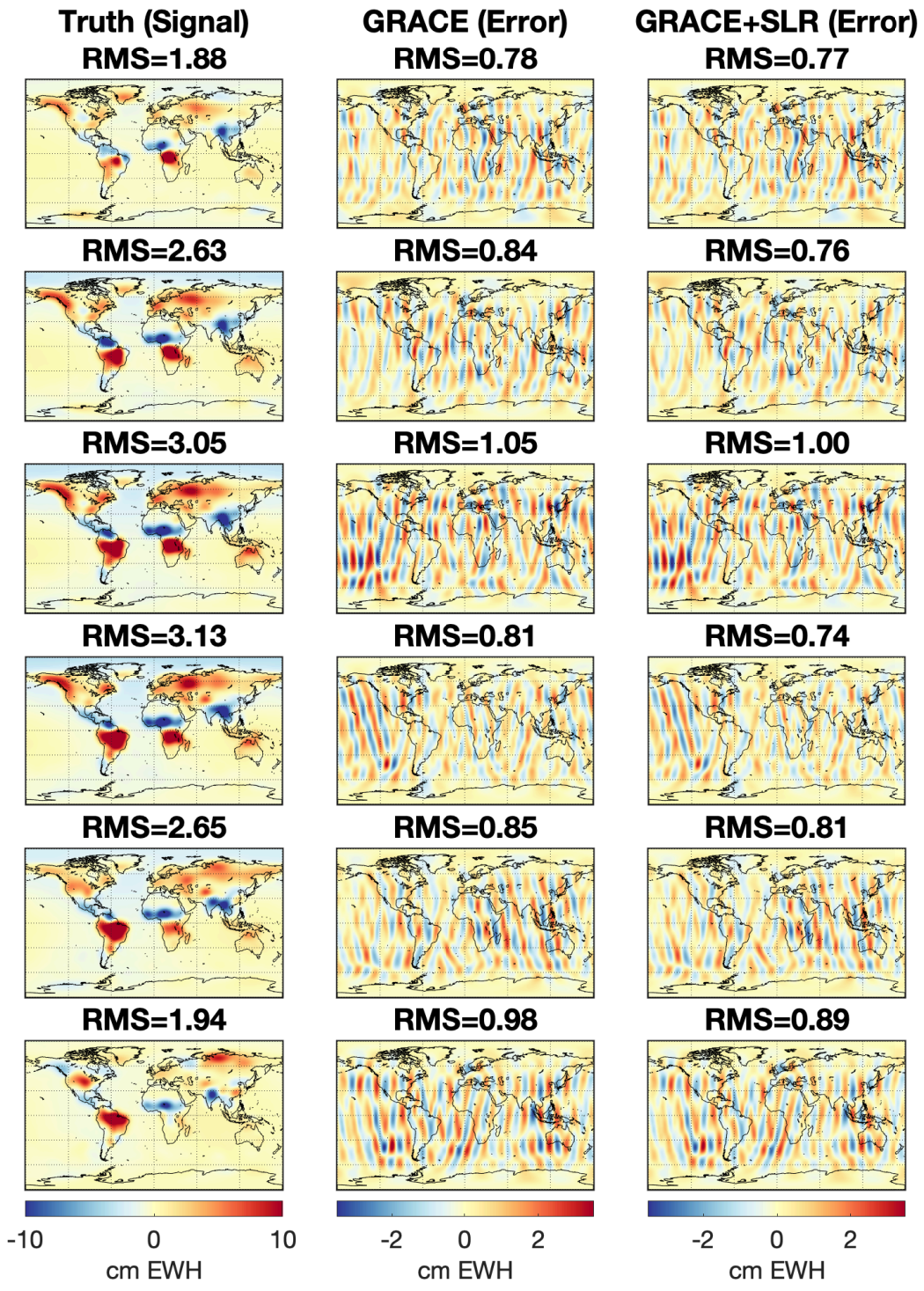

Figure 6.8: Spatial maps of TVG signal and errors for solution months 1-6 row-wise. Column 1 is the truth signal, column 2 is the GRACE error, and column 3 is the combination error. Solutions are computed without the $C_{2,0}$ contribution to degree and order 40 with 500 km Gaussian smoothing. Units are cm equivalent water height (EWH).

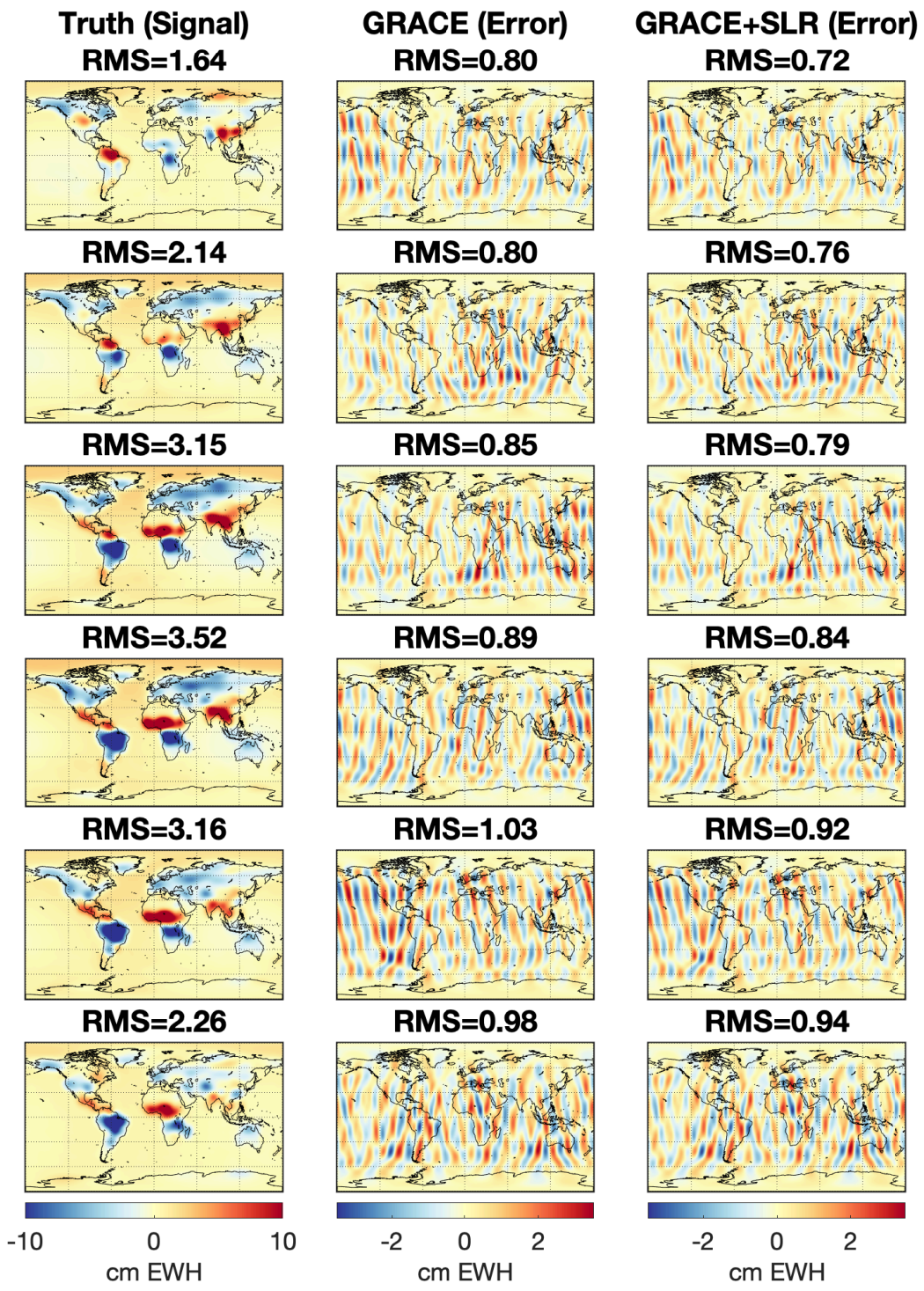

Figure 6.9: Same as Figure 6.8 for months 7-12.

and 5 in Antarctica and Greenland, respectively. Every other basin, except the Ob river, shows some level of improvement with the magnitude depending on the regional errors. Removing the $C_{2,0}$ contribution greatly reduces the impact of the combination. Nevertheless, the combination still moderately reduces the error in some basins such as the Ganges-Brahmaputra, Mackenzie, Yenisey, and Lena rivers on the order of 5-6%.

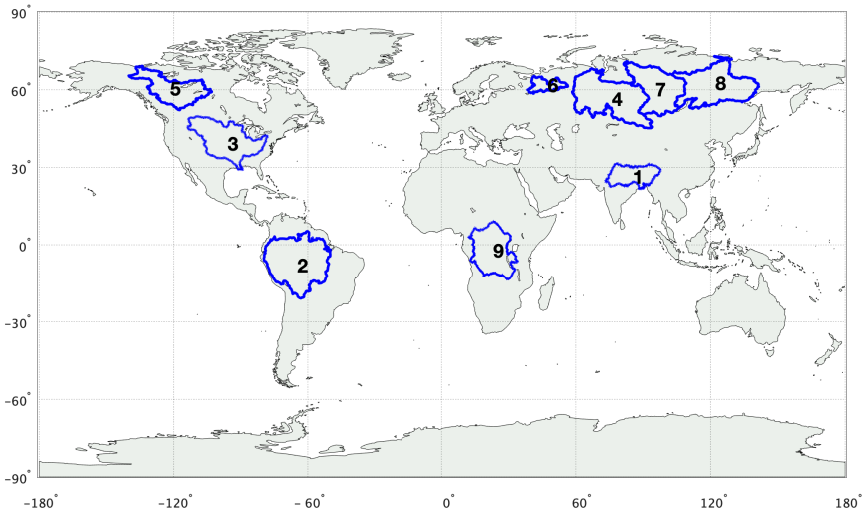

Figure 6.10: Map of select river basins. See Table 6.1 for names of numbered basins.

The results have shown the benefits to using a combination solution, even when GRACE is in a favorable orbit. On its own, SLR can only resolve the first few degrees of the gravity field; attempts to invert for more coefficients quickly result in high parameter correlations and ill-conditioned normal equations. This is due to the fact that SLR determines the gravity field through non-unique orbit perturbations, thus requiring a variety of satellites at different inclinations and altitudes to accurately resolve certain coefficients as seen in Chapter 4 and as observed in the literature [Cheng and Ries, 2017; Sośnica et al., 2015]. With the introduction of GRACE information in the combination, the correlations are reduced in the SLR data allowing for better separation of key parameters. The correlation between $C_{2,0}$ and $C_{4,0}$, for example, improves from about -0.6 in the baseline SLR-only solution to -0.15 in the combination solution. Note that this value is somewhat sensitive to the data weights as over-weighting the SLR data drives the

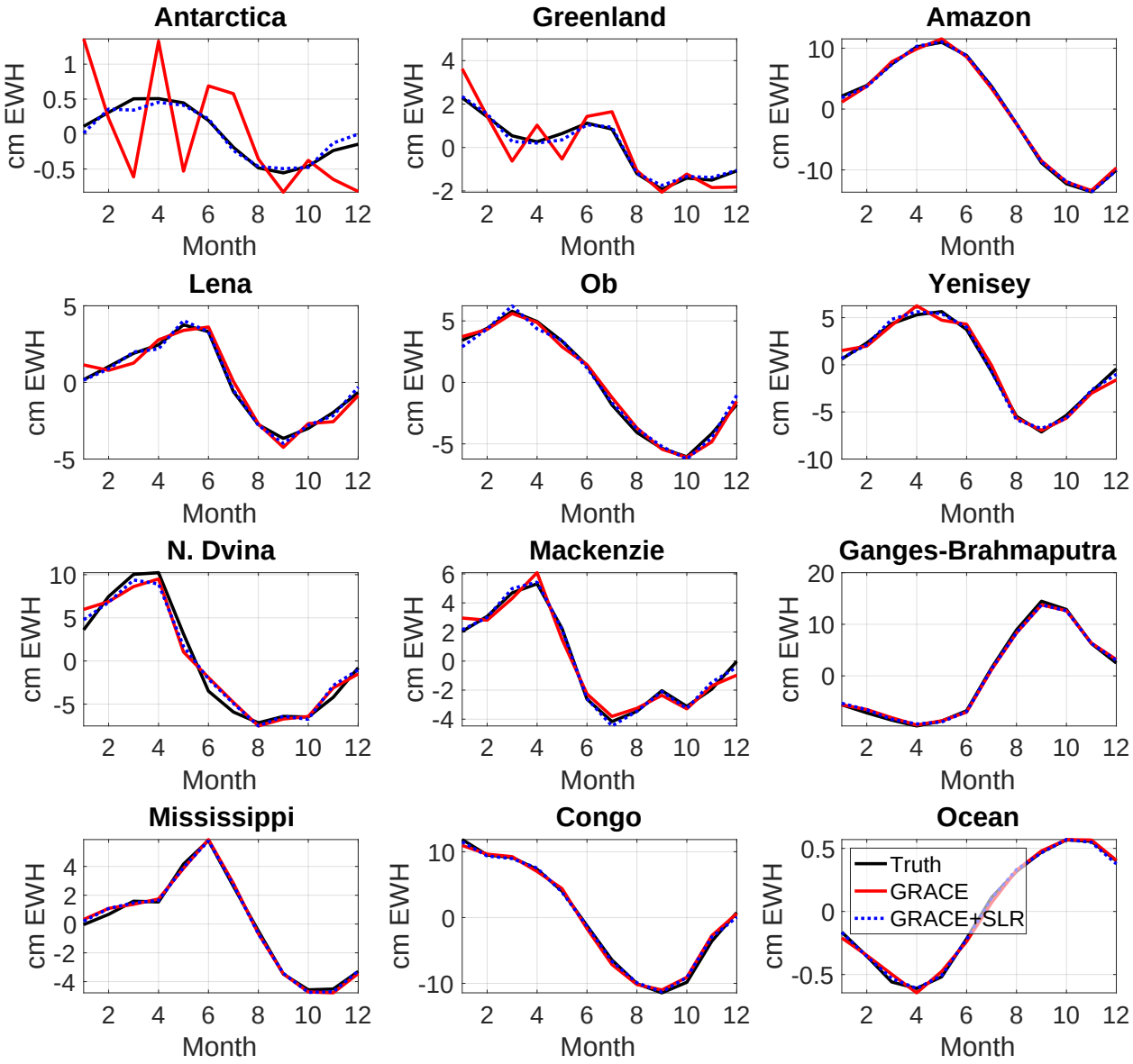

Figure 6.11: Mass change in select basins for truth (black), GRACE (red), and GRACE+SLR7 (blue dash). Solutions are computed to degree and order 60 with 300 km Gaussian smoothing.

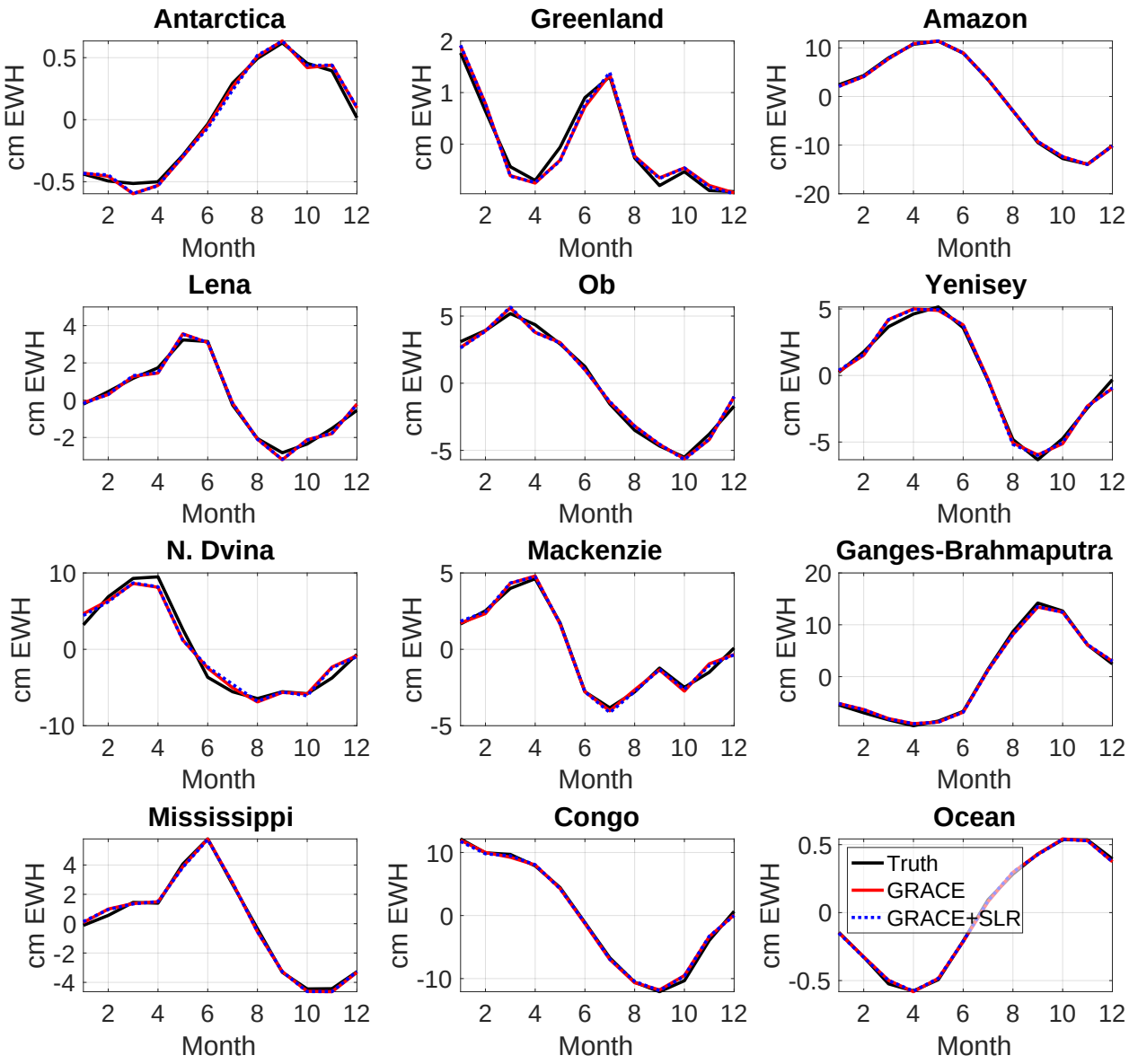

Figure 6.12: Same as Figure 6.11 but without the $C_{2,0}$ contribution.

Table 6.1: Error RMS for selected geographic areas computed with and without $C_{2,0}$ contribution. Basin number refers to Figure 6.10.

Basin (number)	**With $C_{2,0}$** (cm EWH)		**Without $C_{2,0}$** (cm EWH)	
	GRACE	GRACE+SLR7	GRACE	GRACE+SLR7
Antarctica (-)	0.708	0.082	0.041	0.045
Greenland (-)	0.740	0.143	0.131	0.129
Amazon (2)	0.415	0.159	0.176	0.169
Lena (8)	0.500	0.206	0.227	0.213
Ob (4)	0.340	0.377	0.359	0.372
Yenisey (7)	0.645	0.313	0.345	0.322
N. Dvina (6)	1.242	0.960	0.936	0.950
Mackenzie (5)	0.547	0.229	0.258	0.240
Ganges-Brahmaputra (1)	0.430	0.390	0.402	0.388
Mississippi (3)	0.238	0.185	0.181	0.186
Congo (9)	0.519	0.381	0.387	0.387
Ocean (-)	0.031	0.012	0.012	0.011

correlations in the combination to their SLR-only values. The recent use of GRACE-derived forward models in SLR data processing by Loomis et al. [2019] and Cheng and Ries [2023] provides a similar benefit insofar as the *a priori* data mitigate the impact of the correlated parameters, though the actual value of the correlations remains unaffected. This processing advancement has led to major improvements in SLR gravity solutions of $C_{2,0}$ and $C_{3,0}$, but does not fully exploit SLR's capability to supplement GRACE. The combination method delivers a unified and mathematically rigorous joint solution.

6.6 Reconciling Combinations with New Satellites & Stations

The combination of GRACE with the SLR7 produced a highly accurate estimate of $C_{2,0}$ and leaves little room for a new satellite or station to improve the low-degree solution further. Here, it is stressed that the combination solutions serve a different purpose than the addition of a new satellite or station investigated in Chapters 4 and 5. New additions to the SLR system would mainly benefit independent SLR solutions. Even with the superior resolution of the GRACE data, independent SLR solutions are useful for validating GRACE, especially during months where its orbit is sub-

optimal or during end-of-life operations with lower power usage. Perhaps even more salient are the points discussed in Section 1.3.2 regarding the continuity of mass-change observations. Gaps in the GRACE record present challenges in assessing possible biases, especially if large mass-change events were to occur. Enhancing the SLR-only record adds critical redundancy and can mitigate the impact of future gaps in the GRACE timeseries. With GRACE data available, however, there are seemingly few drawbacks to forming combination solutions. As discussed in Section 6.5, the GRACE and SLR data are in some ways complementary; SLR is sensitive to linear combinations of low-degree coefficients, which GRACE does not recover as well, and the GRACE data maximizes the information in the SLR observations. Although there were challenges in simulating the GRACE low-degree errors, the behavior of $C_{2,0}$ demonstrates the benefits of combination solutions. Compared to independent estimates, the combination decreases the impact of correlated parameters and reduces the chance of higher degree effects aliasing into the lower degrees in the SLR data. Combination solutions and new SLR additions therefore play simultaneously important roles in maintaining accurate TVG estimates.

6.7 Conclusions

This chapter investigated fully-simulated combination solutions of GRACE and SLR data. The different data types are combined at the normal equation level and inverted to produce a single solution in contrast to the conventional substitution method that forms two independent solutions. Several cases using different relative weighting and normal matrix sizes were studied. It was found that the SLR partials up to degree and order 60 could be used so long as these data are not overweighted relative to GRACE. With the inclusion of a twice-per-rev tone error, the simulated GRACE solution had the largest errors in the $C_{2,0}$ coefficient, which also showed the most significant improvements after performing the combination. Even though SLR can recover this term on its own, the GRACE data reduce the influence of higher degrees, leading the combined solution to produce a highly accurate estimate of this coefficient. Compared to GRACE on its own, the combination also improved the near-sectoral coefficients of order 15, which are the primary

resonance terms with GRACE's orbit. Practically, this translated to small, but still significant improvements in recovering the global signal spatially, with the monthly errors reduced up to 10% when the $C_{2,0}$ contribution was excluded. Regionally, the ice sheets and large river basins also improved with the combination. The full combination reduced the error RMS in the ice sheets by a factor of 5-10. Depending on the regional errors, certain river basins improved over 50% with the full solution and up to 6% with $C_{2,0}$ excluded. These results provide a novel quantification of the combination's impact. Given that SLR satellites have decadal lifespans in highly stable orbits, they are a natural choice to continue supplementing the GRACE data.

Chapter 7

Conclusions

This thesis has presented a comprehensive analysis of potential improvements to SLR TVG estimates through new additions to the space segment, ground network, and combination solutions with GRACE. This chapter presents a summary of the results, recommendations for the future of SLR, and suggestions for future studies.

7.1 Summary

For new additions to the SLR system (stations and satellites), the results ultimately suggest that a new satellite would have the largest impact on temporal gravity estimates. It was found that a low-inclination satellite provided the most improvement when combined with 7 existing SLR satellites. Such a satellite strongly decorrelated the low-degree gravity coefficients, particularly the even zonals whose correlation improved by an order of magnitude. Multi-year simulations demonstrated that this led to improved recovery of the annual signal and a significant reduction of the retrieval errors in these coefficients. Synthesizing the solution in terms of equivalent water height also revealed notable improvements with a new low-inclination SLR satellite. To explain these results, a sensitivity analysis was performed to study the effect of higher degree influences on the solution. This showed that the low-inclination satellite very effectively reduces the influence of the higher degree even zonals, allowing for improved recovery of the estimated terms. The errors in the odd zonals also reduce, albeit to a lesser extent due to the effect of LARES in the baseline solution. Overall, the altitude of a potential new satellite was found to be less impactful than its

inclination, so long as the altitude is high enough to allow for a sufficient number of observations. Finally, aspects of analytical perturbation theory were used to verify the interplay of altitude and inclination. While a satellite's sensitivity to the gravity field decreases with increasing altitude, this effect primarily dominates at shorter wavelengths. For a given altitude, the inclination primarily affects a satellite's sensitivity to the zonal coefficients, with the analytical equations confirming the large impact of a low-inclination satellite.

While new stations did not have the dramatic effect of a new satellite, they will continue to play an essential role in the observing system. Three cases were studied: a single new station, 5 future stations, and a geographically uniform case. The case of a single new station revealed key patterns regarding the placement of a new station and its effect on the low-degree gravity coefficients. However, the analysis was restricted to the formal errors since a new station is only 2-3% of the total network. The results showed that a new station could decrease the formal errors of certain coefficients by over 10%, particularly if the station fills a geographic gap at the poles or in the Southern hemisphere. The odd zonals would especially benefit from an Antarctic station as their errors reduced by over 10% with the addition of such as station. Several other sectoral and tesseral coefficients also saw improvements of this magnitude with the addition of this simulated station. Although no Antarctic station is under construction, there are new stations scheduled to begin operations in the coming decade. An investigation of 5 potential new stations found that they could increase the network's sensitivity to TVG at least to the level of a single Antarctic station, even if their location is not strictly optimal. This case improved the formal errors in the zonals, tesserals, and sectorals by 11%, 13%, and 15%, respectively. A non-realistic, but nonetheless informative, scenario was studied where the tracking stations were distributed evenly across the globe. Although this led to large improvements in the formal errors and retrieval error, the correlations of the zonals and order 1 terms remained unaffected. This suggests an important fundamental limitation of ground stations to systematically decorrelate certain gravity coefficients as with a new satellite. Through analytical perturbation theory, one finds that the SLR satellite orbits drive the observed correlations in the SLR solution due to the fact that each satellite senses

non-unique effects from a linear combination of coefficients. Notwithstanding this key distinction, new stations remain essential for redundancy and for increasing the overall number of data points.

Finally, this work investigated fully-simulated combination solutions that merged GRACE and SLR data to form a single solution. Several design choices were considered, with the relative data weighting found to be the most consequential choice. The $C_{2,0}$ coefficient improved the most, with the error RMS in the combined solution reduced by about an order of magnitude relative to the independent methods. The sectoral coefficients of GRACE's primary resonant order ($C_{15,15}$ and $S_{15,15}$) saw their error RMS reduced by 30% in the combination. Even with the large $C_{2,0}$ contribution removed, globally averaged errors reduced in certain months by 10% or over 0.1 cm EWH compared to GRACE-only. $C_{2,0}$ has a large effect on the estimated mass change of the ice-sheets; the combination improved Antarctic and Greenland mass recovery by a factor of 10 and 5, respectively. Removing the large impact of this coefficient, the combination solution still shows reduced errors in certain large river basins of about 5%.

7.2 Recommendations & Future Work

Launching a low-inclination SLR satellite with the purpose of measuring TVG would provide a unique data set that would benefit numerous scientific communities. Although SLR independently cannot replace GRACE in terms of data resolution, it can serve as a low cost method for validating GRACE, filling inter-mission gaps (especially with new SLR additions), and producing a long term timeseries of the low-degree gravity terms and reference frame parameters. The passive, low cost nature of an SLR satellite makes it a particularly attractive option to enhance the low-degree gravity field, and their decadal lifespan ensures continuous data, barring any anomalous failures. While no detailed budgets could be located, one source[1] quotes the LARES satellite as costing about USD 10 million, excluding launch costs. This is substantially lower than the estimated NASA contribution[2] of over USD 400 million for GRACE-FO. While SLR has a more involved ground segment than

[1] https://www.nationalgeographic.com/science/article/120213-einstein-relativity-european-space-agency-vega-rocket-science

[2] https://www.jpl.nasa.gov/news/press_kits/grace-fo/download/grace-fo_launch_press_kit.pdf

GRACE, these stations will continue to operate regardless of the addition of a new satellite and therefore no significant cost burden is incurred for this component. Thus, a new SLR satellite could provide significant science return relative to its cost.

The prospect of an Antarctic station should continue to be explored. The practical aspects of an Antarctic station discussed in Section 5.5 should be further investigated. The two forthcoming South American stations are a promising start to filling geographic gaps, although these stations are replacing and upgrading previous ones. Constructing any new station requires years of careful planning and simply calling for the development of new stations understates the difficulty of this task. New Southern hemisphere stations present a particular challenge due to climate, geopolitical factors, and there being less land mass overall. Technological advancements may permit SLR to occur in previously overlooked areas. One way to diversify the network is with small, low-cost stations, such as the "miniSLR" [Hampf et al., 2023].

New satellites or stations have the largest impact on independent SLR solutions. Given the current SLR satellites, the simulation suggests that a combination solution with GRACE produces highly accurate estimates of the low-degree gravity field. It is therefore recommended that combination solutions become a more regular product. This will ensure a high quality solution that fully leverages the gravity information contained in the SLR data. It also preserves the statistical characteristics that the substitution method neglects, which could allow for more rigorous error analyses.

This thesis has laid the foundation for several potential future studies. The effect of new satellites and new stations on the reference frame and EOPs should be investigated, with some literature having already examined new stations. The case for a low-inclination satellite would be strengthened if its impact on these fundamental geodetic parameters were quantified. The effect of a new satellite on geocenter estimation would also make for a useful study with careful consideration as to the method of computing this quantity. Additional cases involving new satellites should continue to be examined, including cases involving multiple new satellites and with varied eccentricity. Finally, more combination strategies should be explored, such as those that employ

regularization or use a basis other than spherical harmonics. These proposed investigations, while not a comprehensive list, would complement and expand upon the results in this dissertation.

Bibliography

Bandikova, T., McCullough, C., Kruizinga, G. L., Save, H., and Christophe, B. (2019). GRACE accelerometer data transplant. Advances in Space Research, 64(3):623–644.

Bloßfeld, M. (2015). The Key Role of Satellite Laser Ranging towards the Integrated Estimation of Geometry, Rotation and Gravitational Field of the Earth. PhD thesis, Technische Universität München.

Bloßfeld, M., Müller, H., Gerstl, M., Stefka, V., Bouman, J., Göttl, F., and Horwath, M. (2015). Second-degree Stokes coefficients from multi-satellite SLR. Journal of Geodesy, 89(9):857–871.

Bloßfeld, M., Rudenko, S., Kehm, A., Panafidina, N., Müller, H., Angermann, D., Hugentobler, U., and Seitz, M. (2018). Consistent estimation of geodetic parameters from SLR satellite constellation measurements. Journal of Geodesy, 92(9):1003–1021.

Bonin, J. A., Chambers, D. P., and Cheng, M. (2018). Using satellite laser ranging to measure ice mass change in Greenland and Antarctica. The Cryosphere, 12(1):71–79.

Breivik, G. M., Klingan, O. J., and Grinde, G. (2022). Ny-Ålesund: New SLR Site in the Arctic at 79°N. 22nd International Workshop on Laser Ranging, Yebes, Spain.

Chen, J., Cazenave, A., Dahle, C., Llovel, W., Panet, I., Pfeffer, J., and Moreira, L. (2022). Applications and Challenges of GRACE and GRACE Follow-On Satellite Gravimetry. Surveys in Geophysics, 43(1):305–345.

Chen, J., Tapley, B., Wilson, C., Cazenave, A., Seo, K.-W., and Kim, J.-S. (2020). Global Ocean Mass Change From GRACE and GRACE Follow-On and Altimeter and Argo Measurements. Geophysical Research Letters, 47(22):e2020GL090656.

Chen, J. L., Rodell, M., Wilson, C. R., and Famiglietti, J. S. (2005). Low degree spherical harmonic influences on Gravity Recovery and Climate Experiment (GRACE) water storage estimates. Geophysical Research Letters, 32(14).

Chen, J. L., Wilson, C. R., and Seo, K.-W. (2009). S2 tide aliasing in GRACE time-variable gravity solutions. Journal of Geodesy, 83(7):679–687.

Cheng, M. (1988). Time Variations in the Earth's Gravity Field from Starlette Orbit Analysis. PhD thesis, The University of Texas at Austin, United States – Texas.

Cheng, M. and Ries, J. (2017). The unexpected signal in GRACE estimates of C_{20}. Journal of Geodesy, 91(8):897–914.

Cheng, M. and Ries, J. (2023). C20 and C30 Variations From SLR for GRACE/GRACE-FO Science Applications. Journal of Geophysical Research: Solid Earth, 128(2):e2022JB025459.

Cheng, M., Ries, J. C., and Tapley, B. D. (2011). Variations of the Earth's figure axis from satellite laser ranging and GRACE. Journal of Geophysical Research: Solid Earth, 116(B1).

Cheng, M., Tapley, B. D., and Ries, J. C. (2013a). Deceleration in the Earth's oblateness. Journal of Geophysical Research: Solid Earth, 118(2):740–747.

Cheng, M. K., Eanes, R. J., Shum, C. K., Schutz, B. E., and Tapley, B. D. (1989). Temporal variations in low degree zonal harmonics from Starlette orbit analysis. Geophysical Research Letters, 16(5):393–396.

Cheng, M. K., Ries, J. C., and Tapley, B. D. (2013b). Geocenter Variations from Analysis of SLR Data. In Reference Frames for Applications in Geosciences, International Association of Geodesy Symposia, pages 19–25, Berlin, Heidelberg. Springer.

Cheng, M. K., Shum, C. K., and Tapley, B. D. (1997). Determination of long-term changes in the Earth's gravity field from satellite laser ranging observations. Journal of Geophysical Research: Solid Earth, 102(B10):22377–22390.

Ciufolini, I., Paolozzi, A., Pavlis, E., Ries, J., Gurzadyan, V., Koenig, R., Matzner, R., Penrose, R., and Sindoni, G. (2012). Testing General Relativity and gravitational physics using the LARES satellite. The European Physical Journal Plus, 127(11):133.

Deccia, C. M. A., Wiese, D. N., and Nerem, R. S. (2022). Using a Multiobjective Genetic Algorithm to Design Satellite Constellations for Recovering Earth System Mass Change. Remote Sensing, 14(14):3340.

Degnan, J. J. (1985). Satellite Laser Ranging: Current Status and Future Prospects. IEEE Transactions on Geoscience and Remote Sensing, GE-23(4):398–413.

Dobslaw, H., Bergmann-Wolf, I., Dill, R., Forootan, E., Klemann, V., Kusche, J., and Sasgen, I. (2015). The updated ESA Earth System Model for future gravity mission simulation studies. Journal of Geodesy, 89(5):505–513.

Dobslaw, H., Bergmann-Wolf, I., Dill, R., Poropat, L., Thomas, M., Dahle, C., Esselborn, S., König, R., and Flechtner, F. (2017). A new high-resolution model of non-tidal atmosphere and ocean mass variability for de-aliasing of satellite gravity observations: AOD1B RL06. Geophysical Journal International, 211(1):263–269.

Dobslaw, H., Bergmann-Wolf, I., Forootan, E., Dahle, C., Mayer-Gürr, T., Kusche, J., and Flechtner, F. (2016). Modeling of present-day atmosphere and ocean non-tidal de-aliasing errors for future gravity mission simulations. Journal of Geodesy, 90(5):423–436.

Dong, D., Gross, R. S., and Dickey, J. O. (1996). Seasonal variations of the Earth's gravitational field: An analysis of atmospheric pressure, ocean tidal, and surface water excitation. Geophysical Research Letters, 23(7):725–728.

Ghobadi-Far, K., Werth, S., Shirzaei, M., Loomis, B. D., Döhne, T., Willen, M. O., and Horwath, M. (2023). The Impact of New Accelerometer Transplant Data (ACH) on GRACE Follow-On Along-Orbit Inter-Satellite Laser Ranging Observations and Monthly Time-Variable Gravity and Mascon Solutions. Journal of Geophysical Research: Solid Earth, 128(6):e2023JB026740.

Glaser, S., König, R., Neumayer, K. H., Balidakis, K., and Schuh, H. (2019). Future SLR station networks in the framework of simulated multi-technique terrestrial reference frames. Journal of Geodesy, 93(11):2275–2291.

Haberkorn, C., Bloßfeld, M., Bouman, J., Fuchs, M., and Schmidt, M. (2016). Towards a Consistent Estimation of the Earth's Gravity Field by Combining Normal Equation Matrices from GRACE and SLR. In IAG 150 Years, International Association of Geodesy Symposia, pages 375–381, Cham. Springer International Publishing.

Hampf, D., Niebler, F., Meyer, T., and Riede, W. (2023). The miniSLR: A low-budget, high-performance satellite laser ranging ground station.

Han, S.-C., Shum, C. K., Bevis, M., Ji, C., and Kuo, C.-Y. (2006). Crustal Dilatation Observed by GRACE After the 2004 Sumatra-Andaman Earthquake. Science, 313(5787):658–662.

Hauk, M. and Wiese, D. N. (2020). New Methods for Linking Science Objectives to Remote Sensing Observations: A Concept Study Using Single- and Dual-Pair Satellite Gravimetry Architectures. Earth and Space Science, 7(3):e2019EA000922.

Horvath, J., McGarry, J., Cheek, J., Clarke, C., Donovan, H., Patterson, D., Ricklefs, R., Nelson, A., Hall, F., and Mann, A. (2014). Automating NASA's Space Geodesy Satellite Laser Ranging (SGSLR) system. In 19th International Workshop on Laser Ranging, Annapolis, Maryland, pages 27–31.

Kanamitsu, M., Ebisuzaki, W., Woollen, J., Yang, S.-K., Hnilo, J. J., Fiorino, M., and Potter, G. L. (2002). NCEP–DOE AMIP-II Reanalysis (R-2). Bulletin of the American Meteorological Society, 83(11):1631–1644.

Kang, Z., Ries, J., Bettadpur, S., Save, H., and Tapley, B. (2022). Combined Gravity Solution from SLR and GRACE/GRACE-FO. In International Association of Geodesy Symposia, pages 1–7. Springer, Berlin, Heidelberg.

Kaula, W. M. (1966). Theory of Satellite Geodesy. Applications of Satellites to Geodesy. Blaisdell.

Kehm, A., Bloßfeld, M., König, P., and Seitz, F. (2019). Future TRFs and GGOS – where to put the next SLR station? In Advances in Geosciences, volume 50, pages 17–25. Copernicus GmbH.

Kehm, A., Bloßfeld, M., Pavlis, E. C., and Seitz, F. (2018). Future global SLR network evolution and its impact on the terrestrial reference frame. Journal of Geodesy, 92(6):625–635.

Kim, J. (2000). Simulation Study of A Low-Low Satellite-to-Satellite Tracking Mission. Thesis, University of Texas, Austin.

Kokurin, Y. L. (2003). Lunar laser ranging: 40 years of research. Quantum Electronics, 33(1):45.

Kornfeld, R. P., Arnold, B. W., Gross, M. A., Dahya, N. T., Klipstein, W. M., Gath, P. F., and Bettadpur, S. (2019). GRACE-FO: The Gravity Recovery and Climate Experiment Follow-On Mission. Journal of Spacecraft and Rockets, 56(3):931–951.

Kvas, A., Brockmann, J. M., Krauss, S., Schubert, T., Gruber, T., Meyer, U., Mayer-Gürr, T., Schuh, W.-D., Jäggi, A., and Pail, R. (2021). GOCO06s – a satellite-only global gravity field model. Earth System Science Data, 13(1):99–118.

Landerer, F., Flechtner, F., Save, H., McCullough, C., Dahle, C., Bettadpur, S., Gaston, R., and Snopek, K. (2022). Extending Global Mass Change Satellite Observations Into the Third Decade With GRACE-FO: Science Mission Status and Plans. GRACE-FO Science Team Meeting 2022, Potsdam, Germany.

Landerer, F. W., Flechtner, F. M., Save, H., Webb, F. H., Bandikova, T., Bertiger, W. I., Bettadpur, S. V., Byun, S. H., Dahle, C., Dobslaw, H., Fahnestock, E., Harvey, N., Kang, Z., Kruizinga, G. L. H., Loomis, B. D., McCullough, C., Murböck, M., Nagel, P., Paik, M., Pie, N., Poole, S., Strekalov, D., Tamisiea, M. E., Wang, F., Watkins, M. M., Wen, H.-Y., Wiese, D. N., and Yuan, D.-N. (2020). Extending the Global Mass Change Data Record: GRACE Follow-On Instrument and Science Data Performance. Geophysical Research Letters, 47(12):e2020GL088306.

Lemoine, F. G., Klosko, S. M., Cox, C. M., and Johnson, T. J. (2006). Time-variable gravity from SLR and DORIS tracking. In Proceedings of the 15th International Workshop on Laser Ranging, Canberra. Citeseer.

Loomis, B. D. (2019). The critical role of satellite laser ranging (SLR) for correcting and validating GRACE & GRACE-FO gravity products and bridging the data gap. AGU Fall Meeting 2019, San Francisco, CA.

Loomis, B. D., Nerem, R. S., and Luthcke, S. B. (2012). Simulation study of a follow-on gravity mission to GRACE. Journal of Geodesy, 86(5):319–335.

Loomis, B. D., Rachlin, K. E., and Luthcke, S. B. (2019). Improved Earth Oblateness Rate Reveals Increased Ice Sheet Losses and Mass-Driven Sea Level Rise. Geophysical Research Letters, 46(12):6910–6917.

Loomis, B. D., Rachlin, K. E., Wiese, D. N., Landerer, F. W., and Luthcke, S. B. (2020). Replacing GRACE/GRACE-FO With Satellite Laser Ranging: Impacts on Antarctic Ice Sheet Mass Change. Geophysical Research Letters, 47(3):e2019GL085488.

Lyard, F. H., Allain, D. J., Cancet, M., Carrère, L., and Picot, N. (2021). FES2014 global ocean tide atlas: Design and performance. Ocean Science, 17(3):615–649.

Maier, A., Krauss, S., Hausleitner, W., and Baur, O. (2012). Contribution of satellite laser ranging to combined gravity field models. Advances in Space Research, 49(3):556–565.

McCarthy, J. J., Rowton, S., Moore, D., Pavlis, D. E., Luthcke, S. B., and Tsaoussi, L. S. (2015). GEODYN Systems Description Volume 1.

McGarry, J. F., Hoffman, E. D., Degnan, J. J., Cheek, J. W., Clarke, C. B., Diegel, I. F., Donovan, H. L., Horvath, J. E., Marzouk, M., Nelson, A. R., Patterson, D. S., Ricklefs, R. L., Shappirio, M. D., Wetzel, S. L., and Zagwodzki, T. W. (2019). NASA's satellite laser ranging systems for the twenty-first century. Journal of Geodesy, 93(11):2249–2262.

Menke, W. (2015). Review of the Generalized Least Squares Method. Surveys in Geophysics, 36(1):1–25.

Meyer, U., Sosnica, K., Arnold, D., Dahle, C., Thaller, D., Dach, R., and Jäggi, A. (2019). SLR, GRACE and Swarm Gravity Field Determination and Combination. Remote Sensing, 11(8):956.

National Academies of Sciences, Engineering, and Medicine (2018). Thriving on Our Changing Planet: A Decadal Strategy for Earth Observation from Space. National Academies Press, Washington, D.C.

Nerem, R. S., Chao, B. F., Au, A. Y., Chan, J. C., Klosko, S. M., Pavlis, N. K., and Williamson, R. G. (1993). Temporal variations of the Earth's gravitational field from satellite laser ranging to Lageos. Geophysical Research Letters, 20(7):595–598.

Nerem, R. S., Eanes, R. J., Thompson, P. F., and Chen, J. L. (2000). Observations of annual variations of the Earth's gravitational field using satellite laser ranging and geophysical models. Geophysical Research Letters, 27(12):1783–1786.

Nerem, R. S. and Klosko, S. M. (1996). Secular Variations of the Zonal Harmonics and Polar Motion as Geophysical Constraints. In Global Gravity Field and Its Temporal Variations, International Association of Geodesy Symposia, pages 152–163, Berlin, Heidelberg. Springer.

Otsubo, T., Aoyama, Y., Hattori, A., Doi, K., Pearlman, M. R., and Noll, C. E. (2019). The Final Frontier for Satellite Laser Ranging: Antarctica. The Tenth Symposium on Polar Science, Tokyo, Japan.

Otsubo, T., Matsuo, K., Aoyama, Y., Yamamoto, K., Hobiger, T., Kubo-oka, T., and Sekido, M. (2016). Effective expansion of satellite laser ranging network to improve global geodetic parameters. Earth, Planets and Space, 68(1):65.

Parkhomenko, N., Shargorodsky, V., Vasiliev, V., and Yurasov, V. (2013). Accident in orbit. 18th International Workshop on Laser Ranging, Fujiyoshida, Japan.

Pearlman, M. R., Degnan, J. J., and Bosworth, J. M. (2002). The International Laser Ranging Service. Advances in Space Research, 30(2):135–143.

Pearlman, M. R., Noll, C. E., Pavlis, E. C., Lemoine, F. G., Combrink, L., Degnan, J. J., Kirchner, G., and Schreiber, U. (2019). The ILRS: Approaching 20 years and planning for the future. Journal of Geodesy, 93(11):2161–2180.

Peltier, W. R., Argus, D. F., and Drummond, R. (2015). Space geodesy constrains ice age terminal deglaciation: The global ICE-6G_C (VM5a) model. Journal of Geophysical Research: Solid Earth, 120(1):450–487.

Pfaffenzeller, N., Pail, R., Gruber, T., Usbeck, T., and Gerardi, D. (2022). Impact of tone errors on gravity field solutions in NGGM concepts. GRACE-FO Science Team Meeting 2022, Potsdam, Germany.

Plotkin, H., Johnson, T., Spadin, P., and Moye, J. (1965). Reflection of ruby laser radiation from explorer XXII. Proceedings of the IEEE, 53(3):301–302.

Rodell, M., Famiglietti, J. S., Wiese, D. N., Reager, J. T., Beaudoing, H. K., Landerer, F. W., and Lo, M.-H. (2018). Emerging trends in global freshwater availability. Nature, 557(7707):651–659.

Savcenko, R. and Bosch, W. (2012). EOT11A - Empirical Ocean Tide Model from Multi-Mission Satellite Altimetry. https://epic.awi.de/id/eprint/36001/.

Schutz, B. E., Cheng, M. K., Eanes, R. J., Shum, C. K., and Tapley, B. D. (1993). Geodynamic Results from Starlette Orbit Analysis. In Contributions of Space Geodesy to Geodynamics: Earth Dynamics, pages 175–190. American Geophysical Union (AGU).

Sneeuw, N. (2000). A Semi-Analytical Approach to Gravity Field Analysis from Satellite Observations. PhD thesis, Technische Universität München.

Snyder, G., Hurst, S., Grafinger, A., and Halsey, H. (1965). Satellite laser ranging experiment. Proceedings of the IEEE, 53(3):298–299.

Sośnica, K. (2014). Determination of Precise Satellite Orbits and Geodetic Parameters Using Satellite Laser Ranging. Astronomical Institute, University of Bern, Switzerland.

Sośnica, K., Jäggi, A., Meyer, U., Thaller, D., Beutler, G., Arnold, D., and Dach, R. (2015). Time variable Earth's gravity field from SLR satellites. Journal of Geodesy, 89(10):945–960.

Su, X., Guo, J., Shum, C. K., Luo, Z., and Zhang, Y. (2020). Increased Low Degree Spherical Harmonic Influences on Polar Ice Sheet Mass Change Derived from GRACE Mission. Remote Sensing, 12(24):4178.

Sun, Y., Riva, R., and Ditmar, P. (2016). Optimizing estimates of annual variations and trends in geocenter motion and J2 from a combination of GRACE data and geophysical models. Journal of Geophysical Research: Solid Earth, 121(11):8352–8370.

Swenson, S., Chambers, D., and Wahr, J. (2008). Estimating geocenter variations from a combination of GRACE and ocean model output. Journal of Geophysical Research: Solid Earth, 113(B8).

Swenson, S. and Wahr, J. (2002). Methods for inferring regional surface-mass anomalies from Gravity Recovery and Climate Experiment (GRACE) measurements of time-variable gravity. Journal of Geophysical Research: Solid Earth, 107(B9):ETG 3–1–ETG 3–13.

Talpe, M. J., Nerem, R. S., Forootan, E., Schmidt, M., Lemoine, F. G., Enderlin, E. M., and Landerer, F. W. (2017). Ice mass change in Greenland and Antarctica between 1993 and 2013 from satellite gravity measurements. Journal of Geodesy, 91(11):1283–1298.

Tapley, B., Schutz, B., and Born, G. H. (2004a). Statistical Orbit Determination. Elsevier Science.

Tapley, B. D., Bettadpur, S., Watkins, M., and Reigber, C. (2004b). The gravity recovery and climate experiment: Mission overview and early results. Geophysical Research Letters, 31(9).

Tapley, B. D., Watkins, M. M., Flechtner, F., Reigber, C., Bettadpur, S., Rodell, M., Sasgen, I., Famiglietti, J. S., Landerer, F. W., Chambers, D. P., Reager, J. T., Gardner, A. S., Save, H., Ivins, E. R., Swenson, S. C., Boening, C., Dahle, C., Wiese, D. N., Dobslaw, H., Tamisiea, M. E., and Velicogna, I. (2019). Contributions of GRACE to understanding climate change. Nature Climate Change, 9(5):358–369.

Tavenner, M. S. (1962). Largos: A suggested method of stereo-triangulation (abstract). In Abstracts of the Papers Presented at the Forty-Third Annual Meeting, American Geophysical Union Washington, D.C., April 25–28, 1962, volume 67, pages 3537–3612. Journal of Geophysical Research (1896-1977).

Torge, W. (2001). Geodesy. Walter de Gruyter.

Torrence, M. H., Dunn, P. J., and Kolenkiewicz, R. (1995). Characteristics of the LAGEOS and ETALON satellites orbits. Advances in Space Research, 16(12):21–24.

Tucker, E. S., Nerem, R. S., and Loomis, B. D. (2022). Simulation of a Future SLR Satellite to Improve Low-Degree Gravity Estimates. Journal of Geophysical Research: Solid Earth, 127(12):e2022JB025743.

Tucker, E. S., Nerem, R. S., and Loomis, B. D. (2023). Impacts of SLR Ground Station Geographic Distribution on Time-Variable Gravity Recovery. Journal of Geophysical Research: Solid Earth, 128(9):e2023JB026638.

Vallado, D. A. (2013). Fundamentals of Astrodynamics and Applications, 4th Ed. Microcosm Press, 4th edition edition.

Velicogna, I. (2009). Increasing rates of ice mass loss from the Greenland and Antarctic ice sheets revealed by GRACE. Geophysical Research Letters, 36(19).

Wahr, J., Molenaar, M., and Bryan, F. (1998). Time variability of the Earth's gravity field: Hydrological and oceanic effects and their possible detection using GRACE. Journal of Geophysical Research: Solid Earth, 103(B12):30205–30229.

Wiese, D. N., Bienstock, B., Blackwood, C., Chrone, J., Loomis, B. D., Sauber, J., Rodell, M., Baize, R., Bearden, D., Case, K., Horner, S., Luthcke, S., Reager, J. T., Srinivasan, M., Tsaoussi, L., Webb, F., Whitehurst, A., and Zlotnicki, V. (2022). The Mass Change Designated Observable Study: Overview and Results. Earth and Space Science, 9(8):e2022EA002311.

Wiese, D. N., Nerem, R. S., and Han, S.-C. (2011). Expected improvements in determining continental hydrology, ice mass variations, ocean bottom pressure signals, and earthquakes using two pairs of dedicated satellites for temporal gravity recovery. Journal of Geophysical Research: Solid Earth, 116(B11).

Wiese, D. N., Nerem, R. S., and Lemoine, F. G. (2012). Design considerations for a dedicated gravity recovery satellite mission consisting of two pairs of satellites. Journal of Geodesy, 86(2):81–98.

Wu, X., Ray, J., and van Dam, T. (2012). Geocenter motion and its geodetic and geophysical implications. Journal of Geodynamics, 58:44–61.

Yoder, C. F., Williams, J. G., Dickey, J. O., Schutz, B. E., Eanes, R. J., and Tapley, B. D. (1983). Secular variation of Earth's gravitational harmonic J2 coefficient from Lageos and nontidal acceleration of Earth rotation. Nature, 303(5920):757–762.

Yu, H., Sośnica, K., and Shen, Y. (2021). Separation of geophysical signals in the LAGEOS geocentre motion based on singular spectrum analysis. Geophysical Journal International, 225(3):1755–1770.

Zelensky, N. P., Lemoine, F. G., Chinn, D. S., Melachroinos, S., Beckley, B. D., Beall, J. W., and Bordyugov, O. (2014). Estimated SLR station position and network frame sensitivity to time-varying gravity. Journal of Geodesy, 88(6):517–537.